AUV Localization in an Underwater Acoustic Positioning System

by

Dugald Thomson

B.Eng., Royal Military College of Canada, 2004

A Thesis Submitted in Partial Fulfillment
of the Requirements for the Degree of

MASTER OF SCIENCE

in the School of Earth and Ocean Sciences

University of Victoria

Supervisory Committee

AUV Localization in an Underwater Acoustic Positioning System

by

Dugald Thomson

B.Eng., Royal Military College of Canada, 2004

Supervisory Committee

Dr. Stan E. Dosso, (School of Earth and Ocean Sciences)
Supervisor

Dr. N. Ross Chapman, (School of Earth and Ocean Sciences)
Departmental Member

Dr. Michael J. Wilmut, (School of Earth and Ocean Sciences)
Departmental Member

Dr. Colin Bradley, (Department of Mechanical Engineering)
Outside Member

Abstract

Supervisory Committee
Dr. Stan E. Dosso, (School of Earth and Ocean Sciences, University of Victoria)
Supervisor
Dr. N. Ross Chapman, (School of Earth and Ocean Sciences, University of Victoria)
Departmental Member
Dr. Michael J. Wilmut, (School of Earth and Ocean Sciences, University of Victoria)
Departmental Member
Dr. Colin Bradley, (Department of Mechanical Engineering, University of Victoria)
Outside Member

This thesis develops a Bayesian inversion algorithm for autonomous underwater vehicle localization, and carries out a study of several factors contributing to localization accuracy in an underwater acoustic positioning system. Specifically, a ray-based algorithm is described that estimates target position through the linearized inversion of transmission arrival time differences, and provides linearized uncertainty estimates for model parameters. Factors contributing to source localization uncertainty considered here included: (1) modelling transmission paths accounting for refraction due to a depth-varying SSP instead of using a constant sound-speed approximation and straight-line propagation, (2) inverting for a potential bias in the measured sound-speed profile, (3) accounting for errors in hydrophone position by including these positions as unknown parameters in the inversion, and (4) applying path-dependent timing correction factors to account for lateral variability in the sound-speed profile. In each case, nonlinear Monte Carlo analysis is applied in which a large number of noisy data sets are considered, to obtain statistical measures of the localization improvement that results by addressing these factors.

Table of Contents

List of Tables

List of Figures

Acknowledgements

First and foremost, I must express a sincere thanks to my advisor and teacher, Dr. Stan E. Dosso, for his interminable patience, uncompromising dedication and genuine interest in my project. Thanks to Dr. Ross Chapman, our discussions on underwater acoustics were thought provoking and informative, and while Stan can claim to be your first Ocean Acoustics student, I am honoured to have been the last. To Dr. Michael J. Wilmut, I am grateful for our sweeping dialogues; your insight is unique. Thanks also to the UVic Ocean Acoustics Lab, including Jan, Jorge, Brendan and Gavin. The combined brainpower inside that room is both frightening and inspiring. To Dr. Colin Bradley and members of his lab, Emmett, Jeff and Allison: thanks for your support and for encouraging me to contribute to the OTTB project. Finally, thanks to the Dept. of National Defence for funding this research, and to those who allowed me this opportunity. I am grateful to you all.

Dedication

To the ocean, our closest neighbour of which we know so little.

"I seem to have been only like a boy playing on the seashore, and diverting myself in now and then finding a smoother pebble or a prettier shell than ordinary, whilst the great ocean of truth lay all undiscovered before me."

– Isaac Newton

1 Introduction

Precise positioning of autonomous underwater vehicles (AUVs) is an important problem for the ocean science community as it attempts to extend its reach further into the ocean's depths. Terrestrial Global Positioning Systems (GPS) are of little use for an underwater target as the high-frequency/low-power signals they employ are unable to penetrate beyond the surface layers of the ocean due to reflection and absorption by seawater. The Integrated Acoustic System (IAS) being designed by the University of Victoria's Ocean Technology Laboratory (OTL) aims to overcome this obstacle by developing a high-precision underwater acoustic positioning system, to be installed on the Ocean Technology Test Bed (OTTB). The goal is to produce a system, similar in operation to a commercial Long Baseline positioning unit, and connected to the Victoria Experimental Network Under the Sea (VENUS), a cutting-edge underwater cabled observatory. The IAS will be capable of localizing a target within the IAS range to a sufficient accuracy for use as ground truth for testing onboard navigation systems. This chapter provides background on AUVs, acoustic localization systems, cabled networks, the IAS range and sound speed in the ocean, as well as providing an overview of the work carried out in the remainder of the thesis.

1.1 Autonomous Underwater Vehicles

AUVs can function without tethers, cables, or remote control, and therefore they have a multitude of applications in oceanography, environmental monitoring, and underwater resource study (Akyildiz, Pompili, & Melodia, 2005). They are capable of operating independently or enhancing the data-gathering capabilities of underwater networks, and

there exists much enthusiasm for these vehicles as they have proven to be valuable instruments in the study and exploration of the oceans. AUV operation is rapidly gaining attention from the science community; however, with it come new challenges. Chief among these challenges is the issue of navigation.

Navigation represents the combination of localization and guidance, and is a fundamental problem that challenges progress in the field of underwater remote data gathering. One promising solution to the navigation issue that has long been employed by submarines and aircraft alike is the Inertial Navigation System (INS) (Stutters, Liu, Tiltman, & Brown, 2008). INS uses sensors to integrate acceleration measurements in three dimensions to provide an internally-referenced positioning solution; however, the position estimate is subject to a compounding, unbounded error known as "drift", and thus its accuracy degrades with time spent underwater. Additionally, these systems' operation is further challenged in the low-speed, low-acceleration regime typical of underwater oceanographic research vessels (L. Whitcomb, Yoerger, Singh, & Howland, 1999). To test the positional accuracy of these INS systems, or any other viable system, developers need a test range that can provide highly accurate ground-truth data to assess their systems' navigational performance. The OTL endeavours to provide just such a platform, through the IAS.

1.2 Underwater Acoustic Positioning Systems

The IAS functions in a manner similar to a typical Long Baseline (LBL) acoustic positioning system, offered commercially as a solution to a number of marine positioning applications, often as a higher-precision and longer-range alternative to ship-based Ultra

Short Baseline (USBL) systems. The baseline refers to the distance between receivers, which may be passive receivers, transceivers, or transponders. Applications for these types of positioning systems include offshore construction, drilling rig placement, marine survey work, precise situation of seismic and other sea-bottom sensors, and underwater navigation (Zhou, 2010). The use of spread-spectrum methods encourages improved accuracy and permits the simultaneous tracking of multiple targets (Gamroth, Kennedy, & Bradley, 2011)

Monteiro (2005) showed that modern differential GPS signals are capable of positioning a target to within 10 cm accuracy, for a target within receiving range of a differential ground station. Unfortunately for users of this magnificent technology, being within range also implies being on or above the Earth's surface, because giga-Hertz radio frequency (RF) signals broadcast by terrestrial GPS systems are incapable of penetrating to beyond a few metres depth in seawater, which is opaque to electromagnetic radiation, due to the high rate of absorption in this medium. Conversely, acoustic signals, which are mechanical waves, do not suffer this rapid degradation of signal strength in seawater. In comparison to RF signals, acoustic signals in the 5 kHz to 80 kHz frequency range (the range proposed for OTTB operation) are subject to attenuation on the order of 1 to 10 dB/km as they travel through this medium, while MHz frequency signals experience attenuations of upwards of 100dB/km. Acoustic signals with frequencies below 5 kHz are prone to lower levels of attenuation, but a higher frequency signal is also generally able to provide a more accurate position since arrival times can be measured more accurately, due to the improved signal resolution (International Marine Contractors Association,

2009). The operating frequency of an acoustic positioning system needs to be chosen carefully to achieve a balance between desired range and accuracy.

LBL systems are typically comprised of a minimum of three fixed, bottom-moored transponders, which reply to a received acoustic interrogation with an acoustic response. They are used to localize a target equipped with a transceiver that sends out the interrogation and receives the reply from the transponder stations (in some cases, the target carries the transponder and replies to interrogations from the fixed transceivers). These systems calculate position based on range only, and often use a time-of-flight technique known as trilateration to determine range relative to the calibrated array of transponders: essentially, the time of arrival (TOA) of each acoustic interrogation/reply defines a sphere whose centre is the fixed position of the transponder, and whose shell represents the set of possible locations of the target. Using the intersection of three or more such spheres (and a least-squares solution for an overdetermined system when more than three transponders are used), the target's potential locations are elucidated and an estimate of the target position is provided. Unidirectional data transmission (i.e., one-way time-of-flight measurements) from source to receiver can be achieved but requires time synchronization between target and receivers, a difficult achievement in the underwater environment (Wang, Kannan, & Wei, 2010). LBL systems can extend coverage over a larger area, either by adding transponders or by using lower frequency signals, however the latter adjustment comes at a cost of reduced localization accuracy. Systems using LBL generally assume straight-line acoustic rays in a constant sound-speed environment. SeaWeb, a system implemented by the US Navy, operates on this principle and was

shown to achieve an accuracy of 7-9 m when tracking AUVs inside of a 3 x 4 km range (Hahn, 2005).

Methods have been proposed to increase LBL system accuracies by accounting for the refraction of sound within a depth-dependent sound-speed profile. Ameer and Jacob (2010) describe a scheme where, using calculated ray trajectories for a measured sound-speed profile, a constant propagation delay surface from each anchor node is computed, and simulations show an improvement over localization using straight-line models, though the algorithm has yet to be implemented for real-world testing. High-grade commercial LBL systems such as Sonardyne's Prospector system claim to achieve a static accuracy of up to 30 cm within a 500-m^2 grid in a shallow-water environment (Chandrasekhar, Seah, Choo, & Ee, 2006), and Sonardyne's latest model, the Fusion 6G, is claimed to attain centimeter-order accuracies in any water depth with a calibration time of under 15 minutes (Sonardyne, 2012), however their techniques are not made readily available to the public.

An alternative to TOA is a ranging practice that calculates time difference of arrival (TDOA) known as multilateration (IMCA, 2009), which requires no knowledge of the absolute transmission instant. The time difference between arrivals at two receivers form a series of concentric circles centred on the receiver stations, with the intersection of rings forming a hyperbola representing the possible target positions. Comparing TDOA of each possible pair of transponder stations, a hyperbola is produced for each, and the intersection of hyperbolas represents the target's most-likely position. Information from a minimum of four receivers is required for a unique three-dimensional (3D) solution (since time differences for four receivers lead to three equations in three unknowns: *x, y*,

and z). TDOA does not require synchronization between target and receivers, and, similarly to TOA, typically assumes straight-line acoustic propagation through a constant sound-speed environment, but ray-tracing schemes can be applied in the same manner to account for refraction.

Commercially available alternatives to the LBL system include the Ultra Short Baseline (USBL) and Short Baseline (SBL) systems. While a typical LBL system operates with a transponder spacing on the order of 1 km, the transceivers in a SBL system are spread across only 10s of metres, and are often mounted along the length of the hull of a ship. The SBL system uses relative range along with vertical and horizontal angle measurements to a minimum of three transponders to determine the target position relative to the surface vessel. Both SBL and USBL systems are easily deployable since they require no bottom-mounted hardware, however SBL systems require additional inputs from ship sensors such as gyroscopes, and their positional accuracy is dependent on spacing between receivers, which is limited by the length of the ship's hull. The need for accurate calibration of transducers on the hull adds complexity, and reliability can be an issue with SBL systems.

USBL systems operate with an even shorter baseline than SBL, typically on the order of ~10 cm, and their transceivers are all contained within an array in a single hull-mounted enclosure. A USBL system measures interrogation-reply travel times to calculate the distance to a submerged target, equipped with a transponder, and the phase difference between arrivals at each receiver element is used to determine the bearing. Accuracy is inversely proportional to the slant range between target and receiver, so a USBL system is best suited for applications where a target remains in relatively close

proximity to the receiver array. The geometry of the LBL, SBL and USBL positioning systems are compared in Fig. 1.1 and Table 1.1

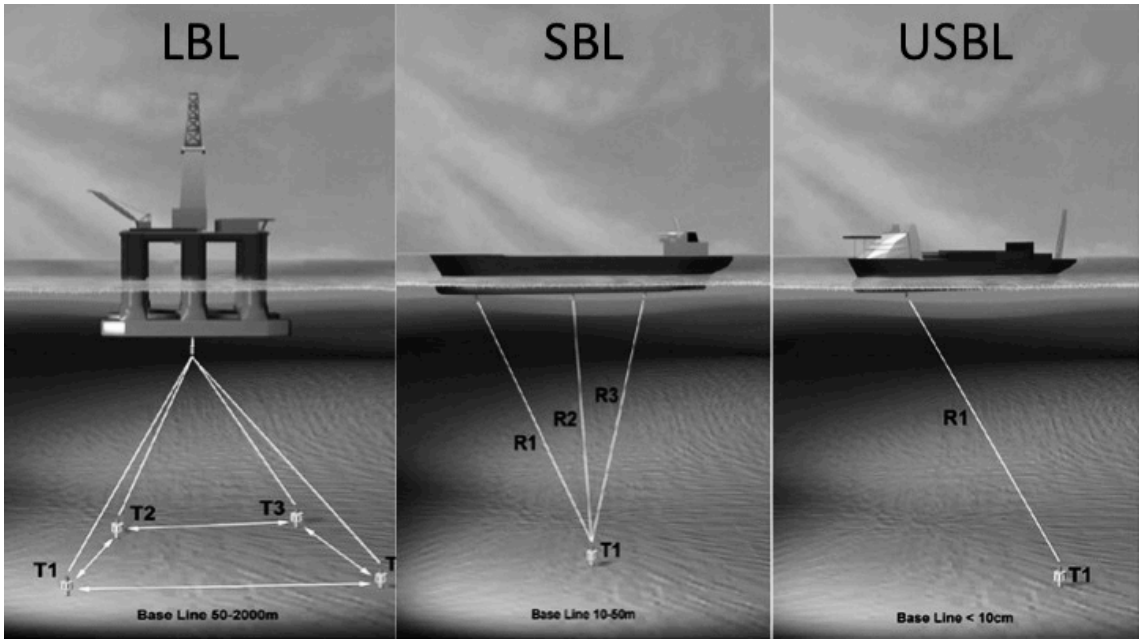

Figure 1.1: Comparison of geometry for Long Baseline, Short Baseline, and Ultra-short Baseline underwater acoustic positioning systems (Kongsberg, 2009).

In addition to the three systems described above, manufacturers have developed combined and hybrid acoustic positioning systems which improve accuracy and ease of deployment, and decrease system cost by combining the operation of two different baselines, or by aiding acoustic positioning through the use of depth sensors or heading sensors, inertial measurement units and Doppler velocity logs integrated to produce a single coherent position output (P. Lee, Jun, Kim, & Lee, 2007). These systems show promise but are beyond the scope of this project and will not be addressed for this research.

System	Baseline Length	Frequency	Nominal Accuracy
Ultra-short Baseline (USBL)	< 10 cm	HF (30 – 64 kHz)	0.02% slant range
Short Baseline (SBL)	10 – 50 m	LF (8 – 16 kHz)	0.05% slant range
Long Baseline (LBL)	50 – 6000+ m	MF (18 – 36 kHz)	0.25 m + 0.05% horizontal range

Table 1.1: Summary of baseline length and estimated accuracy for high-performance (able to account for sound-speed profile effects) Ultra-short Baseline (USBL), Short Baseline (SBL) and Long Baseline (LBL) systems. Operating frequencies chosen based on a minimum 2 km range requirement (International Marine Contractors Association, 2009).

Chandrasekhar and Choo (2006) present a complete survey of existing localization schemes for underwater networks. The authors break the various schemes into two broad categories: range-based and range-free, depending on whether the algorithm requires an input of time or range-based information. Among range-based algorithms, it is argued that the greatest challenge to achieving a high level of accuracy is the synchronization between transmitter and receiver clocks.

Bingham and Seering (2006) offered a solution to the AUV positioning problem that improved on the LBL method to provide a high-precision estimate using LBL infrastructure. They proposed the use of so-called hypothesis grids, which provide a Gaussian estimate of AUV position by incorporating prior knowledge of the environment in a probabilistic model to overcome the issue of poor-quality range measurements frequently arising in real-world LBL scenarios. The poor-quality measurements are due

to ambiguity about the path taken by the transmission – be it direct path, multipath, or an outlier arising from various sources of noise in the underwater environment. They found that by using hypothesis grids to determine the most likely transmission path, their predictive model was able to improve positional estimates and predict the source position for future measurements through a Bayesian inference-based navigation approach, making more information available for a positioning solution based on direct path or multipath observations.

Isik and Akan (2009) proposed a positioning algorithm for underwater networks that employs surface-based buoys to relay GPS information underwater without the use of an LBL system. They noted that there currently exist very few proposals for underwater localization schemes, and considered the effect of sound-speed measurement error on positional accuracy.

Whitcomb *et al.* (1999) advanced the basic concept of LBL positioning by combining a conventional LBL positioning system with Doppler navigation data. The authors point out two particular limitations of a stand-alone LBL positioning system, and how their combined system is able to overcome these deficiencies: precision arising from signal wavelength limitations in the frequency band of interest, and the restricted update rate for positional information. They found that their combined system showed significant improvement in navigation precision and update rate for real-world AUV navigation, without requiring the deployment of additional underwater navigation hardware.

Eustice *et al.* (2010) developed a synchronous-clock navigation system that uses an acoustic modem and a fleet of passively receiving underwater vehicles to measure one-

way travel time from an actively transmitting surface ship that acts as a reference beacon. Multiple vehicles are able to work concurrently within the system since only the beacon transmits a signal, and unlike a typical LBL system, no fixed-beacon network is required. The system was shown to provide a reliable, bounded-error horizontal-positioning solution that performed as well as a fixed-beacon LBL system with an error of 1 m.

1.3 Cabled Networks

Cabled observatories have gained prominence in recent years as a reliable method of gathering long-term localized oceanic data. The conventional approach to gathering this type of data in modern science has been to deploy an instrument, powered by batteries and requiring storage of the data on-site until the user is able to physically recover the sensor and collect the data. This approach is slow, labour-intensive, does not allow the user to inspect the data until the sensor is retrieved, prevents on-line system reconfiguration and failure detection, and the time series of data are limited by battery life and on-board storage capacity (Akyildiz *et al.*, 2005). The advent of the underwater cabled observatory, powered cables and network connections provides an approach to overcome these limitations to oceanic data collection.

The Victoria Experimental Network Under the Sea (VENUS) is at the cutting edge of the developing technological front in cabled observatories, allowing scientists and researchers to efficiently deploy underwater instruments, verify their continued serviceability, and monitor data in real time from an internet connection anywhere in the world. VENUS is not limited to short time-series, or concerned with the lifetime of

consumptive power draining sensors. VENUS is the shallow-water predecessor of the larger Northeast Pacific Time-integrated Undersea Networked Experiment (NEPTUNE) project, which came online off the coast of Vancouver Island in 2009. AUV operation is an important adjunct to the capabilities of VENUS, NEPTUNE, and cabled observatories in general, as it allows mobile remote data gathering, and the OTTB contributes to this concept by promoting testing and operational validation of these vehicles through the IAS.

1.4 Integrated Acoustic System

The OTTB range covers an area of approximately 1.5 km by 1.5 km, and the IAS is a cabled acoustic positioning system that operates to localize a target within these confines. The IAS is comprised of five 3-m high hydrophone towers mounted on the seabed at depths of 60 m to 130 m and located in the four corners of the range plus one in the centre, as depicted in Fig 1.2. AUVs operating in the range will be outfitted with a generic pinger, a transducer that periodically emits an acoustic pulse in the 5 kHz to 80 kHz range. As the pulse travels through the underwater medium, it is received at the five hydrophone stations, and the arrival times are used to localize the AUV. The OTTB is connected to VENUS and receives power and transmits data through its network.

The IAS will be used to support and test underwater vehicles, sensor platforms, and operational training scenarios, and will promote the development of new technologies and techniques, such as improved AUV navigation and capabilities, docking systems and control algorithms, multiple-vehicle cooperation techniques, and acoustic communication systems.

Figure 1.2: Conceptualized layout of the University of Victoria's Ocean Technology Test Bed infrastructure. Concentric circles indicate location of five cabled receiver towers (Ocean Technology Lab, 2005).

The IAS system is similar in operation to the LBL system described in Sec. 1.2; however, it makes use of the VENUS infrastructure to reduce the system complexity. Components of the IAS network are interconnected via a series of underwater cables that synchronize each hydrophone tower with a small system timing error. This allows for the use of simpler one-way time-of-flight calculations, since pings received at each hydrophone tower will be sent through the network for shore-based processing rather than returned to the target using bottom-mounted transponders. Because the target does not need to calculate its own position, as in the case of many bidirectional systems, it can operate with less-expensive and less-complex components such as generic, off-the-shelf

pingers. One particular advantage of this is the ability for increased inter-operability, where an outside agency can utilize the IAS range to test its AUVs without having to refit them with a transceiver or specific communication system to relay positional information back to shore.

The IAS employs the IEEE 1588 Precision Time Protocol (PTP), allowing a precision of $\pm$ 10 μs in clock timing (Lentz & Lecroart, 2009), a substantial improvement over the milliseconds-order accuracy offered by less precise network timing protocols typically employed in a data communication network. The shore station acts as the PTP master, and the cabled connections to each hydrophone station permits that master to discipline oscillators at each tower. This is significant, because clock error tends to be one of the dominant limiting factors to accuracy in an underwater positioning system. Additional development of the IEEE 1588 PTP protocol is expected to improve clock timing accuracy to within 100s of nanoseconds, which could further improve positional accuracy for a target operating in the range, an issue that is discussed in Chapter 4.

1.5 Sound-speed profile

One challenge in utilizing acoustics in the underwater environment lies in the dynamic nature of the marine environment. There is no "typical" environment, and the environment plays a determining factor in the propagation through the medium. The level of precision achievable in an underwater acoustic positioning system is largely a function of the user's ability to accurately define the environment (IMCA, 2006). Granted the high accuracy of time measurements due to the PTP network timing, the ability to

accurately measure the sound-speed field can be a limiting factor in the IAS positioning system.

The three main sources of uncertainty in modelling the sound-speed field within the range are: (1) the accuracy of the velocimeter used to measure the profile, in this case an Applied Microsystems SVPlus with specified accuracy of $\pm$ 0.05 m/s with a precision of $\pm$ 0.03 m/s (AML Oceanographic, 2012); (2) the calibration error or bias of the instrument, discussed further in Sec. 5.3; and (3) the temporal and spatial under-sampling of the sound-speed variability. This under-sampling represents an error that increases with time, since the water column properties change from the measured values as internal waves, tides, winds, daytime heating or cooling and other oceanographic phenomena cause variation in sound-speed structure from that which was measured. In addition, a sample taken at only one location represents the profile for that location alone, and is not necessarily representative for the entire path along which the rays travel. This two-dimensional variation in the sound-speed field and its effect on the positioning solution is further investigated in Sec. 5.5.

Kussat (2005) investigated the time discrepancy between sound-speed profiling casts separated by 2–3 hours at one site during an AUV positioning study, and found that the profiles varied by an average of $\pm$1.55 m/s in the upper 100 m from one cast to the next. This demonstrates the importance of adequately sampling the sound velocity profile, and lending these results to our application implies that accurate and current knowledge of the sound-speed field is an integral component in obtaining a precise positioning solution. Garcia (2005) argues that the physical properties of the water column must be known and accounted for in any underwater sensor network's positioning algorithm in order to

achieve reliable performance. His investigation provided a simulated analysis of the performance of four localization algorithms and analysed how each algorithm performed in terms of positioning error in response to changes in salinity, temperature, or depth.

Siderius, Nielsen, Sellschopp, Snellen, & Simons (2001) found that when using inverse methods to model shallow water acoustic propagation, severe problems can occur at ranges beyond a few kilometres when assuming time invariance for an environmental profile. Acoustic and oceanographic properties were measured over a three-day period while transmitting broadband acoustic signals through a weakly range-dependent medium, to correlate the time-varying environmental and acoustic data. Siderius *et al.* predicted that some regions were particularly time-dependent oceanographically, due to factors such as internal tides, surface waves and ambient noise. He found that at ranges of 5 and 10 km the estimated source position varied largely from the known position with errors increasing with range, with decorrelation times as low as one hour, but with good agreement for the 2-km data. The degradation of the inversion results at longer ranges indicates range and frequency limitations to inverse methods that depend on time-varying ocean properties.

Sound-speed profiles were derived from temperature and salinity data collected by Zaikova *et al*. (2010) within Saanich Inlet but outside the OTTB range, during the months of February, June, September, and December, 2008 (Fig. 1.3). These profiles demonstrate the seasonal variability of the water column.

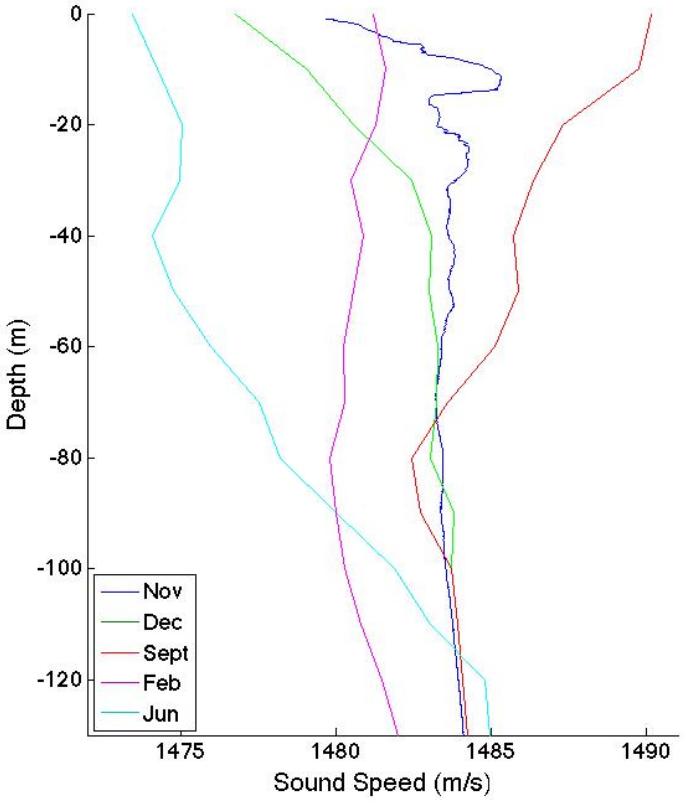

Figure 1.3: Sound-speed profiles in Saanich Inlet during the months of February, June, September, and December, 2008, calculated from temperature and salinity data of Zaikova *et al.* (2010), and November, 2011, from direct sound-speed measurement.

In addition, the sound-speed variability of the OTTB range was sampled during a field exercise, where direct sound-speed measurements were made with velocimeter casts at the range in Saanich Inlet, on November 8, 2011 (a day with calm winds) using an Applied Microsystems SVPlus velocimeter. The results are presented in Fig. 1.4. Nine distinct locations within the range were identified, and velocimeter casts were performed at each. Two hours later, six of these locations were sampled again, in order to investigate both the spatial and temporal sound-speed variability of the water column.

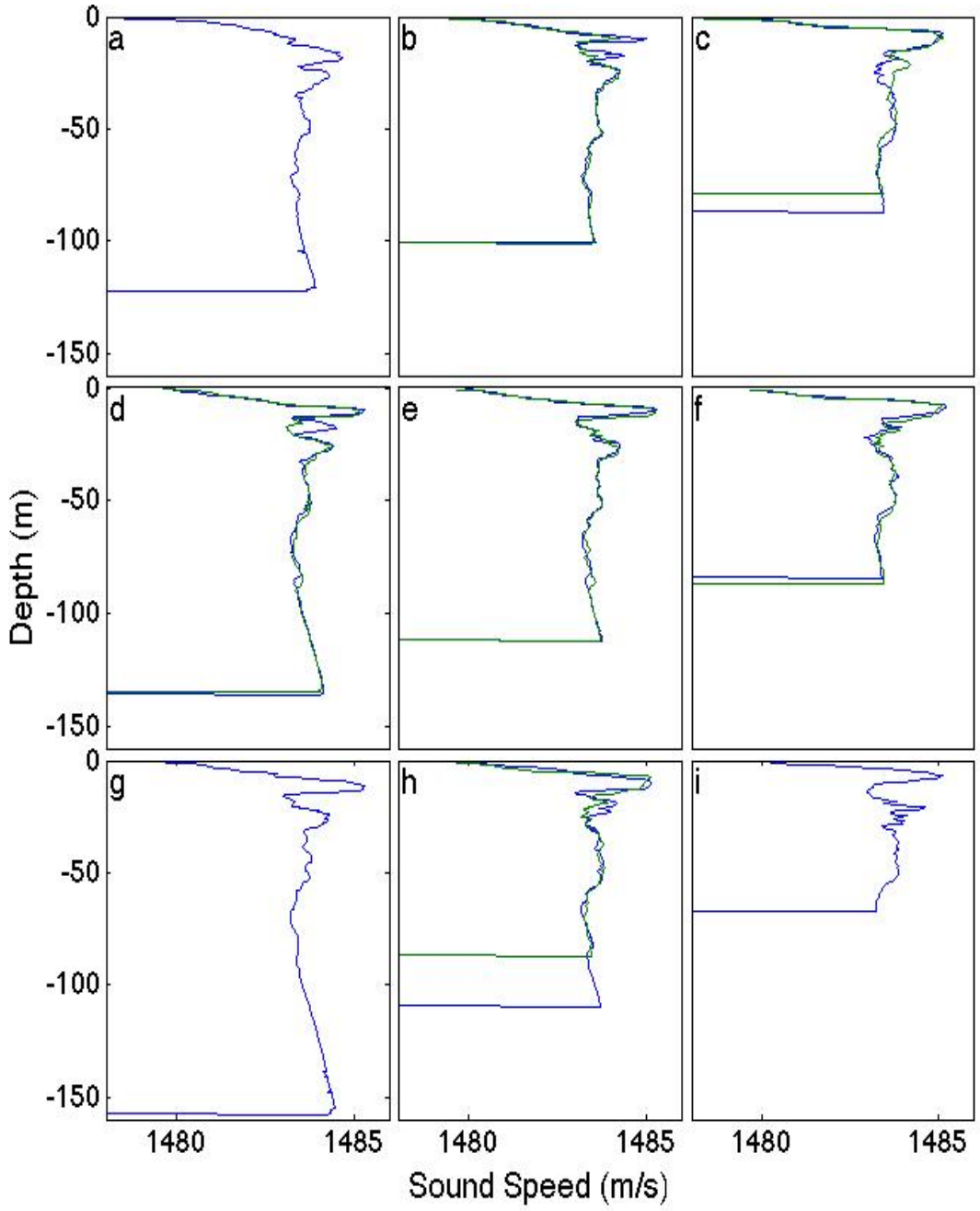

Figure 1.4: Sound-speed profiles collected November 2011 at nine locations within the OTTB range (Figs. 1.3a to 1.3i) with the first sample taken shown in blue and the resampling of 6 sites 2 hours later shown in green. Profile locations within the figure represent approximate placement within the range, (a) showing the sample taken in the NW corner of the range and (i) showing the sample taken in the SE corner.

The acoustic environment determines the transmission paths of sound from source to receiver. A ray model can predict various acoustic paths from source to receiver, including the direct path, surface- and bottom-reflected paths, and paths that are made up of a combination of surface and bottom reflections. A ray with a greater number of reflections will tend to have a longer ray path and time of flight. Due to the relatively short ranges for rays in the IAS and the increased complexity of a system that is required to measure and identify paths, only the direct path rays will be used in the IAS. This assumption may have implications on the accuracy of the system, since shadow zones are predicted by the ray tracing in some locations, as discussed in Sec. 5.1.

1.6 Outline of Work

The goal of this thesis is to develop a ray-based AUV localization algorithm which addresses errors due to dynamic variation in ocean sound speed, as well as uncertainty in receiver locations, based on an inversion of the arrival time data. The algorithm is expected to improve the localization capability of the IAS, so that the OTTB is able to provide a high-accuracy ground truth positioning solution for the test and evaluation of underwater vehicle navigation systems. The work will concentrate on identifying quantifying, and addressing sources of uncertainty in the system, and modelling their anticipated effect on overall target-position uncertainty.

The remainder of this thesis is comprised of the following components:

Chapter 2 develops the essential inverse theory required to formulate the algorithm. Linearization of non-linear problems is discussed and the method of regularization, where prior information is included in the inversion, is introduced.

Chapter 3 presents the ray theory on which the transmission model is based. Ray tracing is the foundation upon which improved system accuracy is based, and the chapter begins by deriving essential ray equations from Snell's law, and works up to the ray partial derivatives and water-column discretization method used in the localization algorithm.

Chapter 4 presents an initial modelling study carried out to assess localization accuracy throughout the OTTB range, including localization uncertainties due to timing errors, receiver-location uncertainties, and sound-speed bias. This work is novel and was published in the journal Canadian Acoustics (Thomson, Dosso, Gamroth & Bradley, 2012*)* and is reproduced in the chapter.

Chapter 5 describes more in-depth modelling studies that were developed to address several important factors in source localization accuracy. To this end, a series of simulations are carried out. The simulation scenarios were developed to investigate: (1) modelling transmission paths accounting for refraction due to a depth-varying SSP instead of using straight rays through a constant sound-speed approximation, (2) inverting for a potential sound-speed bias in the measured profile, (3) accounting for errors in hydrophone position by including these positions as unknowns in the inversion, and (4) applying path-dependent time correction factors to account for lateral variability in the sound-speed profile. The first three factors have been considered previously in the context of array element localization; however, this work represents the first application to AUV localization. The fourth factor (path corrections) is novel here.

Chapter 6 summarizes and discusses the approaches and results of this thesis.

2 Inverse Theory

Inverse theory has been used to determine solutions to a wide range of geophysical and acoustic problems. This thesis uses inverse methods to localize an AUV by inverting hydrophone time difference of arrival (TDOA) data to solve for 3D target position. This is formulated as an iterative, linearized Bayesian inversion, regularized using available prior information about the target position and environment, and provides analytic uncertainty estimates in the AUV location (within a linearized approximation which is later verified through Monte Carlo methods), accounting for the assumed uncertainties in arrival-time data, receiver locations, and sound-speed profile. The fundamental theory, as it pertains to this application, is discussed in this chapter by introducing the concept of inverse theory and the Bayesian probability framework, and developing iterative linearization and regularization methods. Overviews of inverse theory can be found in Menke (1984), Parker (1994), and Aster, Borchers & Thurber (2004); and of the Bayesian approach in Tarantola (1987) and Sen & Stoffa (1995).

2.1 Introduction to Inverse Theory

In general, an inverse problem can be regarded as an approach to estimate the parameters of an assumed model of a physical system by observing the response of some signal that interacts with the system. The model and the data are related through forward and inverse problems. The forward mapping function F applied to a model vector $\mathbf{m}$ predicts the data $\mathbf{d}$ where

$$\mathbf{d} = F[\mathbf{m}] = \mathbf{d}(\mathbf{m}). \tag{2.1}$$

The model that is mapped into the data is often a simplification of the true physical system of interest, and if the parameterization is not adequate, some level of systematic error is expected. The forward problem represents a real physical process that exists in nature, and as such its solution exists, and is unique and stable.

In contrast, the inverse problem

$$\mathbf{m} = F^{-1}[\mathbf{d}] \tag{2.2}$$

represents estimating the model parameters from information in the observed data. Inverse problems are mathematical (not physical) problems and the solution is generally non-unique and sometimes does not exist at all. Furthermore, the solution can be unstable: a small perturbation in data can cause a large change in the model. A solution to an inverse problem is found to exist if a model can be found that replicates the observed data to within uncertainties; however, the converse (non-existence of a solution) is not proved if an acceptable model can not be found.

2.2 Bayesian Formulation

In Bayesian inversion, model parameters are regarded not as deterministic variables but rather as random variables that we seek to describe statistically. The state of any variable is expressed in terms of the degree of belief about its value, called the Bayesian probability. The basis for this approach is Bayes' Theorem,

$$\mathrm{P}(\mathbf{m}|\mathbf{d}) = \frac{\mathrm{P}(\mathbf{d}|\mathbf{m})\mathrm{P}(\mathbf{m})}{\mathrm{P}(\mathbf{d})}, \tag{2.3}$$

where **m** and **d** are random variables representing the model parameters and data, respectively. $\mathrm{P}(\mathbf{m}|\mathbf{d})$ is the posterior probability density (PPD), representing the total information about the model including both data and prior information. $\mathrm{P}(\mathbf{d})$ is the prior

data distribution, which represents a constant factor once the data have been observed and hence can be neglected here and treated as a normalization term. $\mathrm{P}(\mathbf{m})$ is the prior model distribution representing what is known about $\mathbf{m}$ independent of the data. For example, a Gaussian prior distribution about a prior estimate $\widehat{\mathbf{m}}$ is expressed as

$$\mathrm{P}(\mathbf{m}) = \frac{1}{(2\pi)^{M/2}\left|\mathbf{C_p}\right|^{1/2}} \exp\left[-(\mathbf{m}-\widehat{\mathbf{m}})^T \mathbf{C_p}^{-1}(\mathbf{m}-\widehat{\mathbf{m}})/2\right] \tag{2.4}$$

where M is the number of model parameters and $\mathbf{C_p}$ is the prior model covariance matrix. In Eq. (2.3) $\mathrm{P}(\mathbf{d}|\mathbf{m})$ is the conditional probability of observing the data $\mathbf{d}$ given model $\mathbf{m}$; however, after the data have been observed, $\mathrm{P}(\mathbf{d}|\mathbf{m})$ is treated as a function of $\mathbf{m}$, known as the likelihood function $\mathcal{L}(\mathbf{m})$ (the likelihood of the model is equivalent to the probability of observing the data that were observed given the model $\mathbf{m}$). For Gaussian-distributed errors with data covariance matrix $\mathbf{C_d}$ this function can be expressed as

$$\mathcal{L}(\mathbf{m}) = \frac{1}{(2\pi)^{N/2}\left|\mathbf{C_d}\right|^{1/2}} \exp\left[-\big(\mathbf{d}-\mathbf{d}(\mathbf{m})\big)^T \mathbf{C_d}^{-1}\big(\mathbf{d}-\mathbf{d}(\mathbf{m})\big)/2\right], \tag{2.5}$$

where $\mathbf{d}(\mathbf{m})$ represents data predicted for the model $\mathbf{m}$. Neglecting the normalization factor $\mathrm{P}(\mathbf{d})$, Eq. (2.3) can be rewritten as

$$\mathrm{P}(\mathbf{m}|\mathbf{d}) \propto \mathrm{P}(\mathbf{m})\mathcal{L}(\mathbf{m}), \tag{2.6}$$

and by combining Eqs. (2.4), (2.5), and (2.6) the PPD can be expressed as

$$\mathrm{P}(\mathbf{m}\,|\,\mathbf{d}) \propto \exp\left[-\phi(\mathbf{m},\mathbf{d})/2\right], \tag{2.7}$$

where

$$\phi(\mathbf{m},\mathbf{d}) = (\mathbf{d}-\mathbf{d}(\mathbf{m}))^T \mathbf{C_d}^{-1}(\mathbf{d}-\mathbf{d}(\mathbf{m})) + (\mathbf{m}-\widehat{\mathbf{m}})^T \mathbf{C_p}^{-1}(\mathbf{m}-\widehat{\mathbf{m}}). \tag{2.8}$$

While the PPD represents a full solution to the Bayesian inverse problem, due to its multi-dimensional nature, a number of properties defining parameter estimates,

uncertainties, and interrelationships, must be considered in interpreting the result. These properties include the maximum *a posteriori* (MAP) estimate $\mathbf{m_{MAP}}$, the posterior mean estimate $\bar{\mathbf{m}}$, the posterior model covariance matrix $\mathbf{C_m}$, and marginal probability distributions $\mathrm{P}(m_i|\mathbf{d})$ defined, respectively, as

$$\hat{\mathbf{m}} = \mathrm{Arg}\max_{\mathrm{m}} \mathrm{P}(\mathbf{m}|\mathbf{d}) = \mathrm{Arg}\min_{\mathrm{m}} \phi(\mathbf{m}, \mathbf{d}), \tag{2.9}$$

$$\bar{\mathbf{m}} = \int \mathbf{m}' \mathrm{P}(\mathbf{m}'|\mathbf{d}) d\mathbf{m}', \tag{2.10}$$

$$\mathbf{C_m} = \int (\mathbf{m}' - \bar{\mathbf{m}})(\mathbf{m}' - \bar{\mathbf{m}})^T \mathrm{P}(\mathbf{m}'|\mathbf{d}) d\mathbf{m}' \tag{2.11}$$

$$\mathrm{P}(m_i|\mathbf{d}) = \int \delta(m_i' - m_i) \mathrm{P}(\mathbf{m}'|\mathbf{d}) d\mathbf{m}', \tag{2.12}$$

where δ is the Dirac delta function. Analytic solutions to Eqs. (2.9) to (2.12) exist for linear inverse problems (given in Sec. 2.2), and can be applied to weakly non-linear problems (Sec. 2.3).

2.3 Linear Inverse Theory

A discrete linear problem with *N* data and *M* model parameters can be expressed as a set of *N*x*M* linear equations

$$\mathbf{d} = \mathbf{d}(\mathbf{m}) = \mathbf{A}\mathbf{m}, \tag{2.13}$$

where **A** is an *N*x*M* sensitivity or Jacobian matrix containing the physics and geometry of the forward problem, and whose element $A_{ij} = \partial d_i / \partial m_j$ quantifies the sensitivity of the data point d_i to the model parameter m_j.

For linear problems, Eqs. (2.9) – (2.12) have analytic solutions. To find the MAP estimate $\hat{\mathbf{m}}$, $\phi(\mathbf{m}, \mathbf{d})$ must be minimized over $\mathbf{m}$ by setting $\partial \boldsymbol{\phi}(\mathbf{m}, \mathbf{d}) / \partial \mathbf{m} = 0$ and solving to obtain (Menke, 1984, and Foster, 1994)

$$\mathbf{m_{MAP}} = \widehat{\mathbf{m}} + \left[\mathbf{A}^{\mathrm{T}}\mathbf{C_d}^{-1}\mathbf{A} + \mathbf{C_p}^{-1}\right]^{-1}\mathbf{A}^{\mathrm{T}}\mathbf{C_d}^{-1}\mathbf{d}. \tag{2.14}$$

The model covariance matrix $\mathbf{C_m}$ can be expressed analytically as

$$\mathbf{C_m} = \left[\mathbf{A}^{\mathrm{T}}\mathbf{C_d}^{-1}\mathbf{A} + \mathbf{C_p}^{-1}\right]^{-1}. \tag{2.15}$$

The PPD is given by

$$\mathrm{P}(\mathbf{m}|\mathbf{d}) = \frac{1}{(2\pi)^{M/2}|\mathbf{C_m}|^{1/2}} \exp\left[-(\mathbf{m}-\mathbf{m_{MAP}})^{T}\mathbf{C_p}^{-1}(\mathbf{m}-\mathbf{m_{MAP}})/2\right] \tag{2.16}$$

with the marginal distributions

$$\mathrm{P}(\mathrm{m}_i|\mathbf{d}) = \frac{1}{2\pi\left(C_{\mathrm{m}_{ii}}\right)^{1/2}} \exp\left[-\left(\mathrm{m}_i - \mathrm{m}_{\mathrm{MAP}_i}\right)^2/2\mathrm{C}_{\mathrm{m}_{ii}}\right]. \tag{2.17}$$

2.4 Linearized Inversion

A comprehensive theory exists for linear inverse problems with Gaussian data errors and Gaussian priors; however, our ability to solve non-linear problems is limited. If a problem is not strongly non-linear (quasi-linear), it can be locally approximated as a linear problem and iterated to solution using linearized inversion.

2.4.1 Linearization

To derive a linearized solution, the data, which represent non-linear functionals of the model parameters, are expanded in a generalized Taylor Series to first order about an arbitrary starting model $\mathbf{m_0}$,

$$\mathbf{d} = \mathbf{d}(\mathbf{m}) \approx \mathbf{d}(\mathbf{m_0}) + \mathbf{J}(\mathbf{m}-\mathbf{m_0}), \tag{2.18}$$

where $J_{ij} = \partial \mathrm{d_i}(\mathbf{m_0})/\partial \mathrm{m_j}$ is the ij element of the Jacobian matrix $\mathbf{J}$ of partial derivatives, evaluated at $\mathbf{m_0}$.

Defining $\delta\mathbf{d} = \mathbf{d} - \mathbf{d}(\mathbf{m_0})$ and $\delta\mathbf{m} = \mathbf{m} - \mathbf{m_0}$, Eq. (2.13) can be rewritten as

$$\delta\mathbf{d} = \mathbf{J}\delta\mathbf{m} \tag{2.19}$$

which defines a linear inverse problem for $\delta\mathbf{m}$ that can be solved using the methods described in Sec. 2.4 and the model solution is then $\mathbf{m} = \mathbf{m_0} + \delta\mathbf{m_0}$. Since higher-order terms are neglected in Eq. (2.19), the predicted data produced by the linear solution are compared to the observed data and if they do not produce a statistically acceptable fit then further iterations are required by updating the starting model $\mathbf{m_0} \leftarrow \mathbf{m}$ and repeating the inversion iteratively until convergence.

Equation (2.19) represents a linear relationship between data and model perturbations, where the solution is obtained by a series of small perturbations, and the final model typically depends on the starting model, known as the "creeping" approach. For a problem that is weakly non-linear, linearization is generally applicable; however, for a problem that is more strongly non-linear, the method may fail due to non-linear effects such as local minima near the starting model. In this case, non-linear approaches are required; the reader is directed to Sambridge & Mosengaard (2002) for further reading on non-linear inversion methods.

2.4.2 Regularization

A strategy to stabilize an inverse problem by applying prior information to the model is known as regularization. In general, prior information can be applied to model parameters or their derivatives, or can reflect the type of solution (structure) that is expected.

Defining modified data as $\mathbf{d}' = \mathbf{d} - \mathbf{d}(\mathbf{m_0}) + \mathbf{J}\mathbf{m_0}$, Eq. (2.13) can be rewritten as a linear inverse problem for the model parameters $\mathbf{m}$ (rather than perturbation $\delta\mathbf{m}$) as

$$\mathbf{d}' = \mathbf{J}\mathbf{m}, \tag{2.20}$$

and Eqs. (2.14) - (2.15) can include this modified data term as

$$\mathbf{m_{MAP}} = \hat{\mathbf{m}} + \left[\mathbf{J}^{\mathrm{T}}\mathbf{C_d}^{-1}\mathbf{J} + \mathbf{C_p}^{-1}\right]^{-1}\mathbf{J}^{\mathrm{T}}\mathbf{C_d}^{-1}\mathbf{d}'. \tag{2.21}$$

and

$$\mathbf{C_m} = \left[\mathbf{J}^{\mathrm{T}}\mathbf{C_d}^{-1}\mathbf{J} + \mathbf{C_p}^{-1}\right]^{-1}. \tag{2.22}$$

As with the "creeping" approach, since higher order terms are neglected in Eq. (2.20), iteration is required to converge to a final solution. This approach tends to take larger steps at each iteration, and is referred to as "jumping".

2.5 AUV Localization

The general problem in this thesis is to invert for the 3D AUV position (x_i, y_i, z_i), hydrophone positions (X_j, Y_j, Z_j) for i = 1,.., S, and j = 1,.., H, where S is the number of source transmissions and H is the number of hydrophones, and a bias c_b to the sound-speed profile which constitute the model parameters:

$$\mathbf{m} = \begin{bmatrix} x_i, y_i, z_i, X_j, Y_j, Z_j, c_b, & \text{for } i = 1,..,S, \\ & j = 1,..,H \end{bmatrix}^{\mathrm{T}}. \tag{2.23}$$

The data represent a set of arrival time differences *(t_{j1}, j* = 2,.., *H*), defined as the difference of transmission arrival time at hydrophone *j* and hydrophone 1, determined using a cross-correlation function to calculate the time difference between arrival instants directly, with assumed independent Gaussian-distributed errors of standard deviation $\sigma = \sqrt{2} * 10\ \mu s$ giving

$$\mathbf{C_d} = \begin{bmatrix} \sigma^2 & \dots & 0 \\ \vdots & \ddots & \vdots \\ 0 & \dots & \sigma^2 \end{bmatrix}. \tag{2.24}$$

Prior information consists of prior parameter estimates $\widehat{\mathbf{m}}$ with Gaussian-distributed uncertainties of standard deviation ξ_i for $\widehat{m}_i$, which give a prior covariance matrix of

$$\mathbf{C_p} = \begin{bmatrix} {\xi_1}^2 & \dots & 0 \\ \vdots & \ddots & \vdots \\ 0 & \dots & {\xi_n}^2 \end{bmatrix}. \tag{2.25}$$

The linearized solution is given by Eq. (2.21), with posterior covariance matrix given by Eq. (2.22).

3 Ray Theory

3.1 Propagation Modelling

When considering sound transmission problems in the ocean, we seek a mathematical solution to the wave equation usually based on one of five common propagation models. For low frequencies (< 1 kHz) and assuming range independence, normal-mode or fast-field (wave-number integral) methods provide an exact solution. When considering low frequencies in a range-dependent environment, parabolic equations are appropriate, and direct solution of the wave equation through finite-difference or finite-element models provide accurate results at the expense of highly-demanding computational requirements. However, for high-frequency applications where the full wave-field solution is not required, the ray method is most suitable (Jensen, Kuperman, Porter, & Schmidt, 2011) since it provides travel times with minimal computational effort. Ray theory is based on an approximation that holds for wave propagation at sufficiently high frequencies, where wavelength (λ) is small compared to range and water depth, as well as sound speed gradients that satisfy

$$\frac{\lambda}{c}\left|\frac{dc}{dz}\right| \ll 1. \tag{3.1}$$

Ray theory in a horizontally stratified ocean approximates the medium by many discrete layers within which the sound speed varies as a given function of depth. In the ocean, sound speed is a function of temperature, salinity, and pressure, so sound speed in each layer is defined by these variables.

3.2 Eikonal Equation

Fermat's principle states that the path taken by a ray is the one that takes the least time. This principle could be applied to the problem of predicting the ray path; however, the geometric approach is also valid and will be used here. The Eikonal equation, which results from an approximate solution to the general Helmholtz wave equation, forms the basis for solving the ray equations, used to trace the trajectory of a ray path. The Eikonal equation takes the form

$$(\nabla W)^2 = n(\boldsymbol{r})^2 \tag{3.2}$$

where W is a function representing the wave front, ∇ is the gradient operator, and $n(\boldsymbol{r})$ is the index of refraction, a dimensionless function of the position vector $\boldsymbol{r}$ defined as

$$n(\boldsymbol{r}) = \frac{c_0}{c(\boldsymbol{r})}, \tag{3.3}$$

where c_0 is some reference propagation speed and $c(\boldsymbol{r})$ is the propagation speed vector, a function of $\boldsymbol{r}$. Equation (3.2) shows that $n(\boldsymbol{r})$ is parallel to ∇W, as the gradient of W is directed towards the maximum rate of change of W. The eikonal equation defines the geometry of rays as they move through the medium, and the ray equations can be expressed as

$$\frac{d}{ds}\left[n(\boldsymbol{r})\frac{dx}{ds}\right] = \frac{\partial}{\partial x}n(\boldsymbol{r}), \tag{3.4}$$

$$\frac{d}{ds}\left[n(\boldsymbol{r})\frac{dy}{ds}\right] = \frac{\partial}{\partial y}n(\boldsymbol{r}), \tag{3.5}$$

$$\frac{d}{ds}\left[n(\boldsymbol{r})\frac{dz}{ds}\right] = \frac{\partial}{\partial z}n(\boldsymbol{r}); \tag{3.6}$$

however, for simplicity it is assumed that the medium is range independent and $n(\boldsymbol{r})$ and $c(\boldsymbol{r})$ are functions of z only, becoming $n(z)$ and $c(z)$. Applying this assumption,

$$\frac{d}{ds}\left[n(z)\frac{dx}{ds}\right] = 0 \tag{3.7}$$

$$\frac{d}{ds}\left[n(z)\frac{dy}{ds}\right] = 0 \tag{3.8}$$

$$\frac{d}{ds}\left[n(z)\frac{dz}{ds}\right] = \frac{dn(z)}{dz}, \tag{3.9}$$

implying that

$$n(z)\frac{dx}{ds} = \text{constant}, \tag{3.10}$$

$$n(z)\frac{dy}{ds} = \text{constant}. \tag{3.11}$$

Combining Eqs. (3.10) and (3.11) it can be seen that $\left({}^{dx}/_{ds}\right)\left({}^{dy}/_{ds}\right)^{-1} = \text{constant}$, which indicates that the ray travel is confined to a plane normal to the *xy*-plane. For simplicity, consider now the plane in which the ray travels, consisting of the vertical direction *z* and the horizontal direction *r*, as shown in Fig. 3.1.

Considering a ray confined to a two-dimensional plane parallel to *r*, Eq. (3.9) can be expressed as

$$\frac{d}{ds}\theta(z) = -\frac{\cos\theta(z)}{c(z)}\frac{d}{dz}c(z). \tag{3.12}$$

Defining the gradient of $c(z)$ as ${}^{dc(z)}/_{dz,}$ Eq. (3.12) implies that for ${}^{dc(z)}/_{dz} < 0$, ${}^{d\theta(z)}/_{ds} > 0$, meaning raypaths will curve down; similarily, for ${}^{dc(z)}/_{dz} > 0$, ${}^{d\theta(z)}/_{ds} < 0$, raypaths curve up. Interpreted differently, the curvature of the ray is proportional to the negative of the gradient, causing rays to bend towards the region of minimum sound speed.

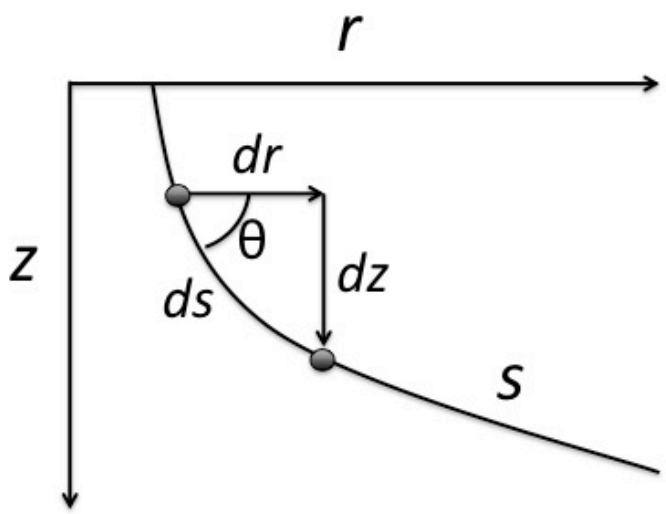

Figure 3.1: Ray path in a continually stratified medium showing the differential distance along the path *ds* in terms of lateral and vertical displacements *dr* and *dz* respectively.

Approximating the infinitesimal ray path length *ds* in Fig. 3.1 as the hypotenuse of a right triangle with sides *dr* and *dz*, it follows that

$$\frac{dr}{ds} = \cos\theta(z) \tag{3.13}$$

$$\frac{dz}{ds} = \sin\theta(z). \tag{3.14}$$

Combining Eqs. (3.9) and (3.13), we obtain

$$n(z)\frac{dr}{ds} = n(z)\cos\theta(z) = \text{constant}, \tag{3.15}$$

representing Snell's Law.

3.3 Snell's Law

Ray tracing in its most basic form is the prediction of how acoustic rays will bend along their path due to refraction. According to Snell's law, for a ray at a grazing angle $\theta(z)$ at some depth z with a sound speed $c(z)$

$$\frac{\cos\theta(z)}{c(z)} = p, \tag{3.16}$$

where p is the ray parameter, which is constant along a ray path. This implies that for layers n and $n+1$

$$\frac{\cos\theta_n(z)}{c_n(z)} = \frac{\cos\theta_{n+1}(z)}{c_{n+1}(z)} = p. \tag{3.17}$$

Again referring to the approximate right angle in Fig. 3.1, expressions for dt and dr are found to be $dt = ds/c\,(z)$, and $dz = \tan\theta(z)\,dr$. It follows then that

$$t = \int_0^s \frac{ds}{c(z)} = \int_0^z \frac{dz}{\mathrm{c(z)}\sin\theta(z)} \tag{3.18}$$

$$r = \int_0^z \frac{dz}{\tan\theta(z)}. \tag{3.19}$$

Snell's law can be employed to eliminate the trigonometric functions from the above equations, giving

$$\cos\theta(z) = pc(z), \tag{3.20}$$

$$\sin\theta(z) = \left[1 - p^2c^2(z)\right]^{1/2}, \tag{3.21}$$

$$\tan\theta(z) = \frac{\left[1 - p^2c^2(z)\right]^{1/2}}{pc(z)}. \tag{3.22}$$

The horizontal distance between a source located at (x_i, y_i, z_i) and a hydrophone at (X_j, Y_j, Z_j) is calculated geometrically as

$$r = \left[\left(X_j - x_i\right)^2 + \left(Y_j - y_i\right)^2\right]^{1/2}. \tag{3.23}$$

Using Eqs.(3.18)– (3.22), a direct acoustic wave transmitted from the source at time t_0 is received at the hydrophone at time t where

$$t = t_0 + \int_{z_i}^{z_j} \frac{dz}{pc(z)[1 - p^2c^2(z)]^{1/2}}, \tag{3.24}$$

while the horizontal displacement *r* can be written as

$$r = \int_{z_i}^{z_j} \frac{pc(z)dz}{[1 - p^2c^2(z)]^{1/2}}. \tag{3.25}$$

These expressions are written assuming $Z_j > z_i$, i.e., the hydrophone is located at a greater depth than the source. For the opposite case ($Z_j < z_i$), a negative sign is required for the integrals in this and following sections unless otherwise noted.

Standard ray tracing algorithms search for a ray parameter value that produces an eigenray connecting source and receiver to within a pre-defined tolerance. The ray parameter defines the take-off angle at the source and is estimated here using an efficient approach based on Newton's method as summarized in Dosso & Ebbeson (2006), from concepts developed in previous work (Dosso *et al.,*1998a,b). Initially a straight ray is assumed to connect source and receiver through a medium with a constant sound speed c_H, the harmonic mean of the sound speed between source and receiver,

$$c_H = \frac{(z_i - Z_j)}{\int_{z_i}^{z_j} \frac{dz}{c(z)}} \tag{3.26}$$

(this equation also holds for $Z_j < z_i$). Newton's method is employed to refine the original estimate for the ray parameter using a Taylor's series expansion of $r(p)$ to first order about p_0 leading to

$$p_1 = p_0 + \left[\frac{\partial r(p_0)}{\partial p}\right]^{-1} (r(p) - r(p_0)), \tag{3.27}$$

with $\partial r/\partial p$ calculated as

$$\frac{\partial r}{\partial p} = \int_{z_i}^{z_j} \frac{c(z)dz}{[1 - p^2 c^2(z)]^{3/2}}. \tag{3.28}$$

The range value obtained for this value of p_1, computed using Eq. (3.25), is compared to the required range as defined by Eq. (3.23), and if it is deemed to be satisfactory the algorithm has found the needed value for p. If the computed range is outside of tolerance, the starting value is updated $p_0 \leftarrow p_1$ and the process is repeated iteratively until convergence. Once the p value has been found, the ray travel time can be computed using Eq. (3.24). Since Newton's method converges quadratically, this approach can be much faster for finding the ray parameter p than other methods such as bisection.

3.4 Ray Partial Derivatives

The linearized inversion methods described in Chapter 2 require partial derivatives of ray travel-time with respect to all parameters, including source position (x_i, y_i, z_i), hydrophone position (X_j, Y_j, Z_j), source transmission instant (t_0), and sound-speed bias (c_b). Differentiating and combining Eqs. (3.23)–(3.25) with respect to p, r, and the horizontal coordinates, respectively, and applying Leibnitz's rule, the horizontal constituents of the Jacobian matrix can be calculated as (Dosso & Ebbeson, 2006)

$$\frac{\partial t}{\partial x_i} = p(x_i - X_j)/r, \tag{3.29}$$

$$\frac{\partial t}{\partial X_j} = p(X_j - x_i)/r, \tag{3.30}$$

$$\frac{\partial t}{\partial y_i} = p(y_i - Y_j)/r, \tag{3.31}$$

$$\frac{\partial t}{\partial Y_j} = p(Y_j - y_i)/r. \tag{3.32}$$

The partial derivative with respect to the vertical component z_i can be determined as

$$\frac{\partial t}{\partial z_i} = \int_{z_i}^{z_j} \frac{pc(z)dz}{[1 - p^2c^2(z)]^{3/2}} \left(\frac{\partial p}{\partial z_i}\right) - \frac{1}{c(z)[1 - p^2c^2(z)]^{1/2}} \tag{3.33}$$

but requires an expression for $\partial p / \partial z_i$, which can be obtained by noting that

$$\frac{\partial r}{\partial z_i} = 0 = \int_{z_i}^{z_j} \frac{c(z)dz}{[1 - p^2c^2(z)]^{3/2}} \left(\frac{\partial p}{\partial z_i}\right) - \frac{pc(z)}{[1 - p^2c^2(z)]^{1/2}}. \tag{3.34}$$

Substituting the solution to $\partial p / \partial z_i$ back into Eq. (3.33) we obtain

$$\frac{\partial t}{\partial z_i} = \frac{1}{c(z_i)}[1 - p^2c^2(z)]^{1/2}. \tag{3.35}$$

Similarly for the hydrophone vertical component

$$\frac{\partial t}{\partial Z_j} = \frac{1}{c(Z_j)}\left[1 - p^2c^2(Z_j)\right]^{1/2}. \tag{3.36}$$

A path-dependent time correction factor τ_j is applied in certain situations, where there is a need to account for a laterally-varying SSP by adding a different correction factor to the observed arrival times at each hydrophone, for one or more source transmissions, to produce a corrected time for each source transmission as

$$t_{ij} = t_{0_i} + \tau_j + \int_{z_i}^{z_j} \frac{dz}{c(z)[1 - p^2c^2(z)]^{1/2}} \quad \text{for } i = 1,..,S, \quad j = 1,..,H. \tag{3.37}$$

For numerical stability, when implementing Eq. (3.24), the time correction parameter τ_j is multiplied by a (constant) representative sound speed factor of $\bar{c}$, and the arrival time is

$$t_{ij} = t_{0_i} + \frac{1}{\bar{c}}\left(\bar{c}\tau_j\right) + \int_{z_i}^{z_j} \frac{dz}{c(z)[1 - p^2c^2(z)]^{1/2}}, \tag{3.38}$$

where the unknown path correction is taken to be $\bar{c}\tau_j$ (rather than τ_j). To eliminate the need to estimate the transmission instant, TDOAs are calculated as the difference of arrival times at hydrophone *j* and hydrophone 1

$$t_{d_{ij}} = \frac{1}{\bar{c}}\left(\bar{c}\delta\tau_j\right) + \int_{z_i}^{z_j} \frac{dz}{c(z)[1 - p^2c^2(z)]^{1/2}} - \int_{z_i}^{z_1} \frac{dz}{c(z)[1 - p^2c^2(z)]^{1/2}} \quad \text{for } i = 1,..,S, \; j = 2,..,H. \tag{3.39}$$

where $\delta\tau_j = \tau_j - \tau_1$. The expression for the time derivative with respect to the correction factor is therefore

$$\frac{\partial t}{\partial\left(\bar{c}\delta\tau_j\right)} = \frac{1}{\bar{c}}. \tag{3.40}$$

The final component of the Jacobian matrix is the time derivative with respect to sound-speed bias, c_b. This term is representative of the bias error that can occur in sound-speed profile measurements due to inexact calibration of instruments, as $c(z) = c_t(z) + c_b$, where $c_t(z)$ is the true, unbiased sound-speed profile. The time derivative with respect to c_b is found by differentiating Eq. (2.24) with respect to c_b as

$$\frac{\partial t}{\partial c_b} = \int_{z_i}^{z_j} \frac{dz}{c^2(z)[1 - p^2c^2(z)]^{1/2}}. \tag{3.41}$$

3.5 Discretization

In practice, the equations in Sec. 3.4 can be implemented by assuming that the continuous sound-speed profile is represented by a series of discrete layers in a piece-wise linear

profile, $\{(z_k, c_k), k = 1, N_z\}$ with each layer having its own non-zero constant gradient, $g_k = {(c_{k+1} - c_k)}/{(z_{k+1} - z_k)}$. In this case, substituting $w_k = (1 - p^2c^2)^{1/2}$, the equations above for direct rays can be evaluated as (Dosso & Ebbeson, 2006),

$$r = \sum_{k=j}^{i-1} \frac{w_k - w_{k+1}}{p g_k} \tag{3.42}$$

$$t = t_0 + \sum_{k=j}^{i-1} \frac{1}{g_k} \left[\log_e \frac{c_{k+1}(1 + w_k)}{c_k(1 + w_{k+1})} \right] \tag{3.43}$$

$$c_H = (z_i - Z_j) \left[\sum_{k=j}^{i-1} \frac{1}{g_k} \left[\log_e \frac{g_k(z_{k_1} - z_k) + c_k}{c_k} \right] \right]^{-1} \tag{3.44}$$

$$\frac{\partial r}{\partial p} = \sum_{k=j}^{i-1} \frac{w_k - w_{k+1}}{p^2 g_k w_k w_{k+1}} \tag{3.45}$$

$$\frac{\partial t}{\partial c_b} = \sum_{k=j}^{i-1} \frac{1}{g_k} \left[\frac{w_{k+1}}{c_{k+1}} - \frac{w_k}{c_k} \right]. \tag{3.46}$$

3.6 Turning Rays

If a non-turning ray cannot be found to connect source and receiver, the ray-tracing algorithm must search for a turning ray. The average sound-speed gradient between the source and receiver is used to determine whether a connecting ray is more likely to have turned upwards or downwards. The aim is to trap the eigenray by seeking rays that turn at the top (for a negative average gradient; bottom for a positive gradient) of each sound-speed layer and finding two rays that bracket the receiver, then refining the position using the bisection method (Dosso & Ebbeson, 2006).

For the case of a source located above a receiver in z with a downward-refracting profile, the first rays considered are those from take-off angles travelling upwards, to determine if they turn back downwards towards the receiver. An effective strategy for this is to determine which rays turn at the top of each layer of the sound-speed profile above the source. If the sound speed gradient in layer k, g_k is less than zero, the value of p for an upward propagating ray at the top of the this layer is determined to be

$$p = {c_k}^{-1}. \tag{3.47}$$

If rays that turn at successive layer boundaries bracket the receiver, the bisection method is used to refine the estimate of p to within the prescribed range tolerance. If eigenrays cannot be found to bracket the receiver using this method, a secondary search over downward-propagating rays turning upwards below the receiver is carried out. For the case of an upward-refracting profile, the progression begins by searching for rays that turn upwards at layer boundaries below the receiver before carrying on to rays that turn downward above the source.

If a turning eigenray is found (i.e., its p-value is determined), ray-path integrals are calculated. Considering an initially downward propagating ray entering the lth layer with $g_l > 0$, the turning depth for this ray is

$$z_T = z_l + \left({}^{1}/_{p} - c_l\right){g_l}^{-1}. \tag{3.48}$$

If this depth is less than z_{l+1}, the boundary of the next layer, the ray must turn in this layer; if not, the ray crosses the boundary into the next layer. For a ray that is found to turn in layer l, the integration is described in four steps: (i) integrate from the source depth (z_i) to the layer depth in which the ray turns (z_l), (ii) integrate from the top of the

layer (z_l) to the depth within the layer at which the ray turns (z_T), (iii) integrate back upwards from z_T to z_l, and (iv) z_l to z_i. The integrals are evaluated numerically and expressed as sums, and for turning rays can now be given as (Dosso & Ebbeson, 2006)

$$r = \sum_{k=i}^{l-1} \frac{w_k - w_{k+1}}{p g_k} + \frac{2w_l}{p g_l} + \sum_{k=l}^{j} \frac{w_k - w_{k-1}}{p g_{k-1}}, \tag{3.49}$$

$$t = t_0 + \sum_{k=i}^{l-1} \frac{1}{g_k} \left[\log_e \frac{c_{k+1}(1 + w_k)}{c_k(1 + w_{k+1})} \right] + \frac{2}{g_l} \log_e \frac{1 + w_l}{p c_l} + \sum_{k=l}^{j} \frac{1}{g_{k-1}} \left[\log_e \frac{c_{k-1}(1 + w_k)}{c_k(1 + w_{k-1})} \right], \tag{3.50}$$

$$\frac{\partial r}{\partial p} = \sum_{k=i}^{l-1} \frac{w_k - w_{k+1}}{p^2 g_k w_k w_{k+1}} - \frac{2}{g_l p^2 w_l} + \sum_{k=l}^{j} \frac{w_k - w_{k-1}}{p^2 g_{k-1} w_k w_{k-1}} \tag{3.51}$$

$$\frac{\partial t}{\partial c_b} = \sum_{k=i}^{l-1} \frac{1}{g_k} \left[\frac{w_{k+1}}{c_{k+1}} - \frac{w_k}{c_k} \right] + \frac{2w_l}{c_l g_l} + \sum_{k=l}^{j} \frac{1}{g_{k-1}} \left[\frac{w_{k-1}}{c_{k-1}} - \frac{w_k}{c_k} \right]. \tag{3.52}$$

4 Modelling Uncertainty

The recent paper (Thomson, *et al.*, 2012), reformatted to constitute this chapter, provides a discussion of the sources and effects of source-location uncertainty within the positioning system. The introductory section of the paper has been included in this chapter, and will repeat some of the more important concepts developed over the preceding chapters before presenting the results of the simulation study. The algorithm described in this chapter inverts for a transmission instant, as explained in Section 4.2, rather than TDOA, as in the remainder of this thesis.

4.1 Introduction

Precise positioning of autonomous underwater vehicles (AUVs) is an important problem for the ocean science community as it attempts to extend its reach further into the depths of the ocean. Terrestrial Global Positioning Systems (GPS) are of little use for an underwater target as the high-frequency/low-power signals they employ are unable to penetrate beyond the surface layers of the ocean due to reflection and absorption by the seawater. The Integrated Acoustic System (IAS) being designed by the University of Victoria's Ocean Technology Test Bed (OTTB) team aims to overcome this obstacle by developing a high-precision underwater acoustic positioning system. The goal is to produce a system, similar to a commercial Long Baseline unit, capable of positioning a target within the OTTB range to a sufficient accuracy for use as a ground truth for testing onboard navigation systems.

The range itself covers an area of approximately 1.5 km by 1.5 km, with five hydrophones moored to 3-m towers on the seabed at depths of 60 m to 130 m and located in the four corners of the range plus one near the centre, as depicted in Fig. 4.1. With the origin of the coordinate system at the lower left-hand corner of the range (as shown in Fig. 4.3 and following), this is a left-hand coordinate system. The N-S axis is referred to as *y* while the E-W axis is aligned to *x*, with *z* being depth below surface. The AUV will be outfitted with a generic 'pinger', a transducer that periodically emits an acoustic pulse in the 5–80 kHz frequency range as it moves about the range. The pulse travels through the underwater medium, and is received at the five hydrophones stations (Gamroth, Kennedy & Bradley, 2011).

The received ping arrival instants represent the data, which are used to estimate the source position using the time difference of arrival through a ray-based linearized inversion technique. The error in the source position estimate is a function of clock error in the Precision Time Protocol (PTP) system ($\pm 10\ \mu s$), tower position survey error (± 0.40 m in each of three dimensions expected), and errors in the measured sound-speed profile (due to instrument bias). Positional uncertainty is also affected to a large degree by the source-hydrophone geometry.

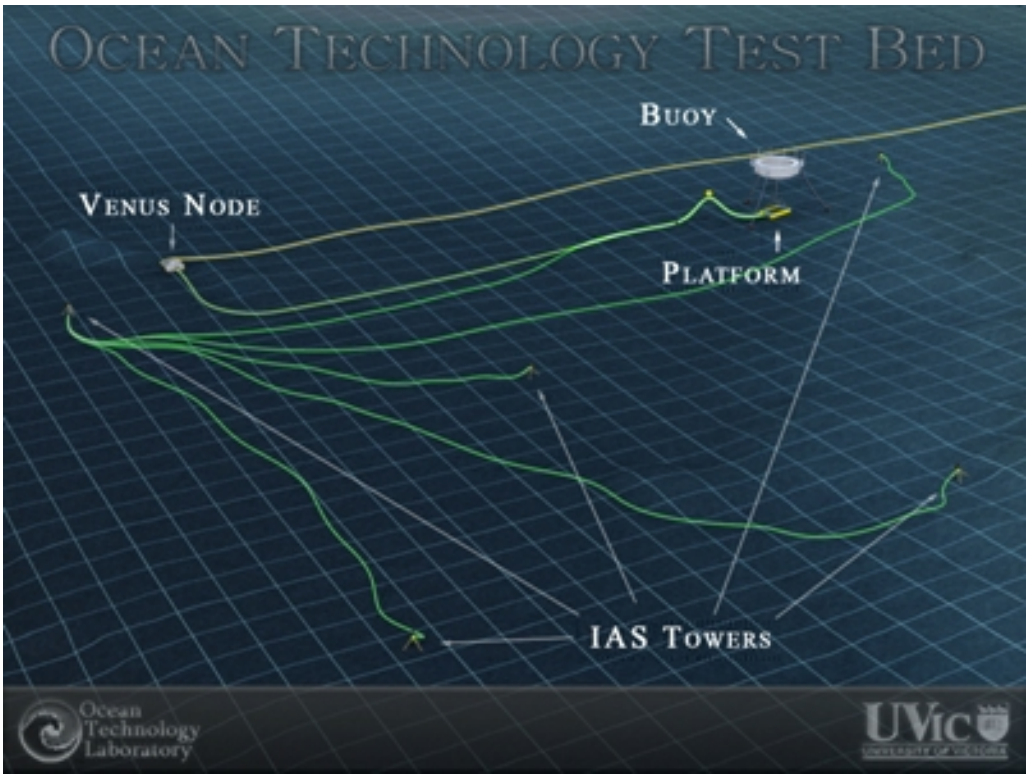

Figure 4.1: Conceptual image of the OTTB range located in Saanich Inlet, near Victoria, BC, showing the five hydrophone tower locations and a grid representing the simulated target positions (Ocean Technology Test Bed, 2005).

The sound-speed profiles used in this investigation are shown in Figure 4.2. The solid-line profile was obtained from direct sound-speed measurements using a velocimeter cast at the range in Saanich Inlet, on November 8, 2011, a day with calm winds. The dashed-line profile was derived from temperature and salinity data collected by Zaikova et al. (2010) within Saanich Inlet but outside the OTTB range during February, 2008. Once the range is operational, the protocol will call for collection of a sound-speed profile within a few hours of data collection for use in target positioning.

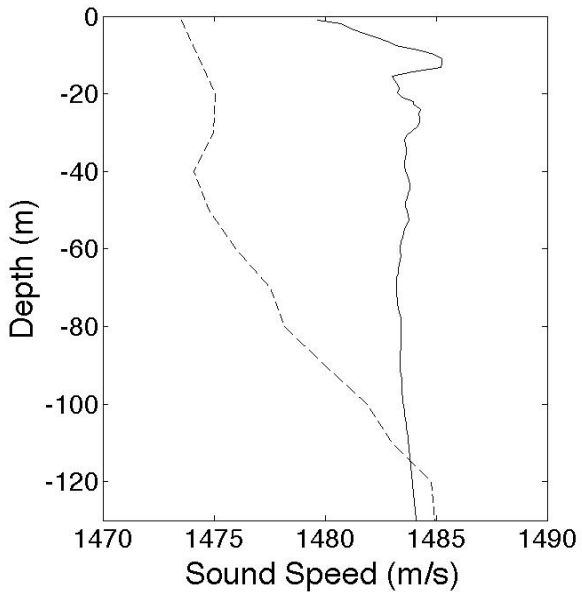

Figure 4.2: Sound-speed profiles used in the simulations. The solid-line profile was collected during November, 2011. The dashed-line profile was collected by Hallam & Tortell (2008) during February, 2008.

To examine the anticipated localization accuracy of the system, a simulation procedure was developed which calculates uncertainties for a series of positions about the range. The remainder of this paper describes the inversion algorithm used to compute localization uncertainties (Section 4.2) and gives a series of examples considering a variety of factors that affect the accuracy (Section 4.3).

4.2 Method

The modelling study carried out here to estimate the localization accuracy for a target located within the range is based on estimating the posterior uncertainties of the source-location in x, y, and z. Since the source-location uncertainty varies with source location, uncertainties are calculated for the source at each point within a grid of positions over the

area of the test bed. At each grid point, the source-location uncertainties are estimated using a linearized Bayesian approach that includes the effects of arrival-time errors as well as uncertainties in hydrophone locations and sound speed. A complete description of these methods can be found in Dosso & Ebbeson (2006). The lateral (r) uncertainty is calculated as the square root of the L_2 norm of the horizontal (x and y) uncertainty components.

The OTTB range is modelled as a range-independent, layered ocean using a measured sound-speed profile. The data set $\mathbf{t}$ is the vector of $N = H$ measured ray arrival times at the $H = 5$ hydrophone stations, while the model $\mathbf{m}$ is a vector of $M = 3H + 5$ parameters representing source locations (x, y, z), hydrophone positions ($X_i, Y_i, Z_i \;\; i = 1, \ldots, 5$), source instant ($t_0$), and an unknown constant bias to the sound-speed profile (Δc) as

$$\mathbf{m} = \begin{bmatrix} x, y, z, \bar{c}t_0, X_1, Y_1, Z_1, \ldots, X_i, Y_i, Z_i, \Delta c \\ for \;\; i = 1, \ldots, 5 \end{bmatrix}^T, \tag{4.1}$$

where the source instant t_0 is multiplied by $\bar{c}$, a representative sound speed, to provide the same units and scale as positional parameters.

The observed data $\mathbf{t}$ are the arrival times of pings originating from the target and received at the five hydrophone stations for each given source transmission. These data contain noise (errors) as discussed in Section 4.1, and the direct path ray arrival times $\mathbf{t}$ can be written in general vector form as

$$\mathbf{t} = \mathbf{t}(\mathbf{m}) + \mathbf{n}, \tag{4.2}$$

where $\mathbf{t}(\mathbf{m})$ are the predicted data based on the model parameters $\mathbf{m}$, i.e., the calculated travel times along eigenrays connecting source and receivers, and $\mathbf{n}$ are errors on the

data. The error n_i on datum t_i is assumed to be an independent Gaussian-distributed random process with zero mean and standard deviation σ.

Expanding $\mathbf{t}(\mathbf{m})$ in a Taylor series to first order about an arbitrary starting model $\mathbf{m_0}$, the result can be written

$$\mathbf{d} = \mathbf{J}\mathbf{m}, \tag{4.3}$$

where

$$\mathbf{d} = \mathbf{t}(\mathbf{m}) - \mathbf{t}(\mathbf{m_0}) + \mathbf{J}\mathbf{m_0} \tag{4.4}$$

are modified data and $\mathbf{J}$ is the Jacobian matrix of partial derivatives of the data functionals with respect to the model parameters evaluated at $\mathbf{m_0}$:

$$J_{ij} = \partial d_i(\mathbf{m_0})/\partial m_j \tag{4.5}$$

This matrix is sometimes called the sensitivity matrix as it quantifies the sensitivity of the data to the model, and contains the physics and geometry of the forward problem.

Prior information about the model parameters is also considered in the problem. Assuming this prior information represents a Gaussian uncertainty distribution with expected values $\widehat{m}_k$ (the prior estimate for the *k*th parameter) and standard deviations ξ_k, the maximum *a posteriori* (MAP) solution is given by

$$\mathbf{m}_{\mathrm{MAP}} = \widehat{\mathbf{m}} + \left[\mathbf{J}^{\mathrm{T}}\mathbf{C_d}^{-1}\mathbf{J} + \mathbf{C_p}^{-1}\right]^{-1}\mathbf{J}^{\mathrm{T}}\mathbf{C_d}^{-1}(\mathbf{d} - \mathbf{J}\widehat{\mathbf{m}}) \tag{4.6}$$

where $\mathbf{C_d} = \sigma^2\mathbf{I}$ is the data covariance matrix and $\mathbf{C_p} = \mathrm{diag}\{\xi_k{}^2\}$ is the prior model covariance matrix. Further, the posterior probability density is a Gaussian distribution about $\mathbf{m}_{\mathrm{MAP}}$ with posterior model covariance matrix

$$\mathbf{C_m} = \left[\mathbf{J}^{\mathrm{T}}\mathbf{C_d}^{-1}\mathbf{J} + \mathbf{C_p}^{-1}\right]^{-1}. \tag{4.7}$$

The square root of the diagonal elements of $\mathbf{C_m}$ provide posterior standard deviation (uncertainty) estimates for the model parameters.

Equation (4.7) represents a linearized approximation in this problem; however, comparison to non-linear solutions from Monte Carlo analysis (Dosso & Sotirin, 1999) indicates that linearization errors are small if $\mathbf{m_0}$ is close to the true model. When inverting measured data linearization errors are minimized by iterating the linearized solution to convergence.

The inversion techniques described above are based on a fast ray-tracing algorithm that uses Newton's method to determine eigenrays; analytic expressions for the ray derivatives are available for the Jacobian matrix (Dosso & Ebbeson, 2006). Uncertainties in x, y, z, and $r = \sqrt{x^2 + y^2}$ are taken from Eq. (4.7) and used to quantify the expected localization accuracy.

4.3 Results

A series of simulations is presented here to compare the effects on localization accuracy of several factors: hydrophone positioning and sound-speed uncertainty, different source depths, and the effect of reducing target vertical positioning uncertainty through the addition of a depth sensor. The results of increased and decreased timing errors are also considered, as well as different sound-speed profiles and hydrophone geometric configurations.

The first simulation considers what is referred here to as the 'ideal-case' scenario, where the hydrophone positional uncertainty and the sound-speed profile bias are both assumed to be zero, with the timing uncertainty set to the PTP limit of 10 μs. The source

depth is 10 m, and the sound-speed profile is the solid line from Fig. 4.2. This represents the simplest case where only the uncertainty due to the system timing error is considered. The results of this simulation are shown in Figure 4.3 in terms of *x*, *y*, *r*, and *z* uncertainties (colour contours) over the area of the range, in 10-m^2 blocks extending from the origin to 1600 m in *x* and 1400 m in *y*. The reader should note that the scale in *z* differs from the remaining components of uncertainty for all figures.

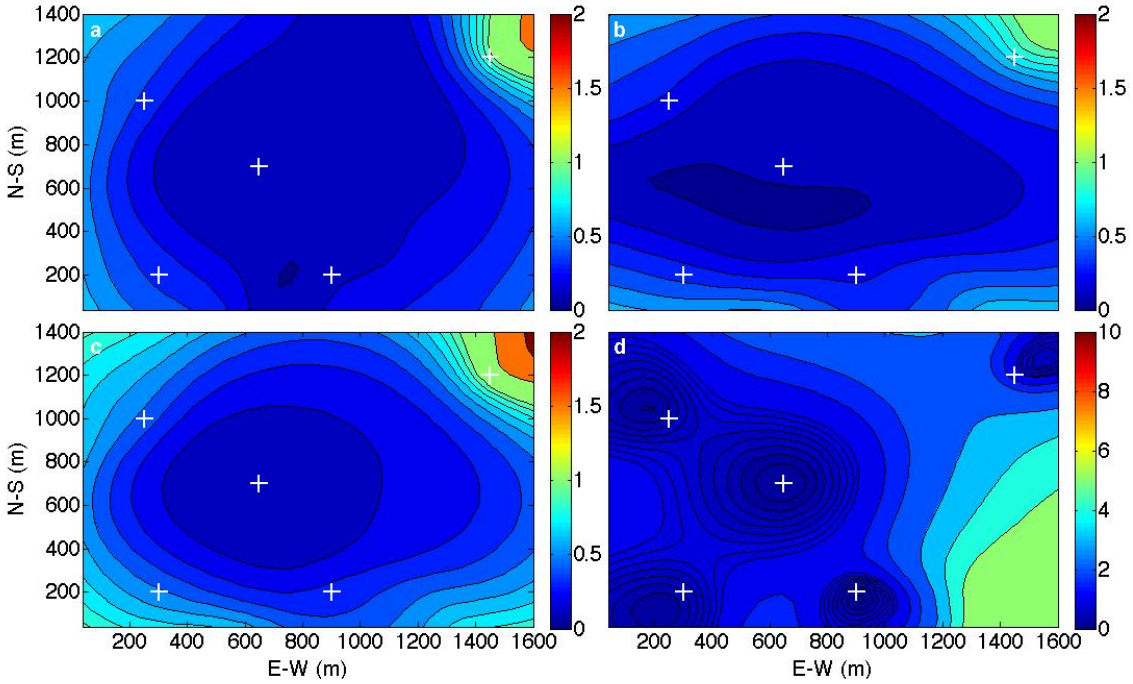

Figure 4.3: Localization uncertainties for the 'ideal case' of perfectly known hydrophone locations and sound-speed profile. Panels (a)–(d) show absolute errors in *x*, *y*, *r*, and *z*, respectively, for a source at 10-m depth. Contours represent uncertainty in metres. Hydrophone locations are depicted as white crosses.

The effects of source/hydrophone geometry are immediately visible in Fig. 4.3. The smallest uncertainty in *x* is found for a source located between two or more hydrophones

in x; similarly, the lowest uncertainty in y occurs for a source between two or more hydrophones in y. The most accurate vertical positioning tends to occur for the source locations nearest a hydrophone, where the acoustic ray travels nearly vertically. The greatest horizontal uncertainty occurs for a source in the corners of the range, where the source/hydrophone geometry is poor; the greatest vertical uncertainty tends to occur for a source furthest from a hydrophone, because the greatest amount of vertical information is contained in rays that arrive at steep vertical angles at the hydrophone, since the ratio of vertical distance to total ray path distance decreases with increasing horizontal distance from source to receiver.

In the second example, the uncertainty from the 'standard case' is examined, where the timing uncertainties remain at 10 μs, the hydrophones have positional uncertainties of 0.40 m in x, y, and z, and the sound-speed profile has an uncertainty (bias) of 1 m/s. The target depth is again set to 10 m. The results of the simulation are shown in Fig. 4.4. The uncertainties are much greater than in the 'ideal case', indicating that relatively small uncertainties in hydrophone location and sound-speed profile can have a significant effect on AUV localization accuracy and must be taken into account in a meaningful modelling study.

The smallest uncertainties for the x component in Fig. 4.4(a) are found in the middle of the range and aligned N-S, as these locations produce the most favourable hydrophone geometry for estimating the position in x, due to the rays arriving with large x components. Similarly for the y component, in Fig. 4.4(b), the smallest uncertainties also tend to the centre but the alignment is E-W. Additionally, the horizontal uncertainty components tend to be lower in the southern and western regions of the range, as the

northeastern hydrophone is asymmetrically located at a longer interval than the typical spacing between other hydrophones. This greater span increases the region of poor geometry within the range (where localization performance is poor due to source-hydrophone geometrical configuration), whereas in the south and west regions, a higher proportion of the area produces favourable geometric alignments in *x* and *y*.

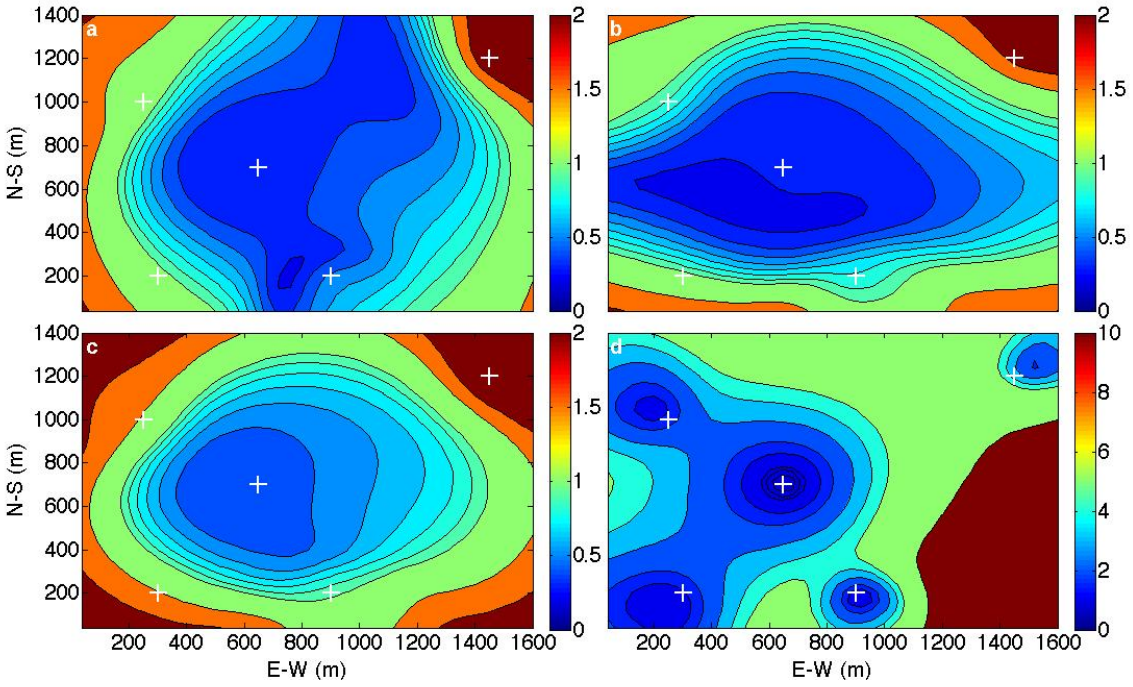

Figure 4.4: Localization uncertainties for the 'standard-case' scenario. Panels (a)–(d) show absolute errors in *x*, *y*, *r*, and *z*, respectively, for a source at 10-m depth. Colour contours represent uncertainty in metres. Hydrophone locations are depicted as white crosses.

Figure 4.4(c) shows the uncertainty in *r*, which combines the uncertainty of *x* and *y*. The region of small uncertainty has a rounded symmetrical shape as opposed to the linear shape in the individual *x* and *y* components, and the combined uncertainty is always

greater than either constituent component. The vertical uncertainty in Fig. 4.4(d) is lowest for a target located close to any hydrophone, with increasing uncertainty for targets that are further away from a hydrophone.

The effect of varying target depth is presented in Fig. 4.5, which shows the result for the same simulation parameters but with a target at 40-m depth. The horizontal results are similar to the 10-m depth case shown in Fig. 4.4; however, the geometric effects are more pronounced with the deeper target, due to the reduced vertical extent between source and receiver. The uncertainty in z increases for the deeper target especially in areas of the range distant from a hydrophone, where uncertainty is relatively high. This scenario was repeated for multiple source depths (not shown). For targets at greater depths, the vertical uncertainty increases, since the ray arrives at the hydrophone more horizontally, providing less vertical information about the target position. Hence, the IAS system is ineffective at estimating the depth of a deep source.

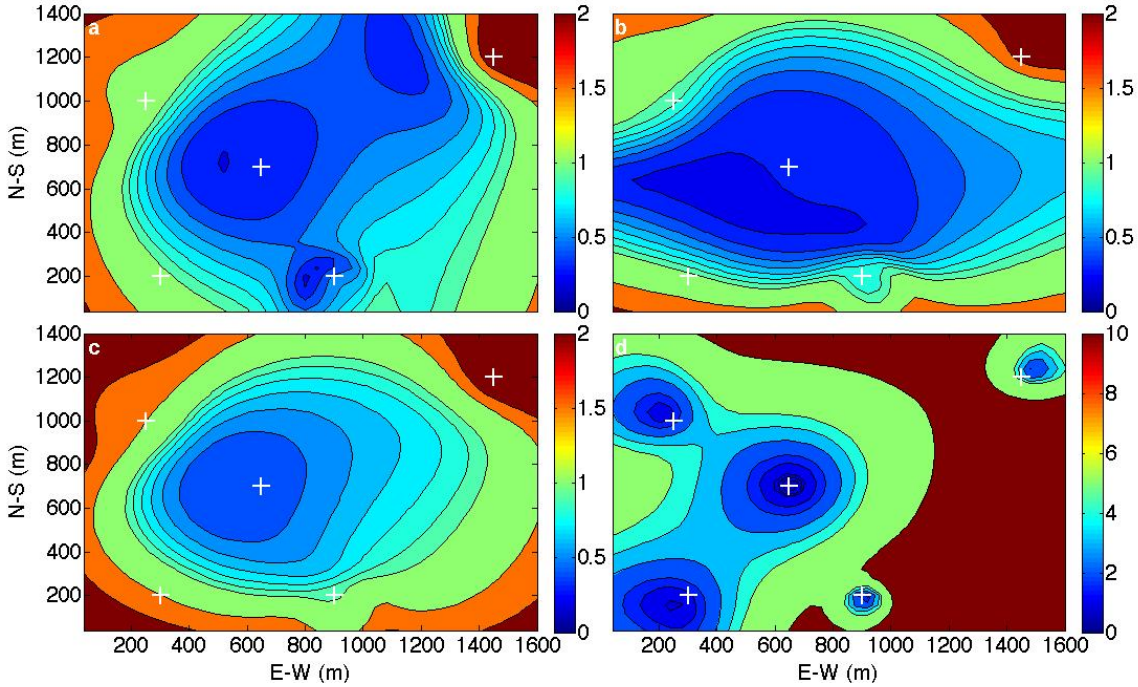

Figure 4.5: Localization uncertainties for the 'standard-case' scenario. Panels (a)–(d) show absolute errors in x, y, r, and z, respectively, for a source at 40-m depth. Colour contours represent uncertainty in metres. Hydrophone locations are depicted as white crosses.

In investigating ways to overcome this limitation and to improve overall uncertainty, a scenario was simulated where the target is outfitted with a depth sensor, so that its vertical positioning is always known to within 0.03 m, shown in Fig 4.6. In this simulation the posterior uncertainty in z is ≤ 0.03 m throughout the range. The effect of this improved z uncertainty on the lateral uncertainty varies depending on the location within the range. For the locations with relatively low uncertainty (those with the most favourable geometry), the uncertainty is improved only slightly, typically on the order of 2%. However, in the regions where uncertainty is high, as well as locations near a hydrophone, the improvement is much more significant: as much as 70%.

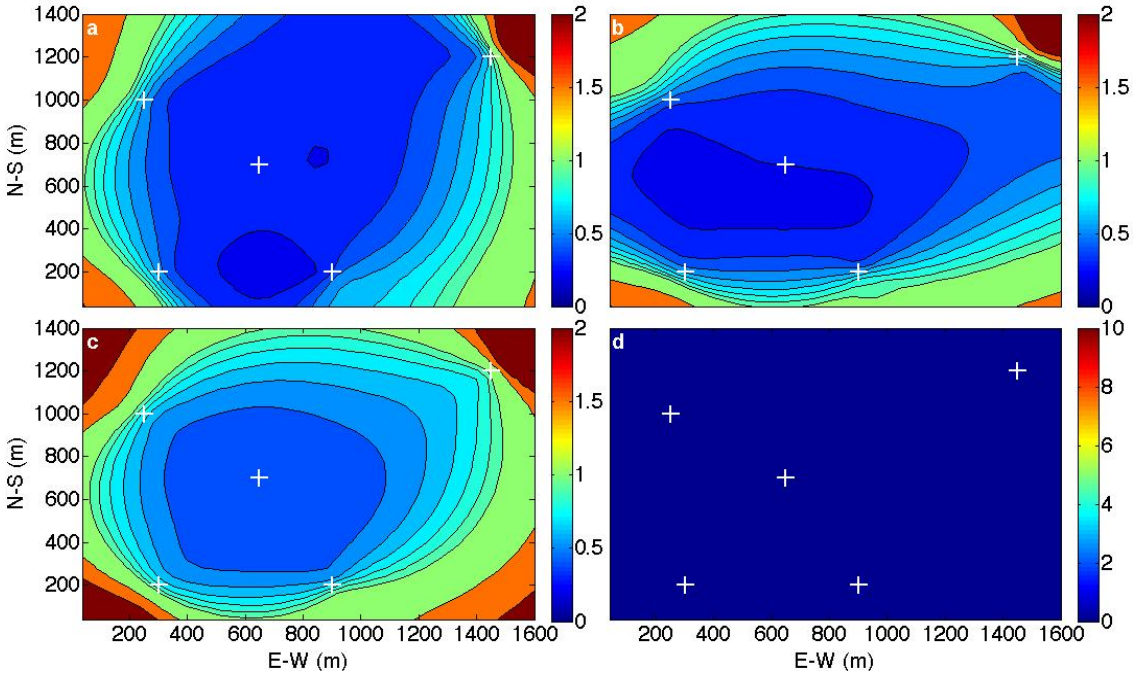

Figure 4.6: Localization uncertainties for the 'depth-sensor case' scenario with target position in *z* assumed to be known to within 0.03 m uncertainty. Panels (a)–(d) show absolute errors in *x*, *y*, *r*, and *z*, respectively, for a source at 10-m depth. Colour contours represent uncertainty in metres. Hydrophone locations are depicted as white crosses.

To consider next the effect of timing errors, a simulation was run where the timing uncertainty was increased by a factor of 100 to 1 ms. The results are presented in Fig. 4.7, and show that uncertainty is substantially increased for all components, indicating that timing uncertainty is an important contributor to overall target positional uncertainty. The 1 ms error was chosen because this is a representative timing accuracy in a typical system employing Network Timing Protocol, as opposed to the 10 µs accuracy achieved in a PTP network (Lentz & Lecroart, 2009). This finding indicates that a high-precision acoustic positioning system would not be feasible without a PTP network.

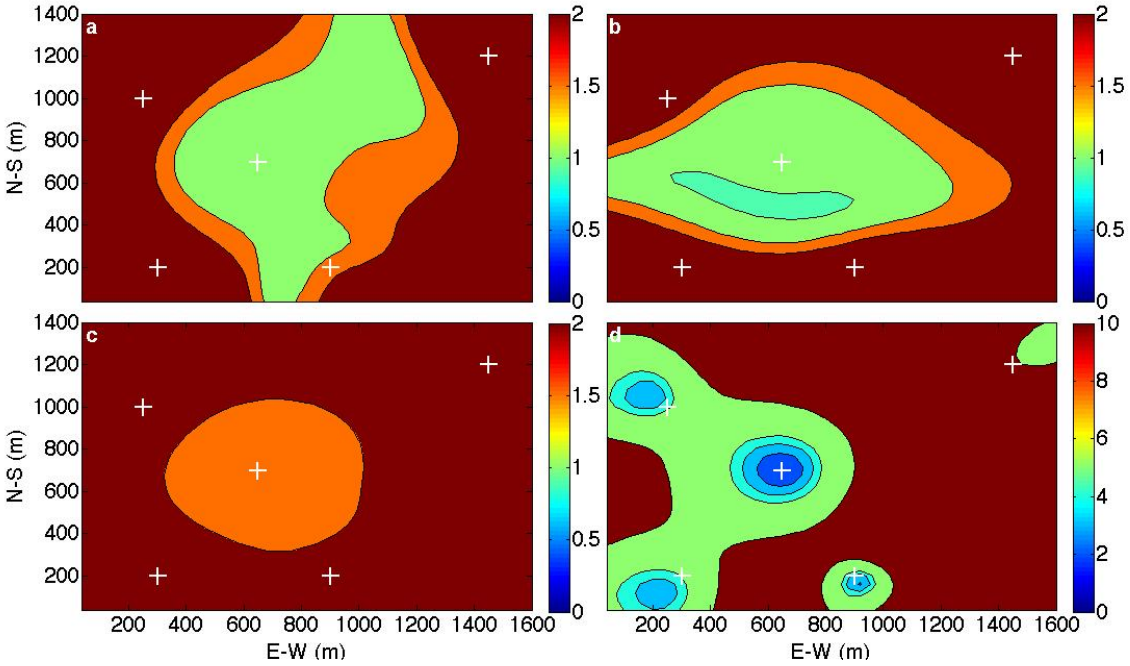

Figure 4.7: Localization uncertainties for the 'standard-case' scenario with a timing error of 1 ms. Panels (a)–(d) show absolute errors in *x*, *y*, *r*, and *z*, respectively, for a source at 10-m depth. Colour contours represent uncertainty in metres. Hydrophone locations are depicted as white crosses.

Another aspect of the PTP network is the potential to further increase the timing precision; it is anticipated that further development in network timing protocols will allow for timing precision to within 100s of nanoseconds (Lentz & Lecroart, 2009). These improvements could be incorporated into the IAS in the future, so a simulation was carried out reducing timing uncertainty by a factor of 100 to 100 ns, shown in Fig. 4.8. The results are virtually identical to the 'standard case' (Fig. 4.4) with timing uncertainty 100 times greater, indicating that there exists a limit, near the PTP timing uncertainty of 10 μs, beyond which the overall positional uncertainty is not impacted by further

improvement; rather, the uncertainty in hydrophone positions becomes the limiting factor.

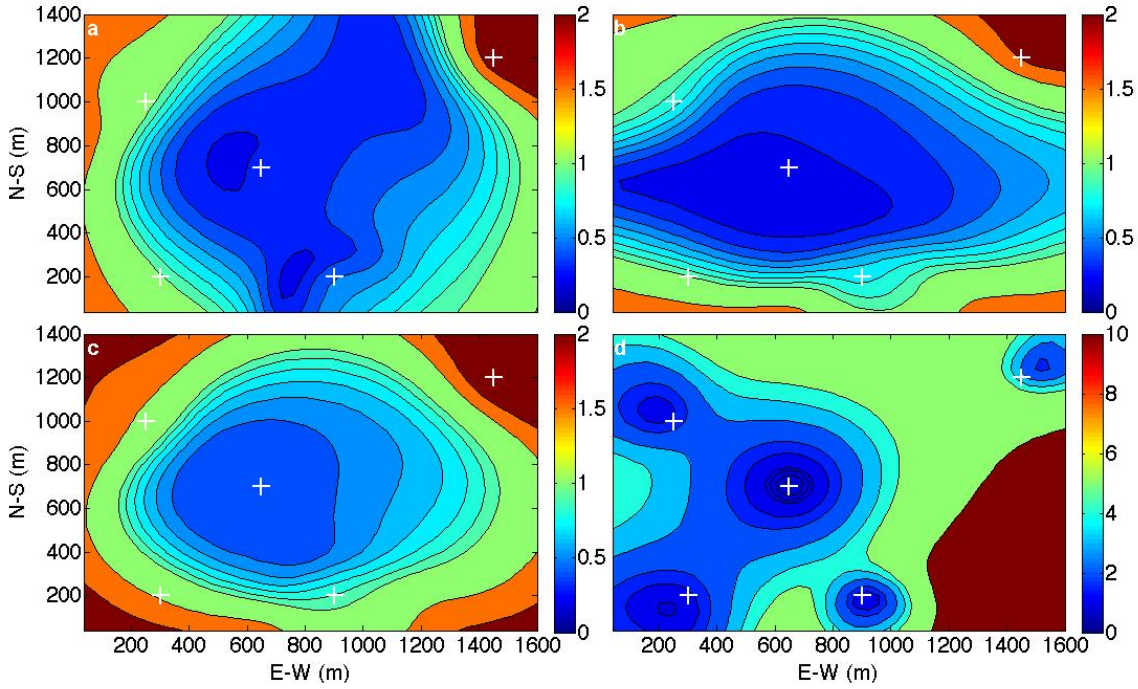

Figure 4.8: Localization uncertainties for the 'standard-case' scenario with a timing error of 100 ns. Panels (a)–(d) show absolute errors in *x*, *y*, *r*, and *z*, respectively, for a source at 10-m depth. Colour contours represent uncertainty in metres. Hydrophone locations are depicted as white crosses.

To determine whether the localization accuracy would be expected to vary significantly during the year as a function of seasonal variations to the sound-speed profile, Fig. 4.9 shows the 'standard-case' scenario run using the upward-refracting February profile shown in Fig. 4.2. The most notable difference from the standard-profile results (Fig. 4.4) is the increased uncertainty in the *x* and *y* components for target locations furthest from a hydrophone, and in *z* for target locations nearer a hydrophone.

However, the variation in uncertainty due to sound-speed profile difference is generally small, indicating that the IAS should function consistently throughout the year.

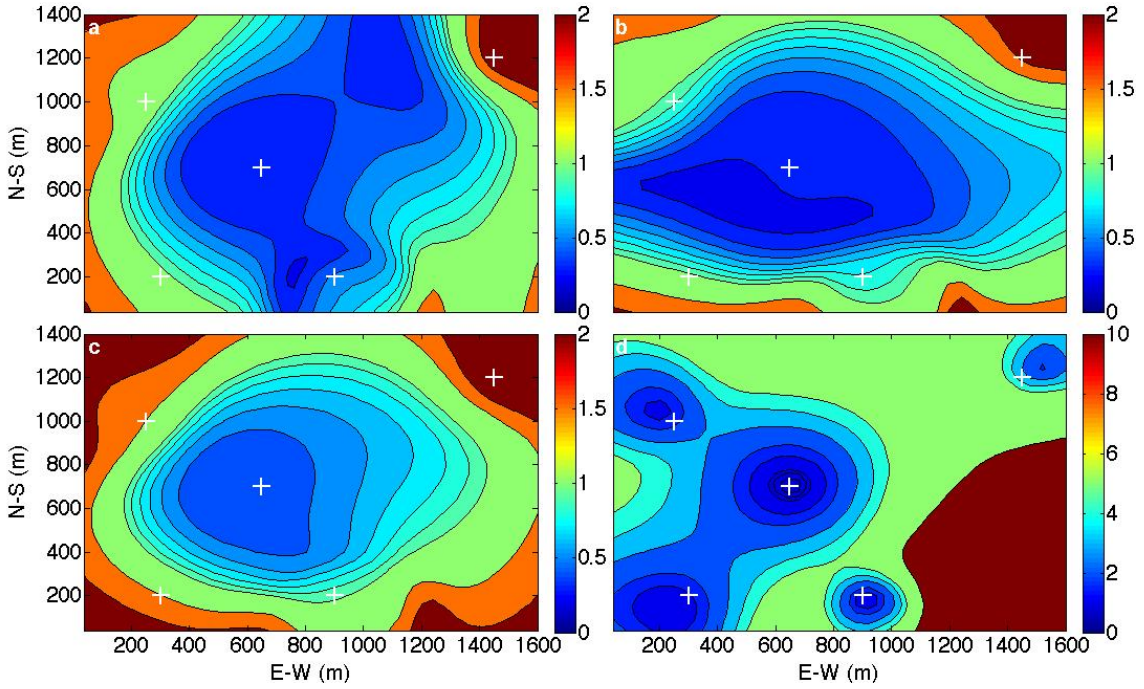

Figure 4.9: Localization uncertainties for the 'standard-case' scenario using a February sound-speed profile. Panels (a)–(d) show absolute errors in *x*, *y*, *r*, and *z*, respectively, for a source at 10-m depth. Colour contours represent uncertainty in metres. Hydrophone locations are depicted as white crosses.

Finally, a simulation was carried out investigating the effects of moving the NE hydrophone tower in line with the other hydrophones to create a more symmetric range. The results are presented in Fig. 4.10, and show that by moving this hydrophone closer to the others, the uncertainty improves slightly for target locations contained within the perimeter of hydrophones, but becomes substantially worse outside this perimeter.

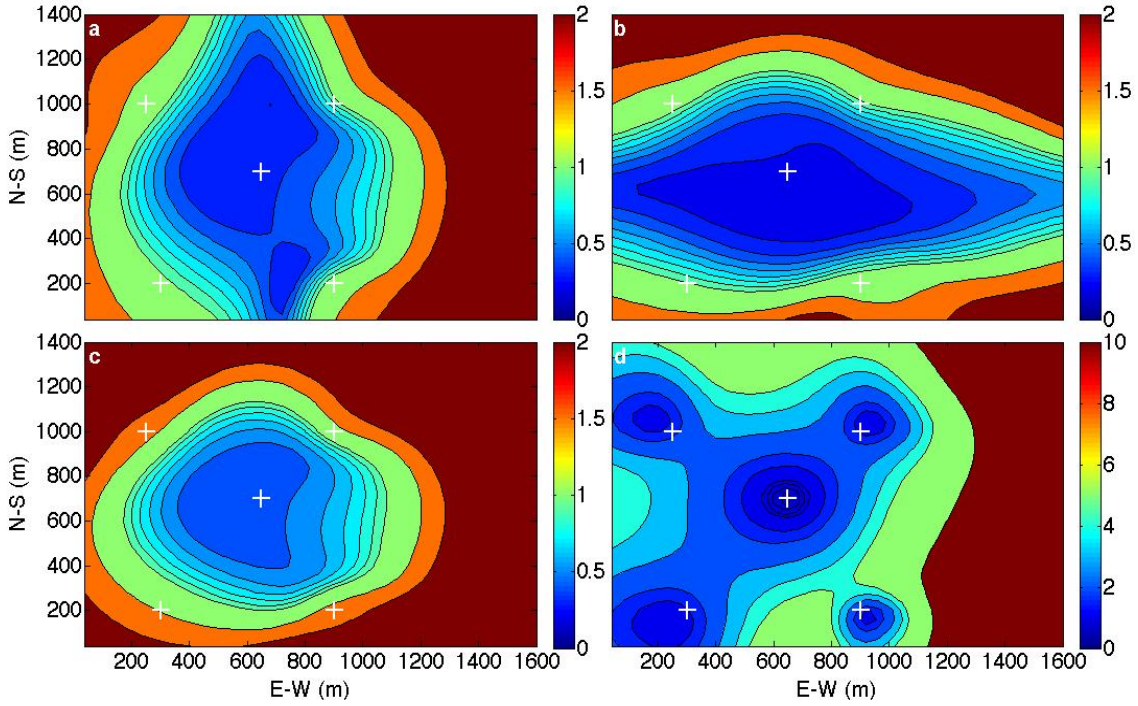

Figure 4.10: Localization uncertainties for the 'standard-case' scenario, relocating the NE hydrophone tower closer to the others. Panels (a)–(d) show absolute errors in x, y, r, and z, respectively, for a source at 10-m depth. Colour contours represent uncertainty in metres. Hydrophone locations are depicted as white crosses.

4.4 Discussion

This chapter developed and illustrated a simulation procedure to investigate localization accuracy for an underwater target (AUV) in an acoustic test range. The simulation procedure allows examination of the effects of several factors, which are integral to the overall system performance, and is a valuable tool for predicting localization accuracy in a variety of situations. Localization uncertainty is examined as a function of hydrophone positional uncertainty, sound-speed uncertainty, timing errors, and source depth. The effect of reducing target positional uncertainty by employing an AUV-mounted depth

sensor is also considered. Finally, different sound-speed profiles and hydrophone geometric configurations are examined.

The simulation is especially beneficial for determining the expected baseline uncertainty for the range given specific values for the system factors (e.g. timing errors, hydrophone-positional and sound-speed uncertainties). In determining whether a certain static accuracy throughout the range is a realizable goal, localization uncertainties can be computed using realistic values for these system factors. Further, the effect of varying these factors on localization accuracies can be quantified.

The simulations showed that for the standard case (timing uncertainties of 0.1 ms, hydrophone location uncertainties of 0.4 m, sound-speed uncertainties of 1 m/s, 10 m source depth) the minimum positional uncertainty at any point in the range was on the order of 40 cm laterally, and 70 cm vertically. These smallest lateral uncertainties occur near the centre of the range, while the smallest vertical uncertainties are generally found above hydrophones. The largest uncertainties, extending well above 1 m, occur towards the periphery of the range due to less favourable source/hydrophone geometry.

The simulations also show that for the existing range infrastructure, a high-precision acoustic positioning system is not feasible using standard network protocol due to the timing uncertainty. Using the PTP network timing, the timing accuracy is sufficient to allow high-precision positioning. However, the improvement in positional uncertainty from further development of the PTP timing uncertainty is negligible, indicating that the operational limit has been met for timing error improvement and improvement in hydrophone localization would be required.

While the methods described here are applied to the specific case of the University of Victoria's OTTB, the approach is general and can be applied to model and examine the accuracy of any underwater acoustic positioning system.

5 Simulation study

To examine the importance of several factors in source localization, a series of simulations is carried out in this chapter. Each simulation is executed for three distinct test cases that were developed to simulate target positions representing favourable source-receiver geometry, poor source-receiver geometry, and an average over geometries in terms of a series of random source positions drawn from within the range. The simulation scenarios were developed to investigate: (1) modelling transmission paths accounting for refraction due to a depth-varying SSP instead of using straight rays through a constant sound-speed approximation, (2) inverting for a potential sound-speed bias in the measured profile, (3) accounting for errors in hydrophone position by including these positions as unknowns in the inversion, and (4) applying path correction factors to account for lateral variability in the sound-speed profile. Each scenario is studied using a Monte Carlo method in which a large number of noisy data sets are inverted to derive statistical measures to quantify the various effects.

5.1 Simulation conditions

5.1.1 Test case source positions

Figure 5.1 shows the true source locations for the first two simulation test cases. Test case 1 is based on the target located roughly in the centre of the range close to the middle of the hydrophone configuration. This position is favourable for localization as the source is situated between hydrophones in both x and y providing good lateral information, and is almost directly above the centre hydrophone, providing good vertical information.

In test case 2, the target is located in a poor position in terms of hydrophone geometry, in the SE corner of the range and distant from the nearest hydrophone tower. In this case, rays arrive at the hydrophones at shallow vertical angles (<0.5°), providing less information about the *z* component, while rays provide redundant *x* and *y* information leading to a system of equations with weak linear independence.

In test case 3, the target position is selected randomly throughout the range and the statistics for the simulation scenarios are calculated for a large number of realizations, each time with a different random position.

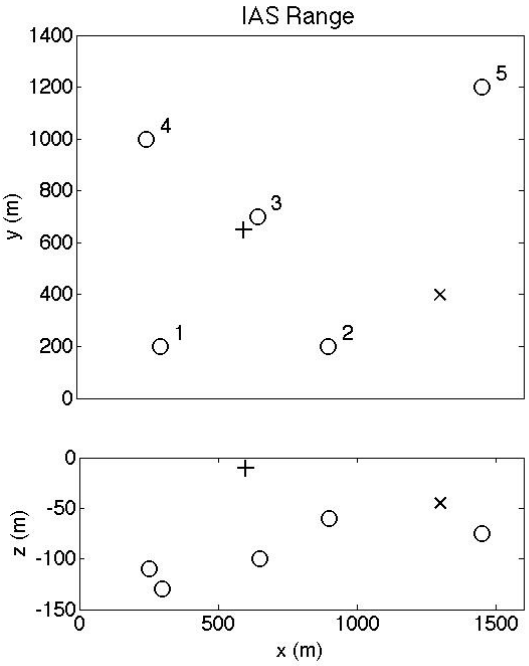

Figure 5.1: Source-receiver geometries. Source locations indicated by '+' for test case 1 and by 'x' for test case 2. Hydrophone positions indicated by circles, and numbered 1–5 in the top pane for identification

5.1.2 Simulated environment

The sound speed environment is modelled using several different SSPs, measured at different times of the year (September, November and December) and shown in Fig. 5.2.

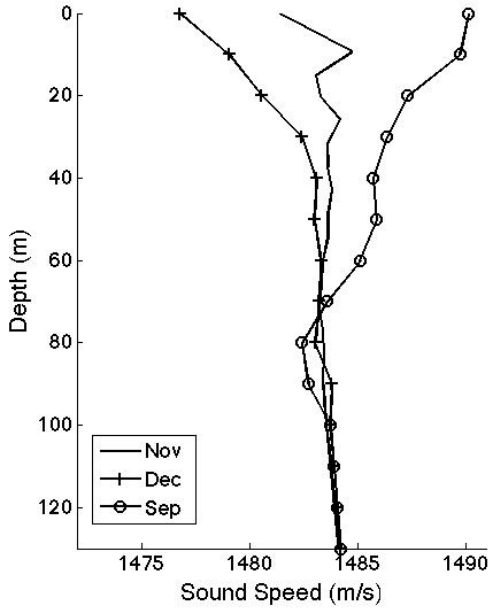

Figure 5.2: Sound-speed profile used for simulations.

Hydrophone positions are considered to be known perfectly (except in the case of Section 5.4 where the effect of hydrophone error is investigated). The target is assumed to be equipped with a sound source that transmits omni-directional pings, and the arrival time at each of the five hydrophones is computed using the ray-tracing algorithm described in Sections 3.4–3.6. For each source transmission received, the arrival time for hydrophone 1 (Fig. 5.1) is subtracted from the arrival times for hydrophones 2 to 5, to produce 4 arrival-time differences. This reduces the number of data available to find a

solution, but acts to stabilize the problem by eliminating the need to estimate transmission instant from the asynchronous source.

Prior information about the source position, as well as hydrophone positions, sound-speed bias, and path-correction factors, when applicable, are contained in the prior estimate vector ($\hat{\mathbf{m}}$) and its corresponding prior covariance matrix ($\mathbf{C_p}$). Some prior knowledge of the target's position is considered to be known, and the simulations presented here assume that the prior is a Gaussian distribution of standard deviation 50 m in *x* and *y* and 10 m in *z* about parameter estimates representing the true values (given in Table 5.1) plus a random perturbation of these standard deviations.

Parameter	True [x,y,z] value
Source (test case 1)	[600, 650, 10] m
Source (test case 2)	[1300, 400, 45] m
Source (test case 3)	[(0:1500), (0:1500), (1:50)] m
Hydrophone 1	[300, 200, 130] m
Hydrophone 2	[900, 200, 60] m
Hydrophone 3	[650, 700, 100] m
Hydrophone 4	[250, 1000, 110] m
Hydrophone 5	[1450, 1200, 75] m

Table 5.1: True source and hydrophone positions used in test cases. Random position for test case 3 chosen within the intervals given.

The system timing error is based on the PTP error of 10 μs described in Chapter 1. This timing error stems from the assumption that the system will operate with an efficient matched-filter system to identify the transmission arrival, and all hydrophones are

synchronized to within the PTP error via the underwater network. Timing errors are considered to be Gaussian-distributed random variables with zero-mean and standard deviation of 10 μs. Note that when considering the TDOA data, the standard deviation of the time differences are $\sqrt{2}\sigma$, where σ is the standard deviation of the arrival times (10 μs). All TDOA data are subject to these timing errors, which are quantified in the data error covariance matrix ($\mathbf{C_d}$).

5.1.3 Ray Tracing

The SSP is fundamentally important when modelling the path that a ray will take from the source to the receiver. For this modelling study, November, September and December profiles are used for simulations, and an example of some predicted ray paths for test cases 1 and 2 are shown in Figures 5.3 and 5.4, respectively, for the November SSP which is also shown at the left in the figure.

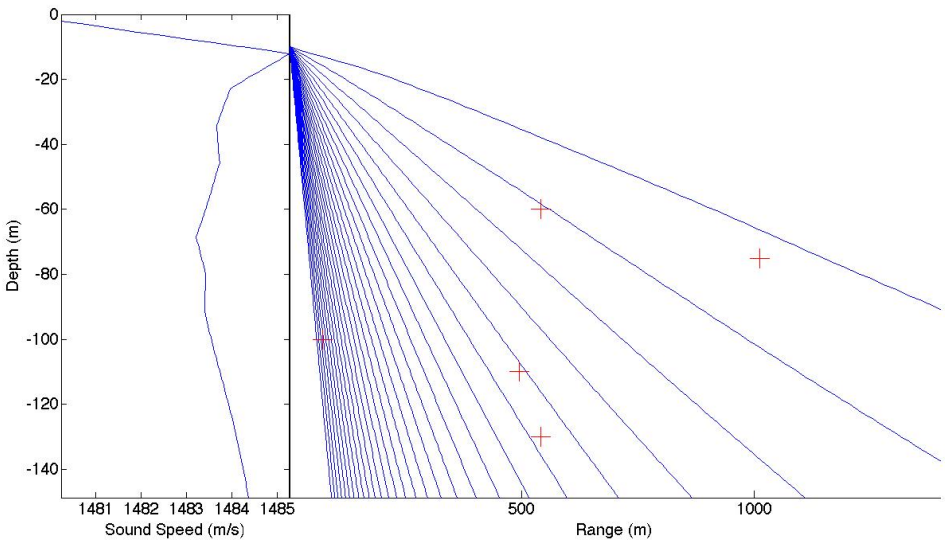

Figure 5.3: SSP and predicted ray paths for test case 1, with take-off angles from 0–60° in 2° increments. Hydrophone positions are depicted as '+' .

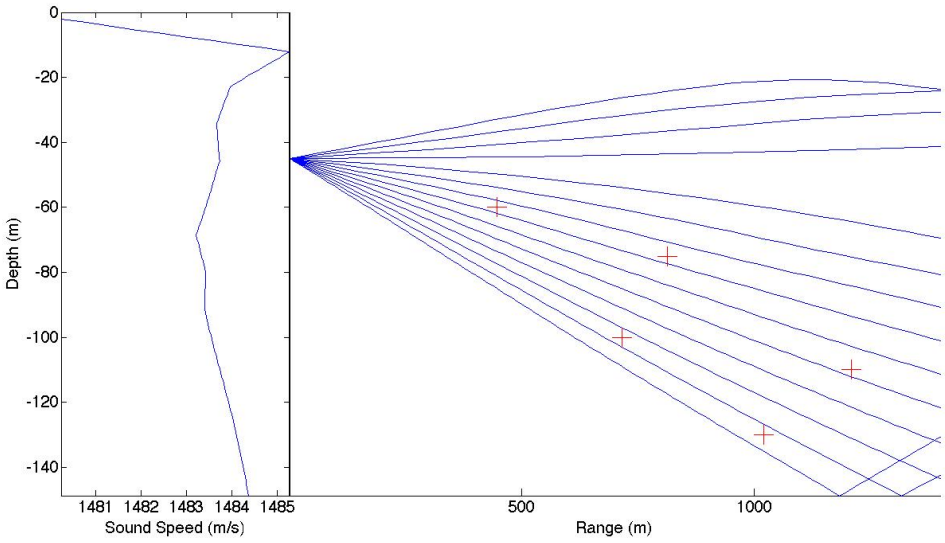

Figure 5.4: SSP and predicted ray paths for test case 2, with takeoff angles from -2° to +5° in 0.5° increments. Hydrophone positions are depicted as '+'s.

Under certain conditions, eigenrays do not exist to connect a source-receiver pair, and one example of this situation is shown in Fig. 5.5. In this case, the source is located in the northwest quadrant of the range at a depth that corresponds to an inflection point in the SSP, a local sound-speed maximum, causing rays to diverge from that depth. The hydrophone at 60-m depth is located in a shadow zone with respect to this source location, and no direct-path ray connects these two points. When such a position is chosen randomly in test case 3, it can destabilize the inversion and an acceptable solution may not be found. In this case the result is excluded from the Monte Carlo simulation; however, this may represent a significant problem that could be encountered in practical operations. Multipath rays could provide additional information in this situation, however

these rays were not considered due to complications involved in predicting reflected ray paths over a sloping bottom.

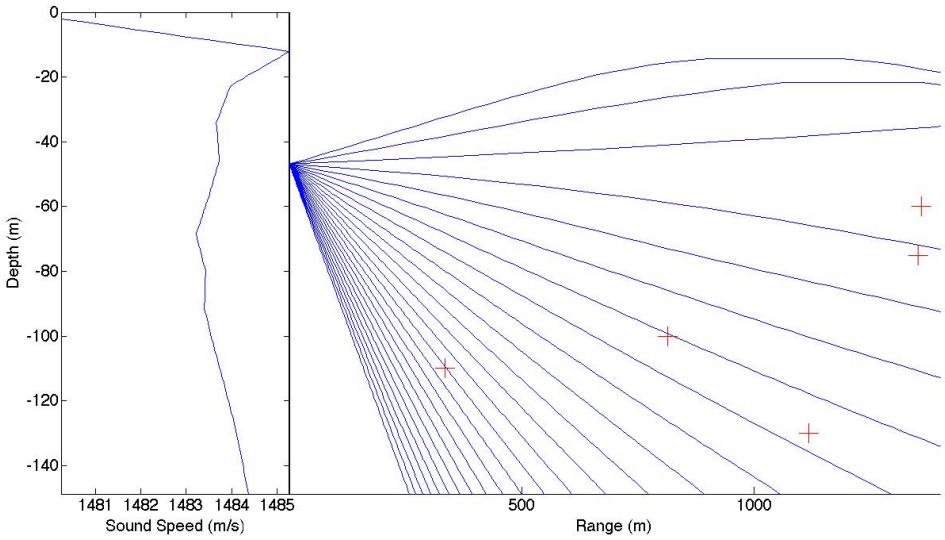

Figure 5.5: SSP and predicted ray paths for a source in test case 3, where the source position is chosen randomly, for take-off angles from -4° to +21° in 1° increments. Hydrophone positions are depicted as '+'s.

Note that the SSP used here is based on measurements made on one particular day of the year, and this profile and the resultant ray paths will not apply when conditions vary. Referring to Fig. 1.3, it is clear that the sound speed is subject to much variation over the course of a year, in addition to the local variations to be investigated in Section 5.5. To study the impact of this long-period variation in the SSP, the simulations described in Sections 5.2–5.5 are carried out with each of the three profiles identified above (September, November and December), with results discussed where they are worth noting, (figures in those sections show results using one profile only).

5.1.4 Simulation procedure

As described in Chapter 2, the inversion algorithm is a linearized solution to a nonlinear system of equations, and hence linearization error may affect the solution and the uncertainties contained in the posterior model covariance matrix. To investigate this issue and to study the four factors mentioned earlier (ray curvature, SSP bias, hydrophone position errors, and lateral SSP variability), Monte Carlo analysis is performed. In each simulation, arrival times (known here as the true data) are computed using the ray-tracing model. A large number of (simulated) observed data sets (typically 1000) are then drawn by adding random noise to the arrival time differences for each scenario, and each TDOA data set is inverted. The model errors are taken to be the difference between true and estimated parameter values. These errors are presented in histograms throughout the rest of this chapter and summarizing statistics are computed and tabulated.

The tables presented to summarize source position error statistics include three measures for each scenario and test case: bias, μ, standard deviation, σ, and root mean square error (RMSE). These measures are calculated for a model parameter m_i over n Monte Carlo realizations as:

$$\mu_i = \frac{\sum_{j=1}^{n}\left(m_{ij} - m_{true,i}\right)}{n}, \tag{5.1}$$

$$\sigma_i = \sqrt{\frac{\sum_{j=1}^{n}\left(m_{ij} - \mu_i\right)^2}{n}}, \tag{5.2}$$

$$RMSE_i = \sqrt{\frac{\sum_{j=1}^{n}\left(m_{ij} - m_{true,i}\right)^2}{n}}. \tag{5.3}$$

Combining Eqs. (5.1)–(5.3), it can be shown that RMSE $= \sqrt{\mu^2 + \sigma^2}$. RMSE is a good indicator of overall accuracy, as it measures the spread of the parameter estimates from the true value, but alone does not indicate whether the spread is due to a systematic error (bias), or a wide error distribution (standard deviation). This distinction is important in this application, and so all three values are reported for each simulation.

To compare the numerical (Monto Carlo) results to the analytic uncertainty (linearized approximation), the posterior uncertainties for a source position in *x, y,* and *z*, are calculated using the square root of the diagonal entries in the model covariance matrix. From these uncertainties, the error distribution for model parameter m_i is calculated as

$$P(m_i) = \frac{1}{\sqrt{2\pi}C_{m_{ii}}} \exp\left[-\frac{\left(m_i - m_{true,i}\right)^2}{2C_{m_{ii}}}\right]. \tag{5.4}$$

These linearized uncertainty distributions are compared with the respective Monte Carlo histograms (representing nonlinear error analysis) for each scenario and each of the three test cases.

5.2 Refraction Effects

Many acoustic positioning techniques do not employ a ray-tracing model, but assume straight-line propagation through a constant sound-speed water column. This section investigates the effect on localization uncertainty at the IAS range of neglecting/including refraction effects.

Path length, and consequently travel time, predicted through ray tracing depends on the SSP used in the model. Specifically, the ray curvature is determined by the gradient of sound speed: rays curve upwards for a positive gradient (sound speed increases with

depth) or downwards for a negative gradient. A larger sound-speed gradient results in greater bending of rays and, hence, greater path lengths. The September SSP shown in Fig. 5.2 has a strong downward refracting gradient, and is used here to investigate refraction effects on localization.

To assess the effect of modelling using a constant sound-speed approximation to the SSP on localization errors, each of the 5000 noisy data sets generated for this scenario was inverted using both a straight-line and a curving-ray model. SSP bias was included as an unknown parameter in the inversion, with large prior uncertainty (10 m/s) to allow the straight-ray inversion the ability to determine the best possible (constant) sound speed to represent the profile. Histograms comparing the inversion results for both propagation models are presented in this section for each of the three test cases in Figs. 5.6 – 5.8. The biases, standard deviations, and RMS errors for each case are given in Table 5.2.

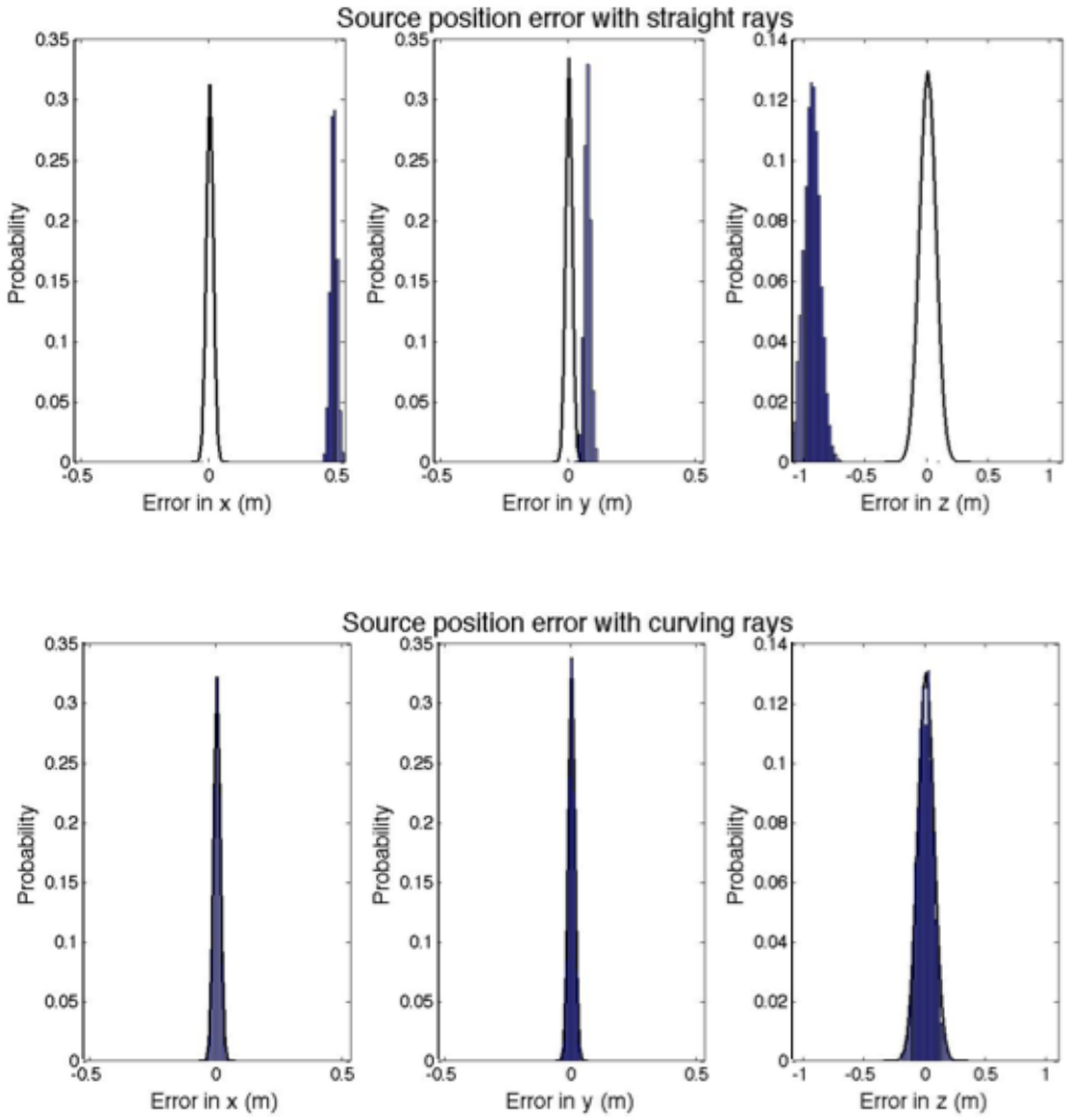

Figure 5.6: Histogram of errors for *x, y*, and *z* source locations for test case 1 using inversion based on straight rays (top) and curving rays (bottom) for 5000 noisy data sets. Continuous distribution represents linearized uncertainty distribution.

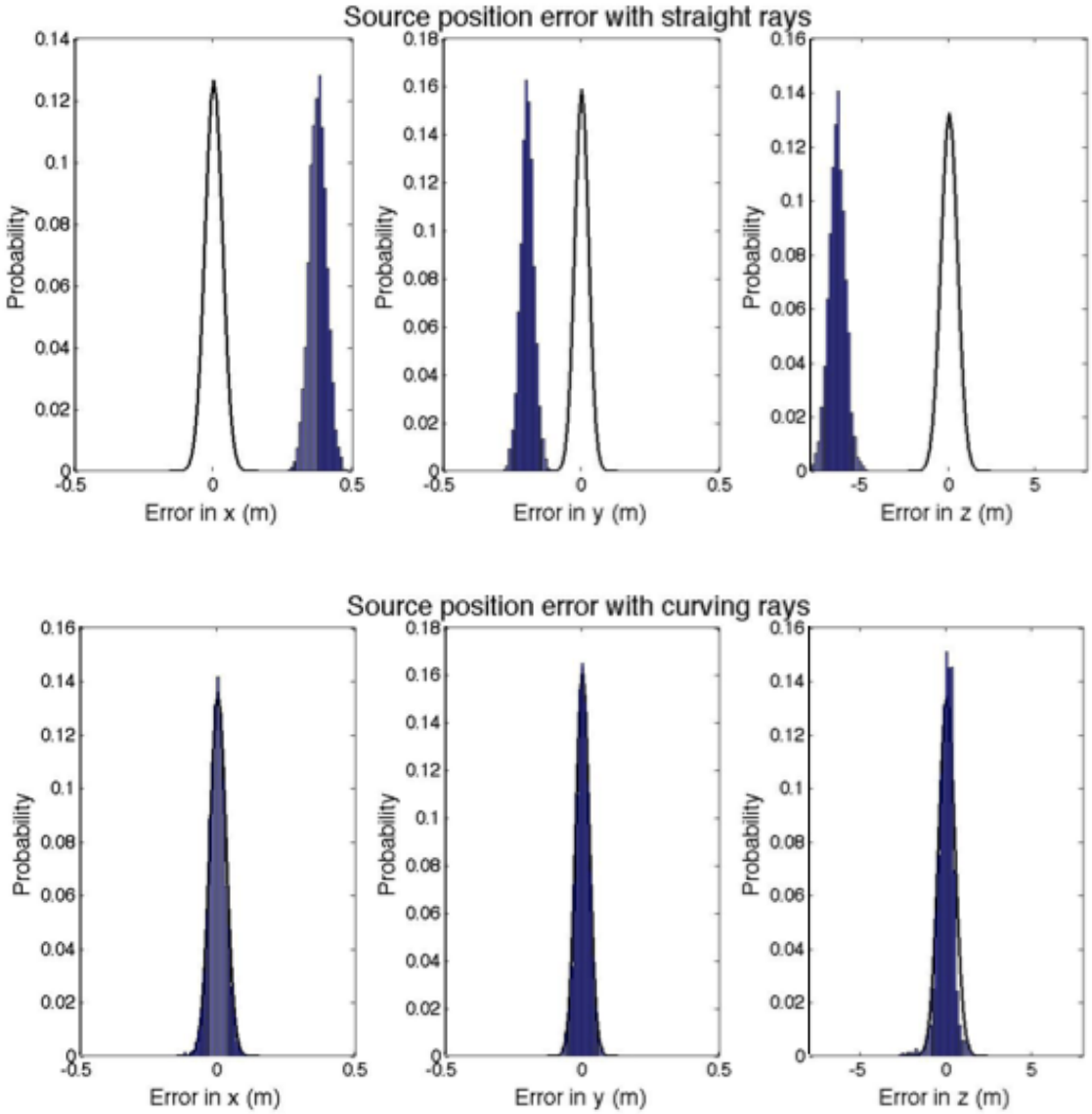

Figure 5.7: Histogram of errors for *x, y*, and *z* source locations for test case 2 using inversion based on straight rays (top) and curving rays (bottom) for 5000 noisy data sets. Continuous distribution represents linearized uncertainty distribution.

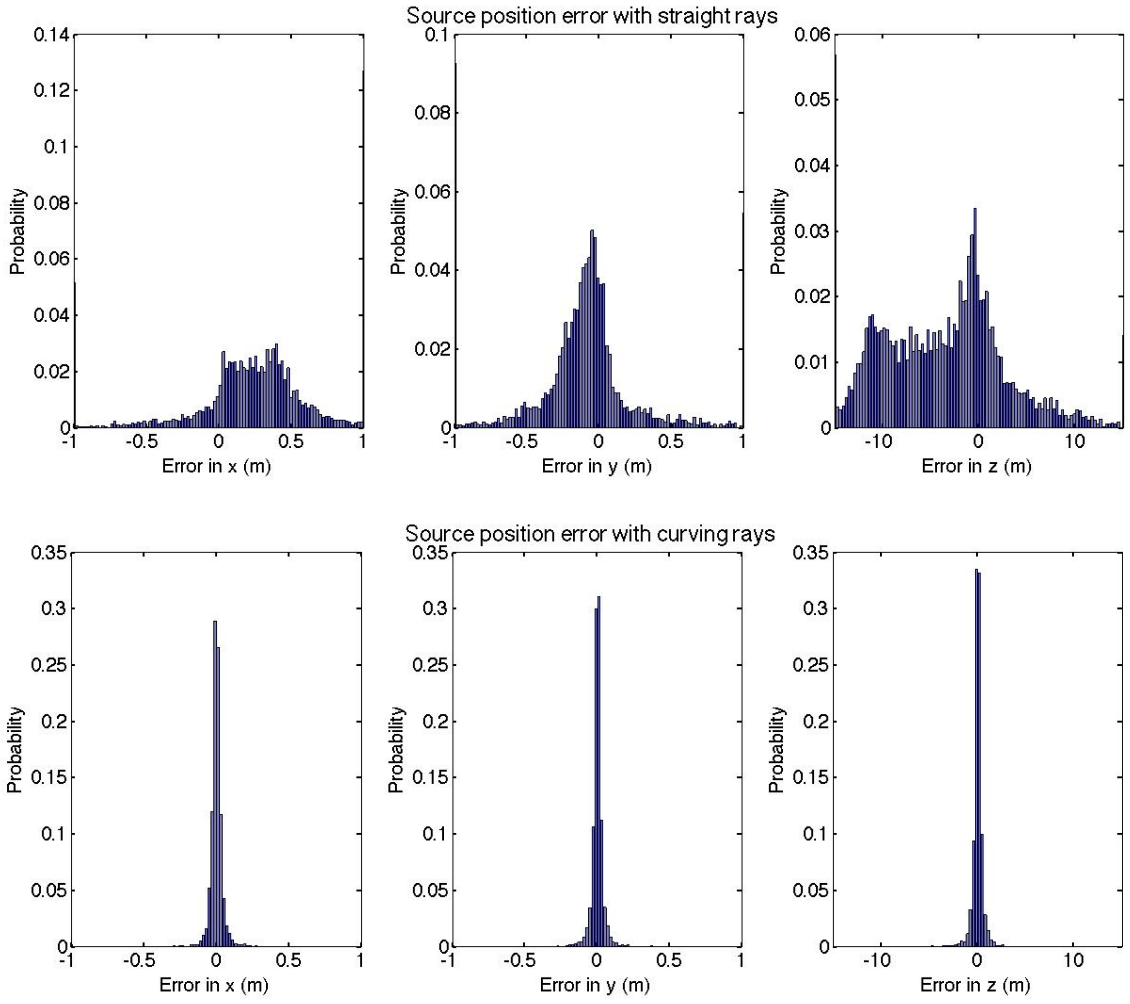

Figure 5.8: Histogram of errors for *x, y*, and *z* source locations for test case 3 using inversion based on straight rays (top) and curving rays (bottom) for 5000 noisy data sets.

Figure 5.6 shows the errors on *x, y,* and *z* source position for test case 1 (favourable source position) using both straight and curving ray propagation models. Considering this figure and Table 5.2, bias is the dominant component of the RMS error for the straight-ray inversions, implying that neglecting ray tracing biases the non-linear inversion result away from the true model, with a relatively narrow distribution of results (histogram) about a biased value. The bias for *x, y,* and *z* is, respectively, 47, 7, and -94 cm. This

implies that there is a systematic error imposed on the inversion results when using the constant sound-speed approximation for propagation modelling. However, the inversion results using the ray-tracing model appear unbiased (biases of less than 1 cm in each *x, y,* and *z* for 5000 samples), with small standard deviations of 1, 1, and 7 cm in *x, y,* and *z.*

Test case		Straight-ray model			Curving-ray model		
		x	y	z	x	y	z
1	Bias (m)	0.47	0.072	-0.94	-0.0059	-0.00046	-0.0037
	σ (m)	0.013	0.012	0.067	0.013	0.012	0.066
	RMS (m)	0.48	0.073	0.94	0.013	0.012	0.066
2	Bias (m)	0.37	-0.2	-6.5	0.00099	0.00032	-0.048
	σ (m)	0.031	0.025	0.48	0.03	0.025	0.47
	RMS (m)	0.38	0.2	6.5	0.03	0.025	0.47
3	Bias (m)	0.19	-0.23	-3.9	-0.0032	-0.011	-0.095
	σ (m)	2.1	1.6	7.3	0.045	0.030	0.66
	RMS (m)	2.2	1.6	8.3	0.046	0.031	0.69

Table 5.2: Bias, standard deviation (σ), and RMS error in *x, y,* and *z* source positions for each of the three test cases using inversion based on straight rays and curving rays.

The linearized uncertainty distributions are in excellent agreement with the numerical uncertainty distributions (histograms) using the curving-ray model for test case 1, indicating that linearization error is not significant in this case, and that the analytic uncertainties calculated from the model covariance matrix are a good estimate of the nonlinear result. For the straight-ray model, however, the linearized and numerical uncertainty distributions do not agree, because the model covariance matrix does not

account for the data error biases resulting from modelling propagation with the straight-ray model.

Figure 5.7 shows the *x, y,* and *z* source position errors for test case 2 (poor source location). In this case again there is good agreement between the linearized uncertainty estimate and nonlinear Monte Carlo results for curving rays. From Table 5.2, the straight-ray model produces slightly smaller RMS errors than test case 1 in *x* (38 cm), but slightly larger in *y* (20 cm) and much larger in *z* (6.5 m), indicating that the source position can significantly affect source-position uncertainty. These errors are again primarily due to the bias resulting from the straight-ray model. The test case 2 position provides reasonably good information for resolving source positions in *x* and *y*, both for straight and curving ray models; however, the information for resolving *z* is poor, as *z* errors increase dramatically between test case 1 and test case 2. This explanation is expanded upon below.

For simulations of test case 3 (random source positions), shown in Fig. 5.8, errors in the straight-ray model are again biased; however, in this case the bias is not the lone contributor to RMS error, as the errors are distributed broadly with large standard deviations, seen in Table 5.2. Here, it is noted, the scales of the straight and curving-ray histograms differ, to allow the error distributions to be viewed properly. For any given source position within the test range, there is an associated mean bias, evident from the simulations in test cases 1 and 2. Since test case 3 is a collection of random positions, the net effect of a collection of error biases (which may be positive or negative) is to reduce the overall bias. Also, as test case 3 involves many different source locations, the analytic (linearized) uncertainty distribution does not apply and is not included in Fig. 5.8.

Fermat's principle states that the path taken by a ray is that which can be travelled in the shortest time, and for the constant sound-speed approximation the shortest path between two points is a straight line. Curving rays are able to spend more travel time in a faster medium, and subsequently their travel time between the same two points is less, despite travelling a longer path. This is true for upward- or downward-refracting profiles; however, including the SSP bias as an inversion parameter allows the straight-ray inversion to adjust constant sound speed to partially account for the travel-time difference. By decreasing the SSP bias prior uncertainty (in effect limiting the amount that either inversion is able to adjust this parameter), source-position uncertainties are largely unaffected in the curving-ray inversion; however, errors increase for the straight-ray inversions: considering the test case 2 position, constraining the sound-speed bias parameter to a prior uncertainty 0.01 m/s results in RMS errors of 70 cm in x and y and 8 m in z (not shown) as compared to 39 and 20 cm in x and y and 6.5 m in z when a 10 m/s prior uncertainty is used (Table 5.2).

Since the straight-ray model predicts longer travel times than the curving ray model, despite the corrective ability of the SSP bias parameter, the source position is generally shifted away from hydrophones. This is evident in Fig. 5.6 for the test case 2 source position, where there is no hydrophone located to the south or east of the source. Accordingly, the errors on the straight-ray predicted source position for test case 2 are biased to the south and east, or the positive x and negative y directions.

In the z direction, all hydrophones are located at greater depths than the source, so source location along this axis is more poorly constrained: this is why the largest errors are seen in z. In IAS operations, improved localization accuracy in z could be obtained by

equipping the target with a pressure sensing device to provide independent information about z, by adding a top-side hydrophone, or by including multi-path arrivals.

The curving-ray results presented here can be considered a 'best-case' baseline for comparing inversions in later sections, where noisy data is applied to the algorithm and results will naturally deteriorate.

In summary, this section has shown that source position errors due to neglecting ray curvature can be considerable. Errors are dependent on source location, with sources at the periphery of the range subject to the greatest position errors. The straight-ray model is able to partially account for errors through adjustment of the SSP bias; however, this parameter does not negate the requirement for accurate modelling of transmission paths when attempting to achieve a high degree of accuracy in an acoustic positioning system.

5.3 Sound Speed Bias

Sound-speed profile measurements, while generally considered precise in a relative sense, can contain an unknown sound-speed bias, (a constant offset at all depths) due to calibration issues of up to 2 m/s for CTD instruments (Vincent & Hu, 1998) and 0.34 m/s for velocimeters (Sweeney *et al.*, 2006). Here, a maximum bias of 2 m/s corresponds roughly to a standard deviation on 1 m/s (as 95% of samples , on average, will fall within -2 m/s < c_b < 2 m/s), and such a bias is applied to the simulated environment in two different ways: (1) carrying out 1000 inversions of noisy data in which each inversion the SSP is biased (compared to the SSP used to compute the true data) by a random draw from a Gaussian distribution of mean zero and standard deviation 1 m/s. This case emulates the prior information used in the standard inversion formulation, but does not allow a meaningful assessment of localization bias due to SSP bias as bias effects are

essentially averaged out, and (2) carrying out 1000 inversions of noisy data in which the SSP in each inversion is biased by +1 m/s. This case allows localization bias to be investigated. These scenarios were chosen to represent two real-world cases: (1) the consequence of sampling the water column with any random CTD instrument subject to the errors described above, and (2) the consequence of repeatedly using the same miscalibrated instrument. Inversions are carried out which treat the SSP as exactly known, referred to here as the uncorrected inversion, or which invert for the bias as an unknown parameter (the corrected inversion), and the results of each are compared in this section for all three test cases. Results for scenario (1) are shown in Figs. 5.9 – 5.11 and Table 5.3, and results for scenario (2) are shown in Figs. 5.12 – 5.14 and Table 5.4. Hydrophone positions are considered to be exactly known in this section.

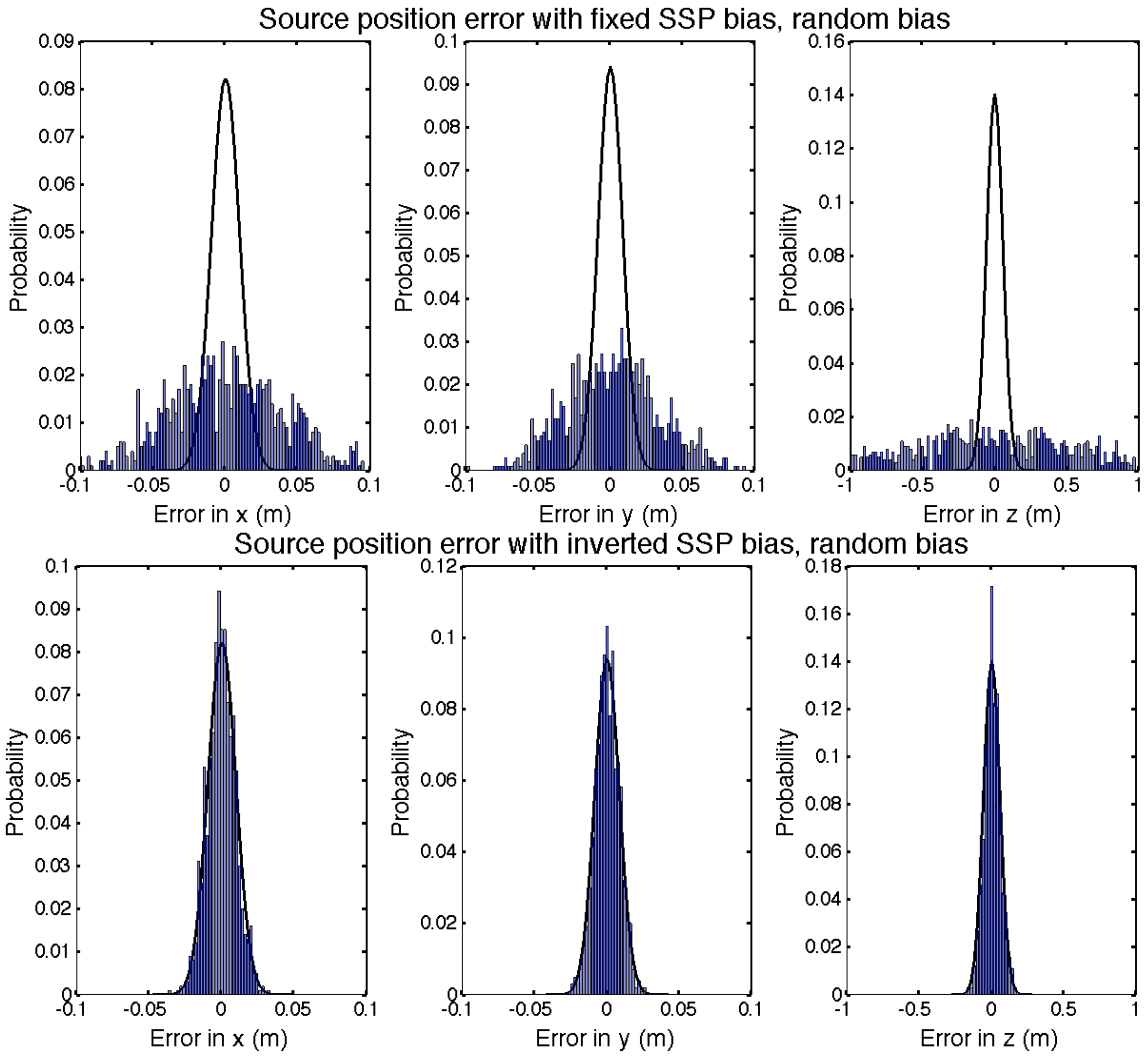

Figure 5.9: Histogram of errors for *x, y*, and *z* source position obtained when SSP bias is included (bottom) and is not included (top) as an inversion parameter for test case 1 based on inversion of 1000 noisy data sets with a random sound speed bias applied. Continuous distribution represents linearized uncertainty distribution.

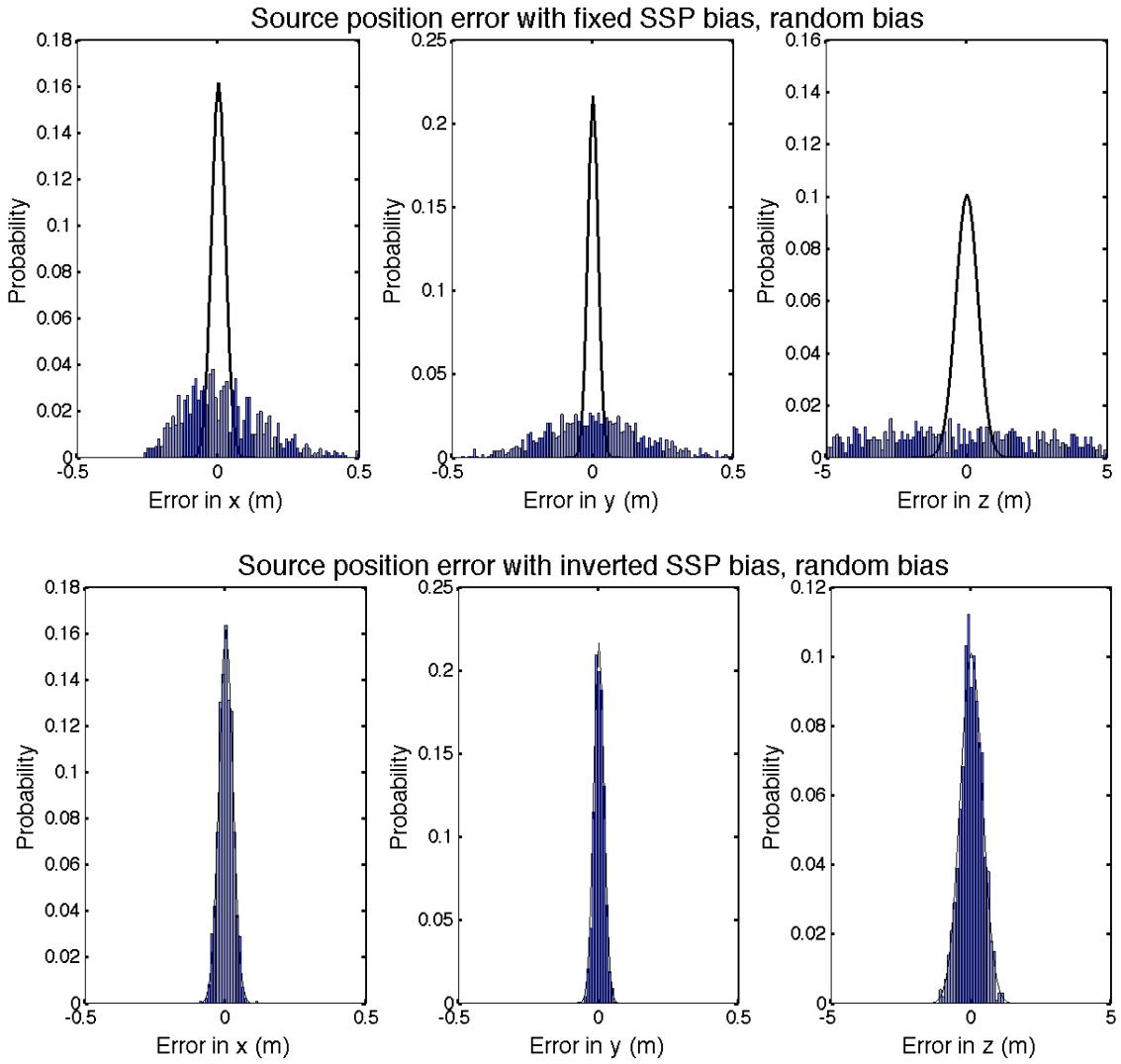

Figure 5.10: Histogram of errors for *x, y*, and *z* source position obtained when SSP bias is included (bottom) and is not included (top) as an inversion parameter for test case 2 based on inversion of 1000 noisy data sets with a random sound speed bias applied. Continuous distribution represents linearized uncertainty distribution.

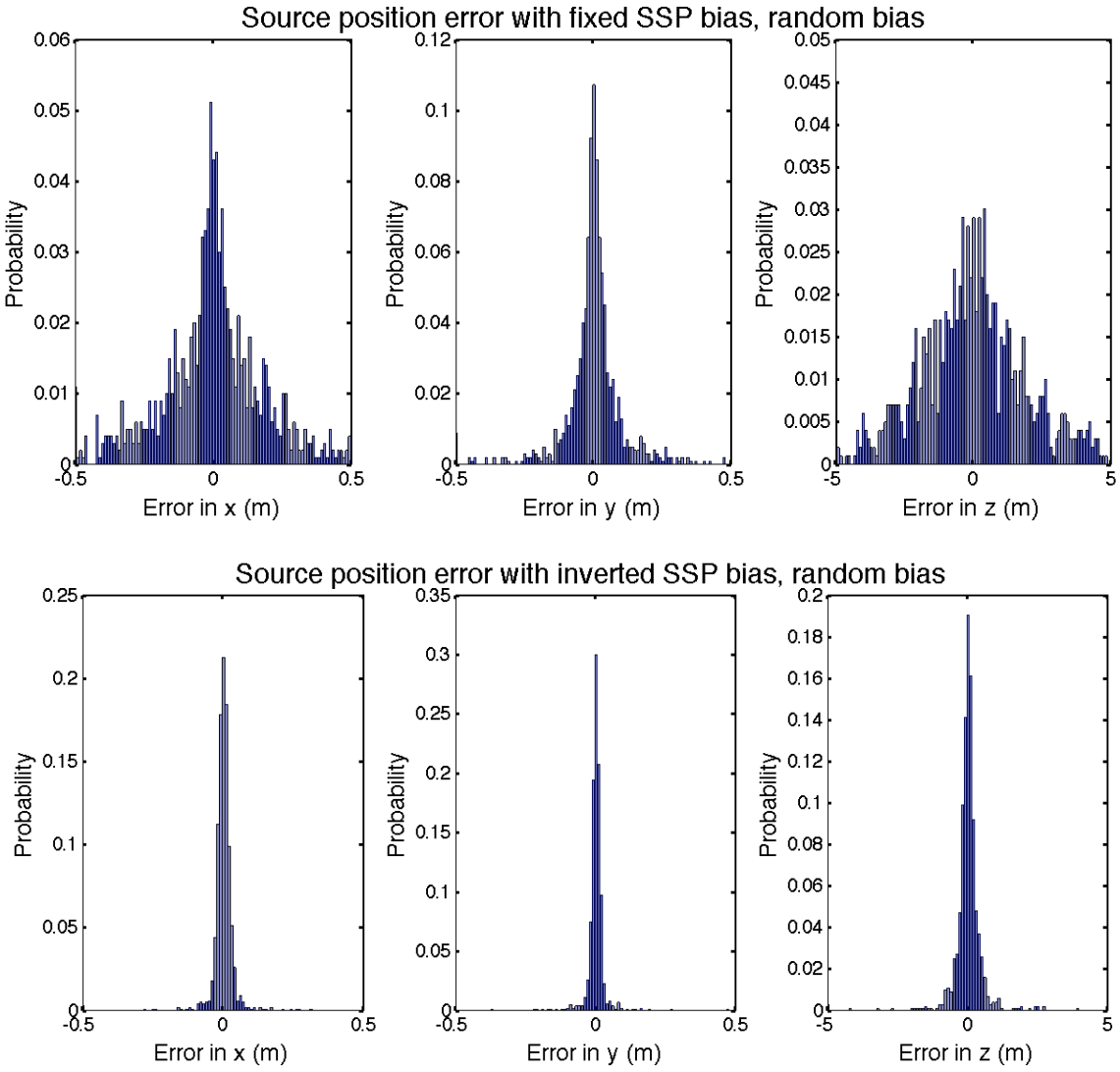

Figure 5.11: Histogram of errors for *x, y*, and *z* source position obtained when SSP bias is included (bottom) and is not included (top) as an inversion parameter for test case 3 based on inversion of 1000 noisy data sets with a random sound speed bias applied

The effect of SSP bias can be substantial, as seen in Figs. 5.9–5.14. The inversion algorithm is generally good at estimating the SSP bias, as the inversions that account for SSP bias show an overall large improvement over those which do not account for bias. Statistical results for inversions with a SSP bias, when it is applied as a zero-mean

Gaussian random variable with standard deviation 1 m/s, as described for scenario (1), are given in Table 5.3, and when it is applied as a constant 1 m/s offset, as described in scenario (2), are given in Table 5.4. The average bias, standard deviation (σ), and RMS error are calculated for *x, y,* and *z* source positions for each of the three test cases when inverting for the SSP bias, and when holding the SSP bias fixed at zero for the inversion.

Test case		Fixed SSP bias			Inverted SSP bias		
		x	y	z	x	y	z
1	Bias (m)	0.0011	0.0012	-0.016	-3.7e-04	-1.3e-04	0.0031
	σ (m)	0.0038	0.032	0.63	0.0096	0.0089	0.054
	RMS (m)	0.0038	0.032	0.64	0.0096	0.0089	0.054
2	Bias (m)	0.021	0.0038	0.44	-3.6e-05	-5.7e-05	-2.7e-04
	σ (m)	0.14	0.17	4.24	0.025	0.018	0.37
	RMS (m)	0.14	0.17	4.38	0.025	0.018	0.37
3	Bias (m)	-0.15	-0.031	2.1	-0.0029	0.0064	-0.046
	σ (m)	0.30	0.27	3.4	0.055	0.041	0.64
	RMS (m)	0.30	0.27	3.5	0.056	0.042	0.65

Table 5.3: Bias, standard deviation (σ), and RMS error for *x, y*, and *z* source position for each of the three test cases when including the sound-speed bias in the inversion and when holding the sound speed fixed in the inversion, for the case of a zero-mean, Gaussian distributed random error with standard deviation 1 m/s added to the SSP.

Figures 5.9–5.11 show the Monte Carlo results when the SSP bias is applied as a random variable (scenario 1). For test case 1 (Fig. 5.9 and Table 5.3), errors are distributed about a mean of close to zero for *x*, *y*, and *z* for both corrected and uncorrected inversions. In both cases, the major contributor to RMS error is the standard deviation,

indicating that over many inversions, the individual errors tend to cancel. Errors in standard deviation are 3.1, 3.8 and 68 cm in *x*, *y*, and *z*, respectively, when SSP bias is held fixed, and 0.9, 0.8, and 3.2 cm when inverting for SSP bias. Agreement between the linear uncertainties predicted in the model covariance matrix and the nonlinear Monte Carlo results is very good for the corrected inversion in Fig 5.9, indicating that linearization errors are small. This is not the case for the uncorrected case, where there is poor agreement between the linear uncertainties and Monte Carlo results due to the SSP bias error which is not accounted for.

Similarly for test cases 2 and 3 (Figs. 5.10 and 5.11), the source position errors resulting from random SSP biases are not significantly biased, but errors are distributed over a much wider range when SSP bias is not included as an inversion parameter. As compared to the uncorrected inversion RMS errors on the corrected inversion are very small in *x*, *y*, and *z*; however, the absolute error in *z*, at 35 cm for test case 2 and 64 cm for test case 3, is considerable, due to the unfavourable geometric configuration of receivers in *z*. As with test case 1, test case 2 shows good agreement between linear uncertainty estimates and nonlinear Monte Carlo results. Linear uncertainty estimates are not shown for test case 3 (Fig. 5.11) as this test involves randomly selected source locations and hence there is no corresponding analytic solution.

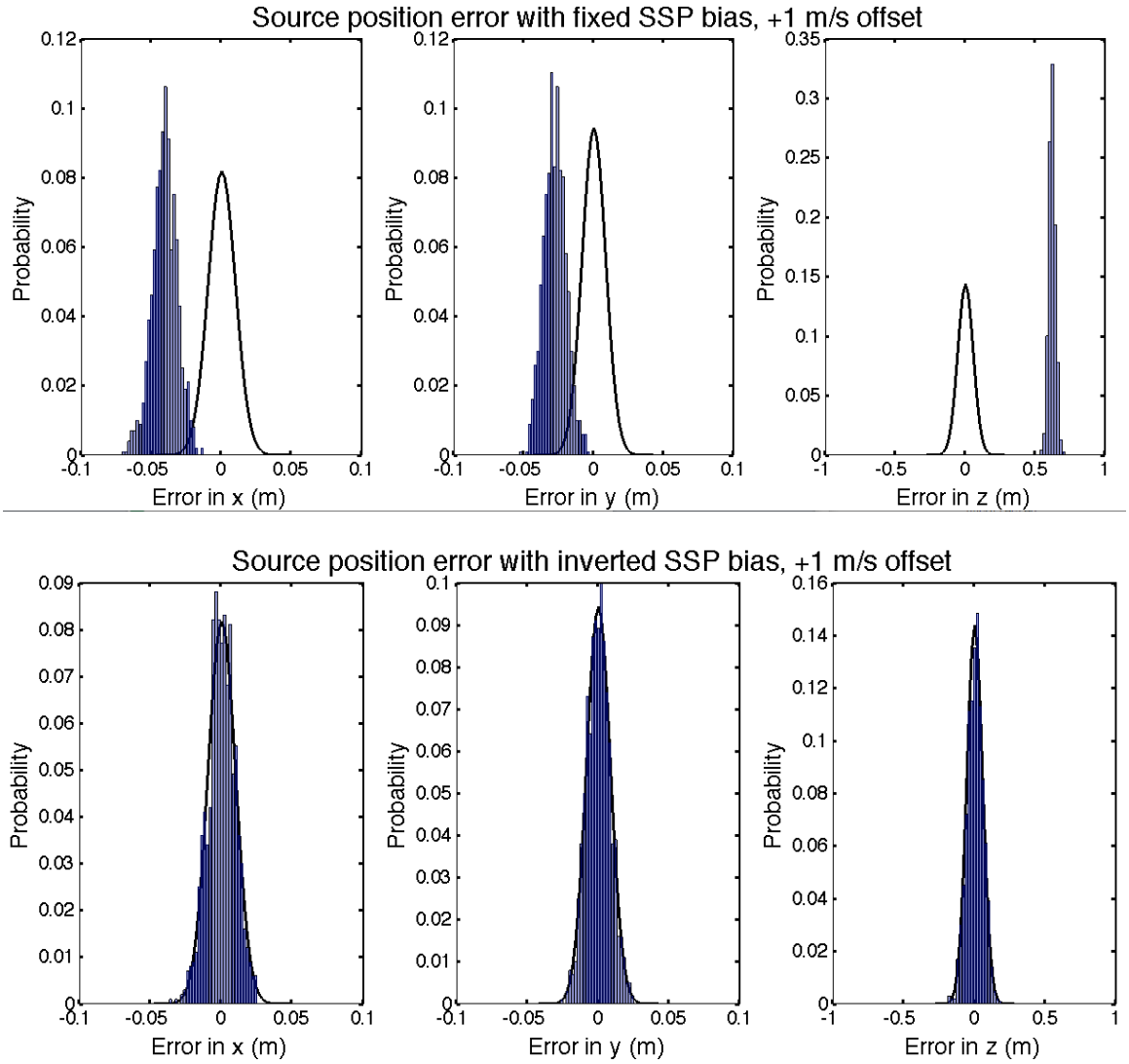

Figure 5.12: Histogram of errors for *x, y*, and *z* source position obtained when SSP bias is included (bottom) and is not included (top) as an inversion parameter for test case 1 based on inversion of 1000 noisy data sets. Continuous distribution represents linearized uncertainty distribution.

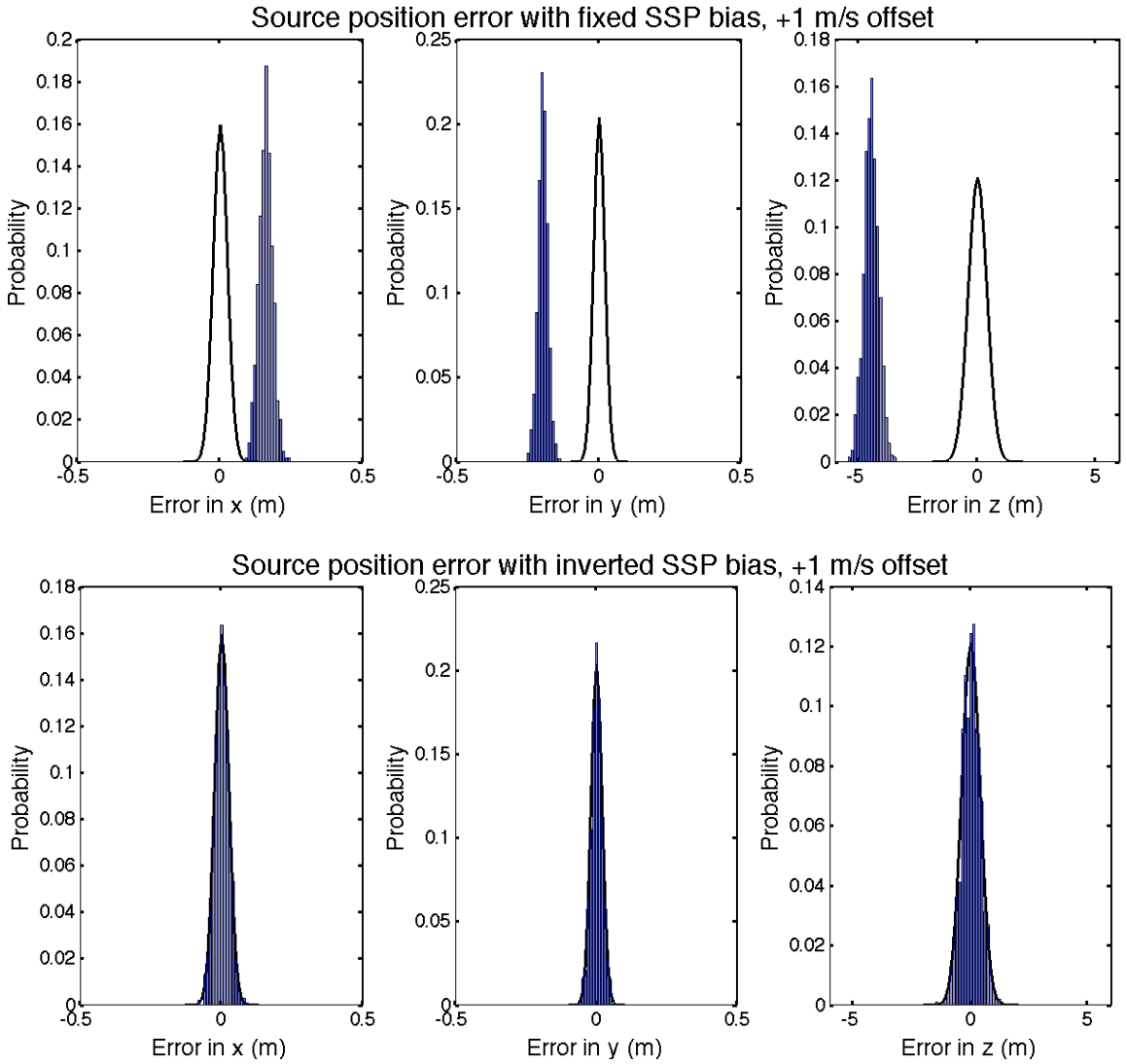

Figure 5.13: Histogram of errors for *x, y*, and *z* source position obtained when SSP bias is included (bottom) and is not included (top) as an inversion parameter for test case 3 based on inversion of 1000 noisy data sets. Continuous distribution represents linearized uncertainty distribution.

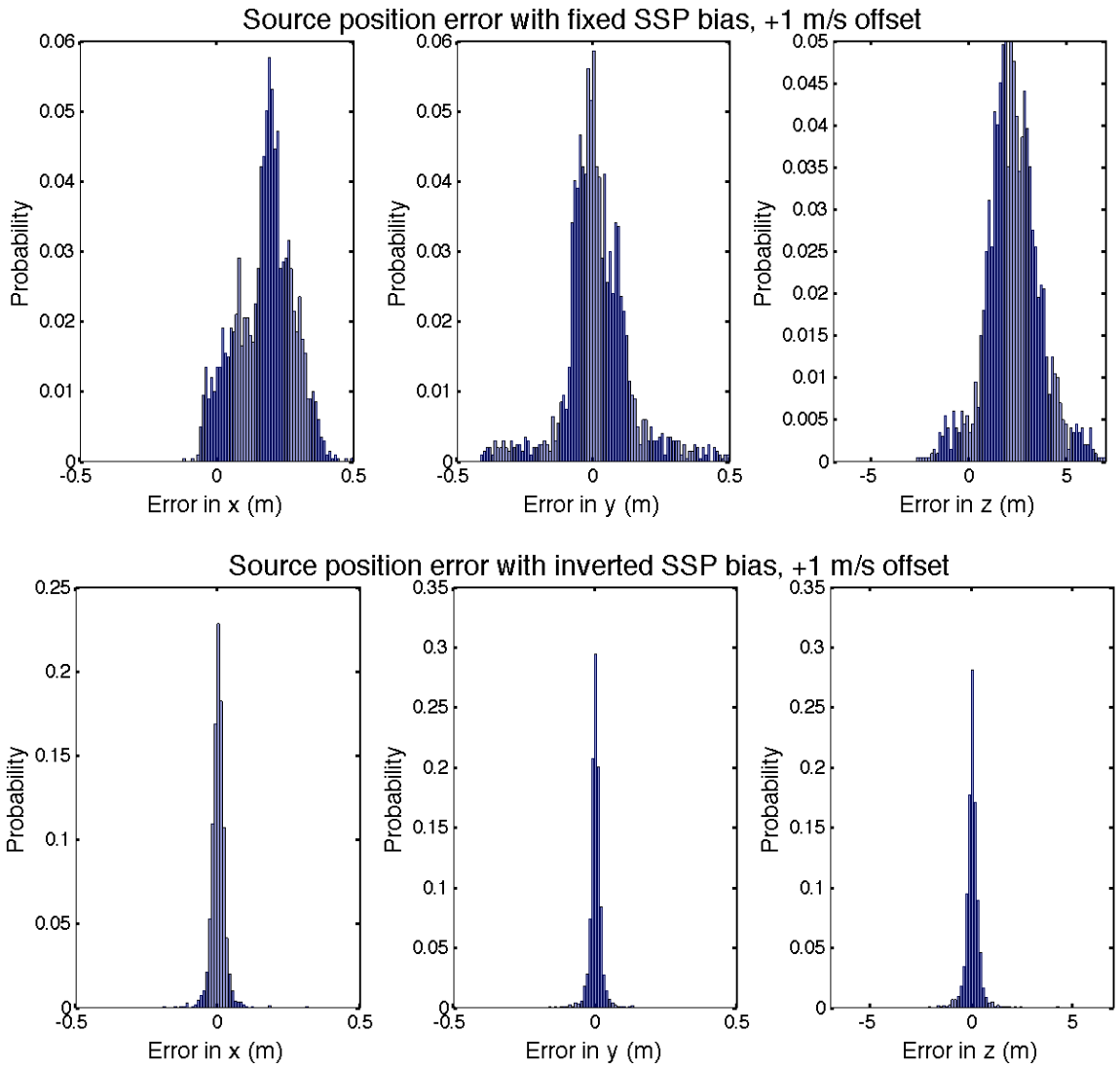

Figure 5.14: Histogram of errors for *x, y*, and *z* source position obtained when SSP bias is included (bottom) and is not included (top) as an inversion parameter for test case 3 based on inversion of 1000 noisy data sets.

When the SSP bias is applied as a 1 m/s offset, as in scenario (2), shown in Figs. 5.12–5.14, the bias is the dominant component of the RMS error for the uncorrected inversion, as source-position errors in *x* and *y* are distributed over a narrow range, offset from the true value. For the corrected inversion, standard deviation remains the dominant

component of RMS error, since results appear to be unbiased. A summary of the results obtained for scenario (2) is shown in Table 5.4. Linear uncertainty estimates for the corrected inversion are in excellent agreement with Monte Carlo results. For the uncorrected inversion the distribution of errors from Monte Carlo analysis is similar to the linearized estimate, but with a distinct bias in *x*, *y*, and *z*. This implies that the SSP bias produces a systematic source-position error over a large number of samples. The standard deviation on errors in *z* is larger, implying that the *z* component is less constrained by the data regardless of whether the SSP bias is accounted for.

Test case		Fixed SSP bias			Inverted SSP bias		
		x	y	z	x	y	z
1	Bias (m)	-0.041	-0.027	0.62	-3.1e-05	-8.8e-05	0.003
	σ (m)	0.0089	0.0079	0.024	0.0095	0.0082	0.056
	RMSE (m)	0.042	0.029	0.62	0.0093	0.0082	0.056
2	Bias (m)	0.15	-0.17	-4.5	2.5e-05	1.8e-05	-0.0098
	σ (m)	0.024	0.018	0.31	0.025	0.0179	0.39
	RMSE (m)	0.16	0.18	4.5	0.025	0.0179	0.39
3	Bias (m)	0.17	0.015	2.2	2.1e-04	-2.8e-04	0.017
	σ (m)	0.19	0.13	1.4	0.062	0.049	0.61
	RMSE (m)	0.19	0.13	2.6	0.062	0.049	0.61

Table 5.4: Bias, standard deviation (σ), and RMS error for *x, y*, and *z* source position for each of the three test cases when including the sound-speed bias in the inversion and when holding the sound speed fixed in the inversion, for the case of a 1 m/s offset added to the SSP.

If the SSP bias, as applied in scenario (2), is increased above 1 m/s (not shown), source-position errors are affected for both uncorrected and corrected inversions. Increasing the SSP bias does not largely affect *x* and *y* errors for the corrected inversion, as the algorithm is proficient at converging towards an appropriate value for SSP bias and the lateral position errors are accounted for; however, *z* errors tend to increase as the bias increases. Errors on the uncorrected inversion increase with increasing SSP bias in *x, y,* and *z*. If no SSP bias is applied ($\mu = 0$, $\sigma = 0$), the corrected and uncorrected inversions produce statistically similar results, both with errors of approximately 1 cm in *x* and *y*, and 20 cm in *z*, indicating that there may be a geometrical limitation to how well the algorithm is able to resolve the target position in *z*.

A greater number of source transmissions provides more information for refining the sound-speed bias estimate in the corrected inversion, which in turn has a direct impact on the source-position error. A single-source inversion (as shown) is able to improve the 1-m/s mean SSP bias estimate to within an RMS error of 20 cm/s of the true value. However, an inversion based on 10 sources (not shown) is able to improve the SSP bias estimate to within 0.5 cm/s of the true value. Improved knowledge of the bias leads to slightly improved source-position estimates, as the single source inversion achieves a 61 cm error in *z* for test case 3 (Table 5.4), as compared to 22 cm for *z* in the 10-source inversion with comparable improvements in *x* and *y*.

The SSP bias effect depends strongly on the source location with respect to receivers. For a source located between two hydrophones, the SSP bias creates an offsetting error (e.g. arrival times are too large at one hydrophone, too small at the other) and the net effect on source-position error is diminished. Hence, a source located centrally in the

range, such as in test case 1 (Fig. 5.11), incurs less source-position error than one located towards the perimeter of the range, as in test case 2 (Fig. 5.12). Peripheral source locations are particularly poor for resolving *z*, evident through comparison of test cases 2 and 3 in Table 5.4, where random locations perform worse in *x* and *y*, but better in *z*.

Sound-speed profile characteristics affect source-position errors due to SSP bias. The figures in Section 5.3 are all compiled using the downward-refracting September SSP; however, when the upward-refracting December SSP is used, *x* and *y* position errors decrease, but *z* errors increase both when inverting for SSP bias and when holding it fixed. Using the November profile produces results that fall in between the September and December profiles.

In summary, the effect of a SSP bias is considerable, whether it is treated as a random error or a constant offset. The source position error imposed by the bias is dependent on source position, and can be particularly detrimental to accuracy in *z*. Accounting for this bias can provide a substantial improvement to source-positioning accuracy, and should be considered for the IAS positioning system.

5.4 Uncertainty in Hydrophone Position

Hydrophone positions are fixed (i.e., unmovable); however, our knowledge of these positions inevitably contains some level of uncertainty. To explore the effect of accounting for this uncertainty by inverting for hydrophone positions as parameters in the model rather than holding hydrophones fixed at incorrect locations, a scenario was developed to simulate inversion using inexact knowledge of hydrophone positions. Five thousand sets of prior estimates of hydrophone positions were created, each with a Gaussian-distributed, zero-mean error of standard deviation 0.5 m added to the true

position of each hydrophone in *x, y* and *z*. True arrival-time data were calculated for 10 source transmissions, with noise added to simulate timing error for each prior estimate, and inverted in two ways: (1) inverting for the hydrophone locations as model parameters and (2) holding the hydrophone locations fixed at the (erroneous) prior values. The simulation was run for each of the three test case source positions, and the results are presented in Figs. 5.15–5.17 and summarized in Table 5.5

.

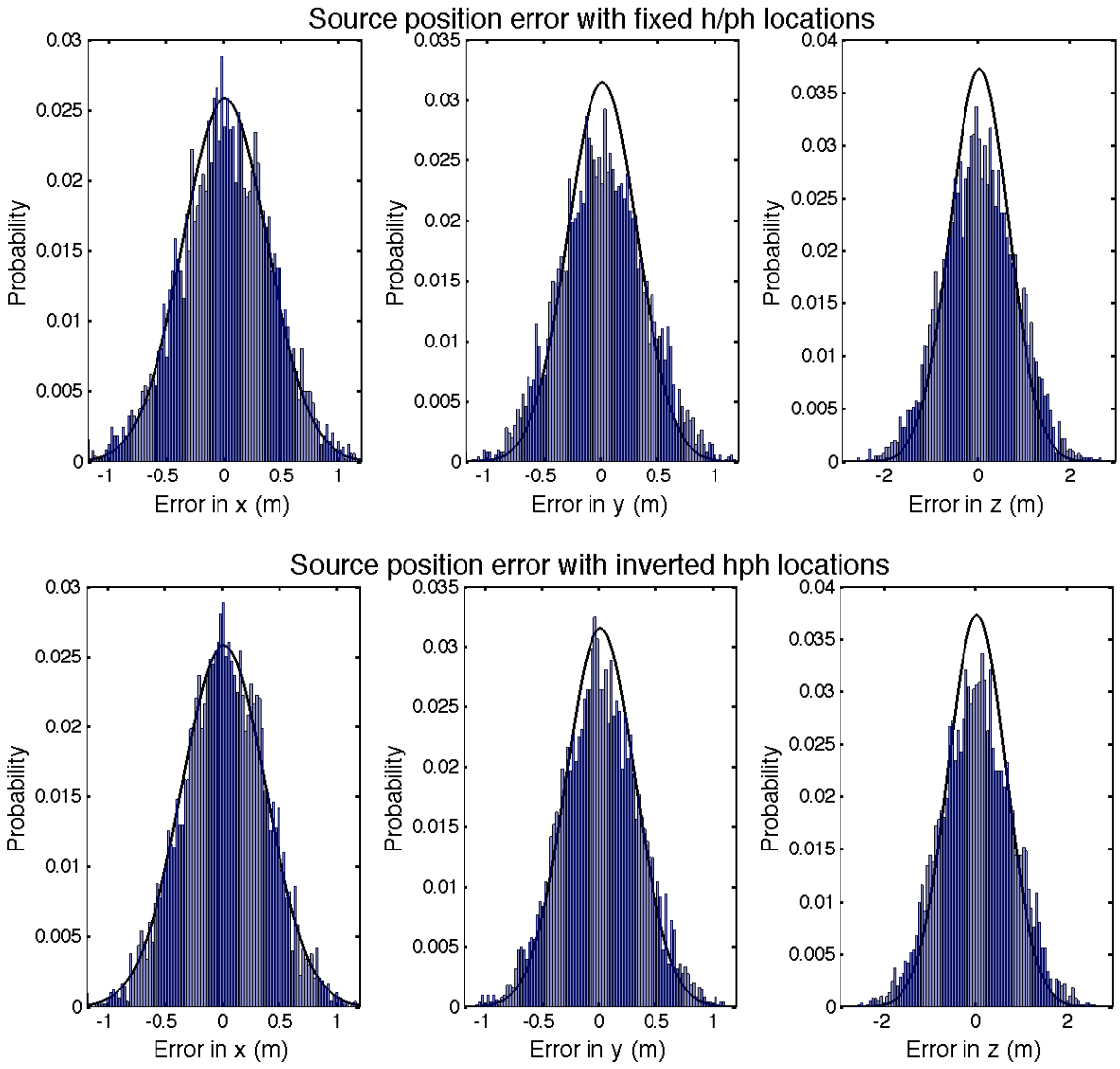

Figure 5.15: Histogram of *x, y* and *z* source-position errors when hydrophone locations are included in the inversion (bottom) and held fixed (top) for test case 1, based on inversion of 5,000 noisy data sets. Continuous distribution represents linearized uncertainty distribution.

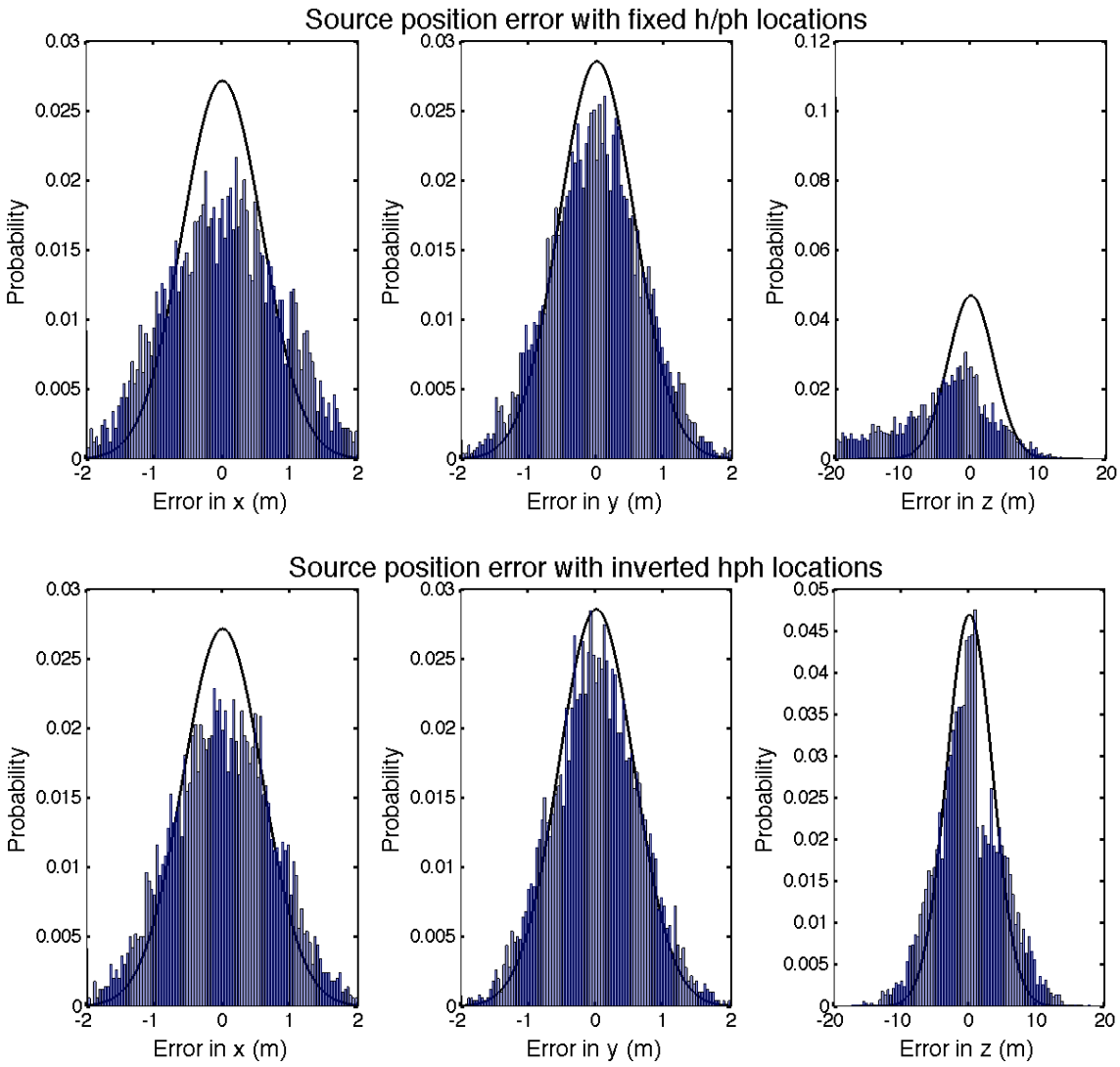

Figure 5.16: Histogram of *x, y* and *z* source-position errors when hydrophone locations are included in the inversion (bottom) and held fixed (top) for test case 2, based on inversion of 5,000 noisy data sets. Continuous distribution represents linearized uncertainty distribution.

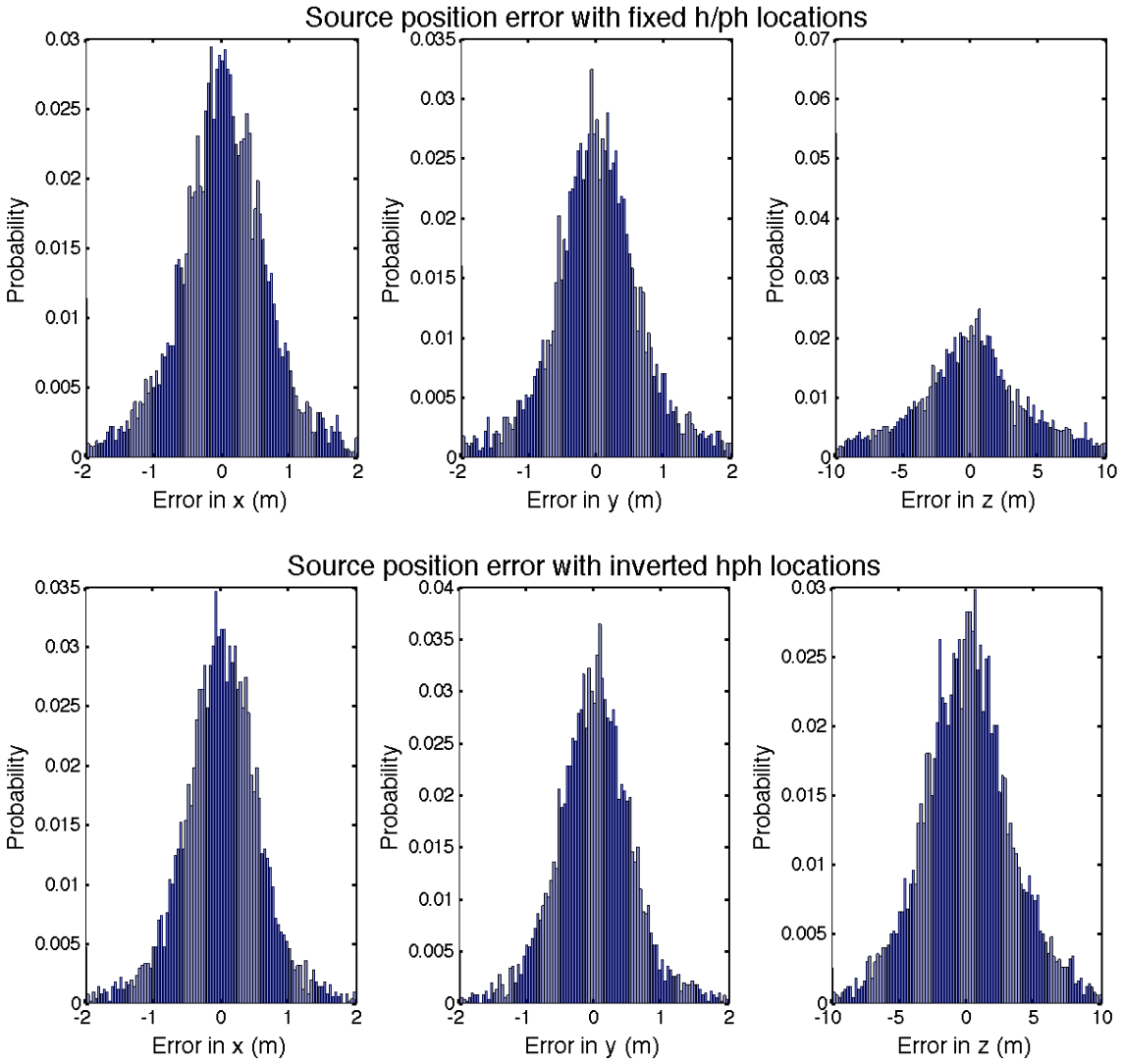

Figure 5.17: Histogram of *x, y* and *z* source-position errors when hydrophone locations are included in the inversion (bottom) and held fixed (top) for test case 3 (random source positions), based on inversion of 5,000 noisy data sets.

Source position errors due to uncertain knowledge of hydrophone positions can be considerable. For test case 1 (Fig. 5.15), the source position RMS errors for the uncorrected inversion are 31, 30 and 64 cm, respectively, in *x, y* and *z*, as compared to errors of 29, 27 and 63 cm when inverting for hydrophone position, as given in Table 5.5.

Comparison of Monte Carlo results to the linearized uncertainties indicates good agreement for *x* and *y* in both the uncorrected and corrected inversions, while nonlinear error distributions are slightly wider than linear estimates in *z* for either method. Standard deviation is the dominant component of overall RMS error, implying that over many samples, the bias from individual hydrophone errors results in a zero-mean source-position error bias.

Test case		Fixed h/ph positions			Inverted h/ph positions		
		x	y	z	x	y	z
1	Bias (m)	0.31	0.3	0.64	0.29	0.27	0.63
	σ (m)	0.24	0.22	0.48	0.22	0.21	0.47
	RMS (m)	0.4	0.37	0.8	0.37	0.34	0.79
2	Bias (m)	0.033	-0.011	-6.3	0.0056	-0.0086	-0.11
	σ (m)	0.88	0.68	9.6	0.76	0.64	4.8
	RMS (m)	0.88	0.68	11	0.76	0.64	4.8
3	Bias (m)	0.017	-0.0063	0.18	0.0075	-0.0040	0.072
	σ (m)	0.76	0.80	6.3	0.63	0.61	3.4
	RMS (m)	0.76	0.80	6.4	0.63	0.61	3.4

Table 5.5: Bias, standard deviation (σ), and RMS error for *x, y*, and *z* source position for each of the three test cases when including hydrophone position in the inversion and when holding the hydrophone position fixed in the inversion, for the case of a zero-mean, Gaussian distributed random error with standard deviation 0.5 m added to prior estimates of hydrophone positions.

As source-hydrophone geometry becomes poorer, as in test case 2 (Fig. 5.16), the improved accuracy of the corrected inversion becomes more apparent. Here, source

position errors from Table 5.5 are 88 and 68 cm in *x* and *y*, respectively, and 11 m in *z*, for uncorrected inversions, compared to 76 and 64 cm in *x* and *y*, and 4.8 m in *z*, when inverting for hydrophone position. Agreement between linear uncertainty estimates and nonlinear Monte Carlo results are good in *x* and *y* for either inversion method, and in *z* for the corrected inversion; however, the agreement in *z* for the uncorrected inversion is very poor, and displays an error bias of -6.3 m.

For test case 3, random source positions, improvements are again evident when inverting for hydrophone position, shown in Table 5.5. As compared to the results from test case 2, it is noted that random source position errors for the uncorrected inversion are greater for *x* and *y*, but test case 3 performs substantially worse for localizing in *z* when hydrophone position errors are not accounted for. The implication is that the test case 2 position, towards the periphery of the range, is particularly susceptible to hydrophone errors when resolving source position in *z*. The corrected inversion is proficient at accounting for this error, as it shows the most dramatic improvement, as compared to the uncorrected inversion, at the test case 2 position.

The sound-speed profile has a slight impact on the source-location uncertainties. The uncorrected inversion produces the smallest uncertainties for the upward-refracting December SSP, while the corrected inversion performs marginally better when the September SSP is used. For either case, the November profile produced the greatest uncertainties, most notably in *z,* where the mean error was almost 20 cm larger than when using the other profiles.

Test case		Fixed h/ph positions			Inverted h/ph positions		
		x	y	z	x	y	z
1	Bias (m)	-0.0032	0.0096	0.026	-0.0015	0.013	0.0017
	σ (m)	0.37	0.37	1	0.33	0.3	0.86
	RMS (m)	0.37	0.37	1	0.33	0.3	0.86
2	Bias (m)	0.087	-0.055	-3.3	0.022	0.0074	0.016
	σ (m)	1.0	0.88	11	0.76	0.63	2.1
	RMS (m)	1.0	0.88	11	0.76	0.63	2.1
3	Bias (m)	0.023	0.003	0.24	0.024	-0.0058	0.037
	σ (m)	1.5	1.7	6.3	0.97	0.95	3.5
	RMS (m)	1.5	1.7	6.3	0.97	0.95	3.5

Table 5.6: Bias, standard deviation (σ), and RMS error for *x, y*, and *z* source position for 10 source transmissions, for each of the three test cases when including hydrophone position in the inversion and when holding the hydrophone position fixed in the inversion, for the case of a zero-mean, Gaussian distributed random error with standard deviation 0.5 m added to prior estimates of hydrophone positions.

Table 5.6 shows the results when data are from 10 sets of arrival time difference measurements, and the inversion solves for 10 source positions. Both the corrected and uncorrected inversions are able to produce more accurate estimates for the source position in *x, y*, and *z* for all three test cases. Most notably, the relative improvement between uncorrected and corrected inversions is substantial. Considering test case 3, random source positions, the single-source inversion produces RMS errors of 0.76 and 0.80 m in *x* and *y*, and 6.4 m in *z* for the uncorrected inversion, as compared to 0.63 and 0.61 m in *x* and *y*, and 3.4 m in *z* for the corrected inversion: improvements of 17, 24 and 47%, respectively. The 10-source inversion produces errors of 1.5, 1.7, and 6.3 m,

respectively, in x, y, and z for the uncorrected inversion, as compared to 0.97 and 0.95 m in x and y, and 3.5 m in z for the corrected inversion: improvements of 35, 44 and 45%. The additional data provides more information to improve hydrophone position estimates, which in turn allow more accurate estimation of the source positions. This result is notable, as it shows that accuracy in the IAS range can be further improved when a real-time solution is not required, by inverting multiple source transmissions together after they have all been received.

In summary, inverting for the uncertain hydrophone position can have a substantial impact on source-position uncertainty, as shown in Figs 5.15–5.17. The effect is dependent on source location with respect to hydrophone receivers, hydrophone position uncertainty, number of source positions in the inversion, and the sound-speed profile. For all cases, simulations where hydrophones are included in the inversion perform better than inversions with fixed hydrophone positions. A statistical summary of the simulation results of Section 5.4 is presented in Table 5.5. The average bias and standard deviation, σ, in metres is calculated for x, y, and z for each of the three test cases when inverting for the hydrophone position, and when holding the hydrophone position fixed for the inversion.

5.5 SSP Lateral Variability

This section considers a novel procedure to account for lateral variability in SSP over the test range. Section 1.5 describes a field sampling operation in which SSPs at 9 locations within the IAS range were collected over a 2-hour period on a calm day with no winds. Figure 5.18 compares two SSPs taken from opposite ends of the range, and shows that the SSPs varied by over 1 m/s at some depths. This indicates that a laterally-varying component of sound speed exists. A series of simulations are carried out here to investigate the extent to which lateral sound-speed variations like this can impact localization accuracy, and if this impact can be lessened by including path-dependent timing correction factors as unknown parameters in the inversion.

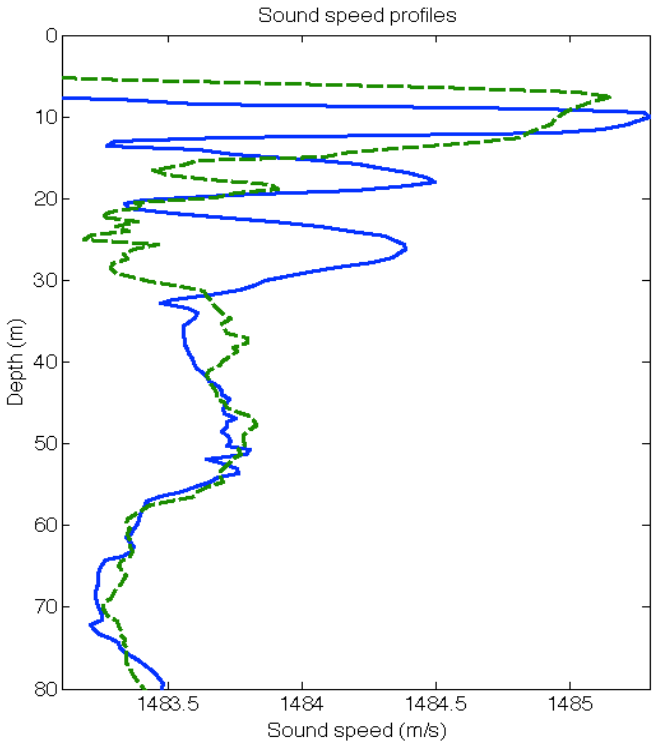

Figure 5.18: Comparison of sound speed profiles taken at two different locations in the IAS range.

To determine the degree that this SSP variation affects arrival time differences, a full multipath expansion model based on Gaussian beams known as Bellhop (Porter, 2010) was used to calculate two-dimensional (2-D) acoustic travel times for a source in the centre of the IAS test bed, with a laterally-varying sound-speed field based on a linear interpolation of the profiles shown in Fig. 5.18. The arrival times predicted with this 2-D ray tracing method were compared to arrivals assuming a range-independent average of the two profiles. The difference was found to be as much as 0.2 ms at hydrophone 5 (Fig. 5.1), and is even larger if the 2-D ray-tracing times are compared to those for one of the measured sound-speed profiles alone, rather than the average of the two. The variability in profile measurements in Fig. 5.18 is considered to be a conservative estimate of the possible lateral sound speed variation observed at the range, and thus a value of 1 ms is considered here to be representative of possible timing differences across the range due to SSP lateral variability.

Several source transmissions originating from the same general area of the range are required to determine path correction factors, and the factor is applied to all arrivals at each hydrophone. The path correction factor represents the change in travel time for a ray travelling along a specific path through the range, however, it would not apply to a ray travelling along a much different path as that correction would tend to be different. For the purposes of this simulation, the same general area is taken to be a zero-mean Gaussian distribution of standard deviation 10 m in x and y and 2 m in z about the nominal test case position. TDOA data are calculated from 50 source positions in the general area of each nominal test case position, and 1000 zero-mean, Gaussian-

distributed random variables of standard deviation 1 ms (representing a path-dependent time correction for each hydrophone) are added to the data, to produce 1000 noisy data sets representing arrival times through a laterally-varying sound-speed field. Inversions are carried out in two ways: (1) accounting for the lateral variation in sound speed by inverting for the path correction as an unknown model parameter, and (2) neglecting the laterally varying component of sound speed (i.e., not including path corrections in the inversion).

For the first two test cases, prior estimates and uncertainties are as in previous scenarios but using 50 randomly generated source positions about the nominal position as described above. For test case 3, similarly, a different random nominal source position is drawn for each iteration from within the x, y and z intervals given in Table 5.1, and 50 source positions are generated in the general area of the nominal position, with prior estimates treated as described for test cases 1 and 2. Results of inversions with and without path corrections are compared (Figs. 5.19–5.21) and tabulated (Table 5.7) for all three test cases.

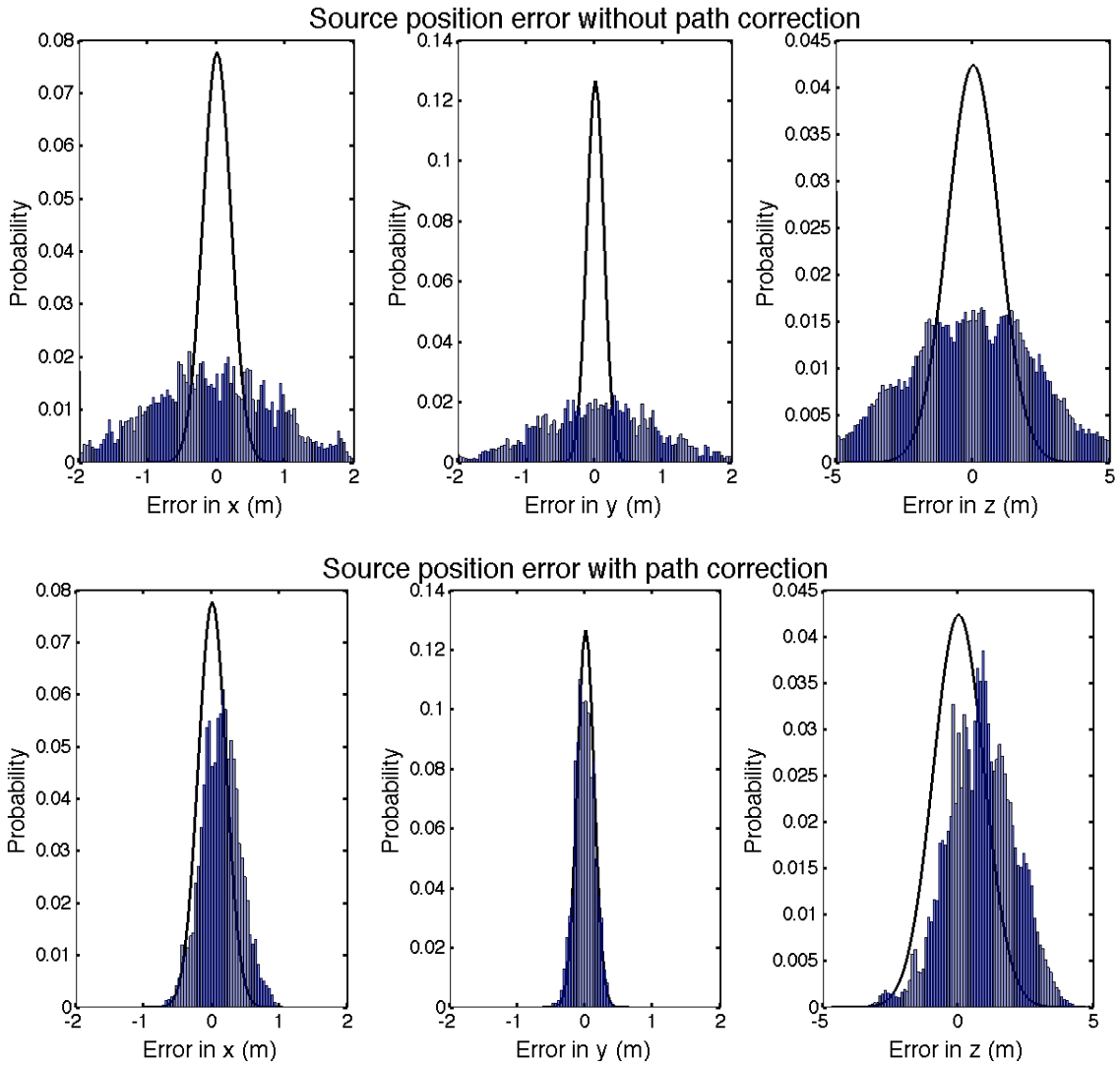

Figure 5.19: Histogram of errors for *x, y*, and *z* source position obtained when the path correction factor is included (bottom) and not included (top) in the inversion for test case 1 based on inversion of 1000 noisy data sets with 50 source transmissions.

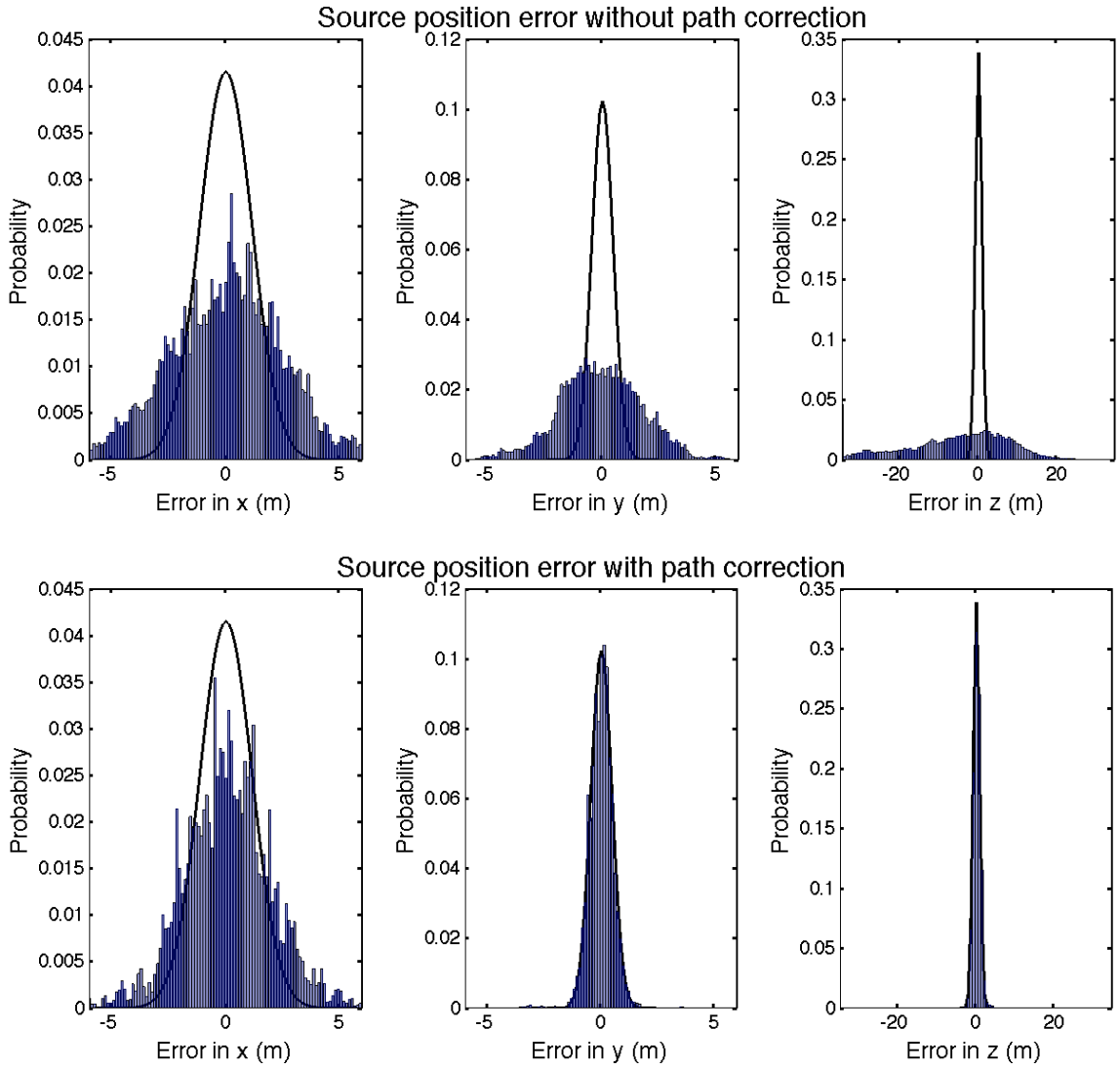

Figure 5.20: Histogram of errors for *x, y*, and *z* source position obtained when the path correction factor is included (bottom) and not included (top) in the inversion for test case 2 based on inversion of 1000 noisy data sets with 50 source transmissions.

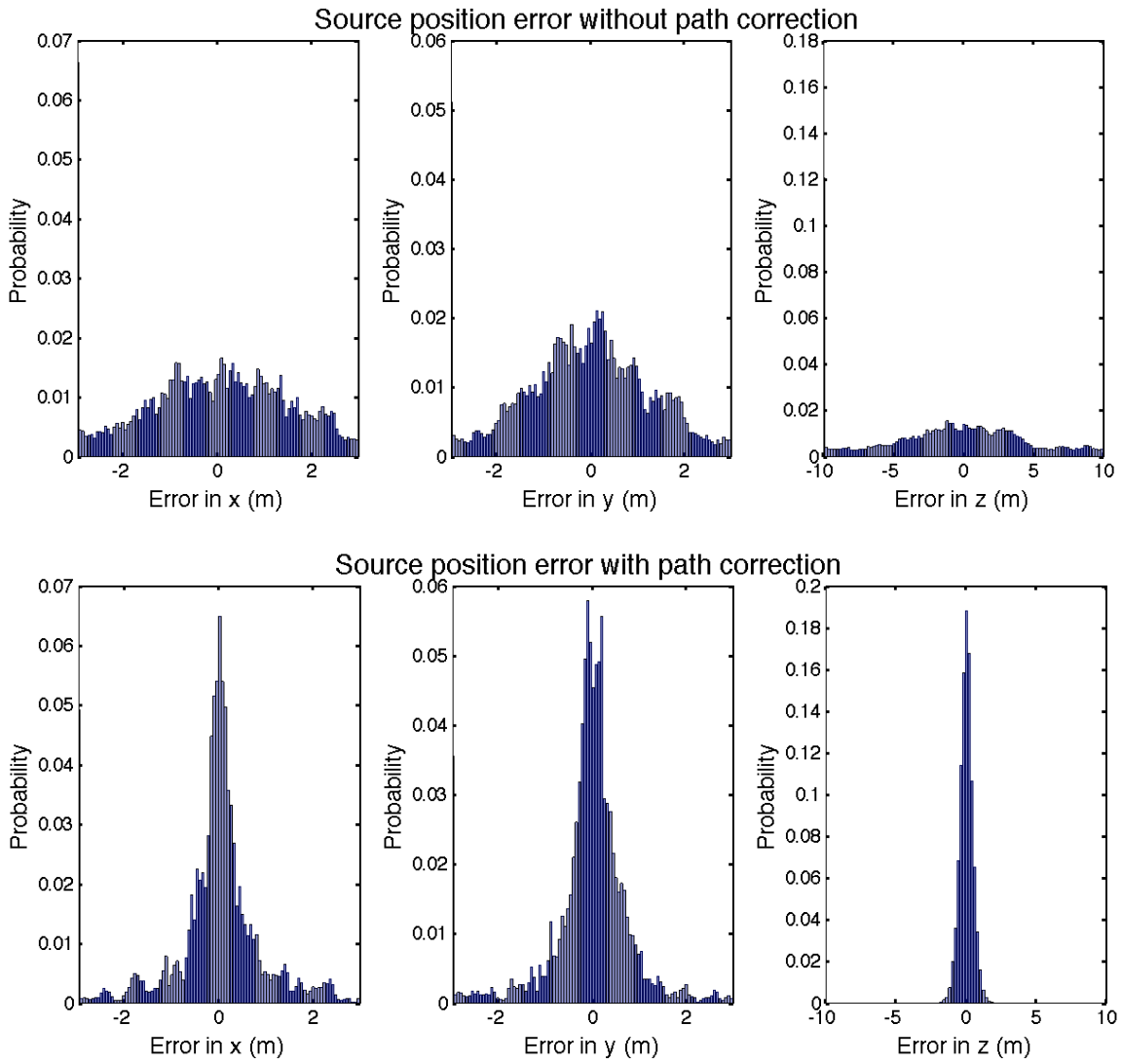

Figure 5.21: Histogram of errors for *x, y*, and *z* source position obtained when the path correction factor is included (bottom) and not included (top) in the inversion for test case 3 based on inversion of 1000 noisy data sets with 50 source transmissions.

The effect of a laterally-varying SSP on localization accuracy can be significant, as seen in Figs. 5.19–5.21. The inversion algorithm is proficient at correcting for the path correction factor with a standard deviation of 1 ms when it is applied to data from 50 source transmissions, as the corrected inversions (accounting for the path correction

factor) show substantial improvement over uncorrected inversions (which assume sound speed to be constant laterally).

Test case		No path correction			Path correction		
		x	y	z	x	y	z
1	Bias (m)	-0.058	0.043	-0.067	0.12	-0.017	0.81
	σ (m)	0.95	0.83	2.3	0.27	0.14	1.2
	RMS (m)	0.95	0.83	2.3	0.30	0.14	1.4
2	Bias (m)	0.031	-0.08	-6.2	0.089	-0.023	0.16
	σ (m)	2.5	1.8	15.0	1.9	0.56	0.99
	RMS (m)	2.5	1.8	15.0	1.9	0.56	1.0
3	Bias (m)	0.062	0.30	1.4	-0.058	-0.031	-0.098
	σ (m)	1.8	1.9	12.0	1.1	1.1	0.9
	RMS (m)	1.8	1.9	12.0	1.1	1.1	0.9

Table 5.7: Bias, standard deviation (σ), and RMS error for *x, y*, and *z* source position for each of the three test cases for inversions with and without path correction, for the case of a zero-mean, Gaussian distributed random error with standard deviation 1 ms added to the arrival time difference data to simulate a laterally varying SSP.

For test case 1 (Fig. 5.19 and Table 5.7), errors are distributed about a mean of close to zero for *x* and *y* both when inverting for a path correction (the corrected inversion), and neglecting the path correction (the uncorrected inversion); however, a bias of 0.81 m in *z* is evident in the corrected inversion. In both cases, the major contributor to RMS error is the standard deviation, indicating that the individual errors tend to cancel over many inversions. RMS errors for the uncorrected inversion are 0.95, 0.83 and 2.3 m in *x*, *y*, and *z*, respectively, and 0.27, 0.14, and 1.4 m for the corrected inversion, demonstrating a

substantial improvement in localization accuracy when lateral sound-speed variation exists and is accounted for. Agreement between the linear uncertainties predicted in the model covariance matrix and the nonlinear Monte Carlo results is good for the corrected inversion in Fig 5.19 for x and y; however, in z the numerical results show some linearization error. In the case of the uncorrected inversion, there is poor agreement between the linear uncertainties and Monte Carlo results for in x, y, and z due to the path-dependent errors that are unaccounted for.

For both uncorrected and corrected inversions in test case 2 (Fig. 5.20 and Table 5.7), the source position error resulting from random lateral variation in SSP are not significantly biased in x and y, but are biased in z for the uncorrected inversion. Errors are distributed over a much wider range when path correction is not included as an inversion parameter, but both inversions do poorly at resolving the source position in x, due to the source-hydrophone geometry at this unfavourable location. As compared to the uncorrected inversion RMS errors on the corrected inversion are small: 2.5, 1.8, and 15.0 m in x, y, and z for the uncorrected inversion, and 1.9, 0.56 and 1.0 m for the corrected inversion. Test case 2 shows good agreement between linear uncertainty estimates and nonlinear Monte Carlo results for the corrected inversion in y and z; however, the agreement in x is somewhat poorer due to the wider distribution of errors. Linear uncertainty estimates are not in agreement with nonlinear Monte Carlo results in the uncorrected inversion due to errors arising from the unaddressed lateral SSP variation.

The results from test case 3, shown in Fig. 5.21 and summarized in Table 5.7, again show substantial improvement when a path correction is applied in the localization inversion. The improvement in z is most notable, 12-m RMS error for uncorrected

inversions as compared to 0.9 m for corrected inversions. Linearized uncertainty estimates are not shown for test case 3 as this case involves randomly selected source locations and hence the analytic solution is not defined.

The most notable result from test cases 2 and 3 is the improvement in errors in z, typically the most problematic to localization due to the fact that all hydrophones are on one side (below) the sources. Shifting sources in z is equivalent to a time shift of the same sign at each hydrophone (different from x and y). Hence, z is typically less constrained than x and y, and path correction factors can be (approximately) accounted by errors in z.

The simulations described above were carried out assuming that data from 50 source transmissions were available for the inversion. A greater number of source transmissions provides additional information to an overdetermined problem, and the solution is generally improved. To investigate whether localization accuracy is affected by the number of source transmissions, and hence, number of data available for the inversion, a simulation was carried out as described for the scenario above, but using only 20 source transmissions, for test case 1. Results are shown in Figure 5.22 and summarized in Table 5.8.

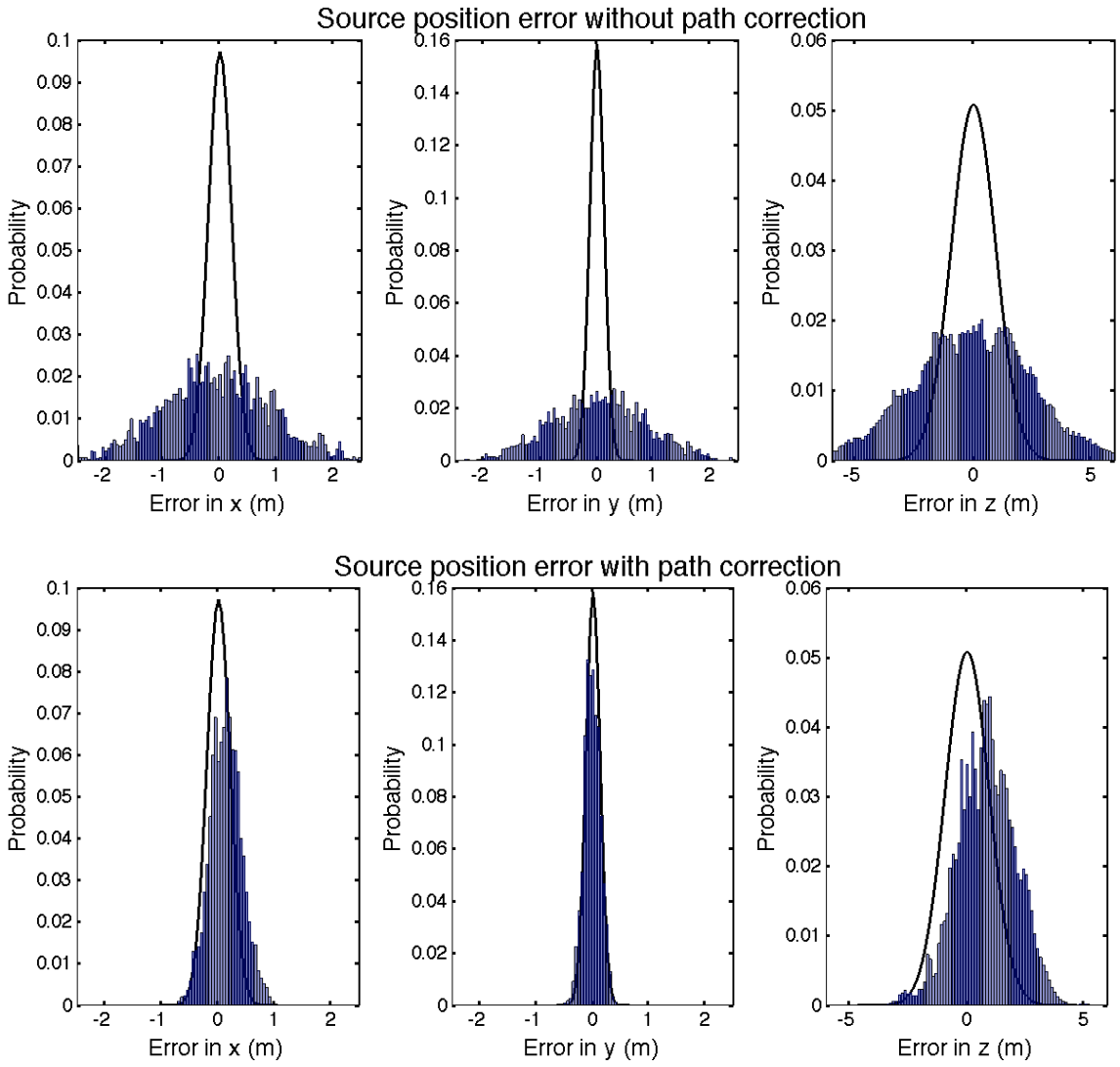

Figure 5.22: Histogram of errors for *x, y*, and *z* source position obtained when path correction is included (bottom) and not included (top) as an inversion parameter with 20 source transmissions for test case 1 based on inversion of 1000 noisy data sets with random path corrections applied. Continuous distribution represents linearized uncertainty distribution.

Figure 5.22 and Table 5.8 show that the number of source transmissions plays a role in determining localization accuracy. In this case, inverting for the path correction

improves the RMS source-position error in *x*, *y*, and *z*, from 0.9, 0.8 and 12 m for the uncorrected inversion, respectively, to 0.43, 0.34, and 2.2 m for the corrected inversion. However, this improvement is not as large as when 50 source transmissions were used (Table 5.7).

Test case		No path correction			Path correction		
		x	y	z	x	y	z
1	Bias (m)	0.036	0.012	0.20	0.20	-0.06	1.4
	σ (m)	0.90	0.8	2.7	0.37	0.34	1.7
	RMS (m)	0.90	0.8	2.7	0.43	0.34	2.2

Table 5.8: Bias, standard deviation (σ), and RMS error for *x, y*, and *z* source position for test case 1 when inverting for inversions with and without path correction, for the case of a zero-mean, Gaussian distributed random error with standard deviation 1 ms added to the arrival time difference data to simulate a laterally-varying SSP, based on 20 source transmissions.

The lateral variation in sound speed depends on prevailing environmental conditions on any given day. The simulations considered above have assumed a laterally-varying SSP resulting in time differences with a standard deviation of 1 ms. This variation is greater than what was observed at the IAS range on one calm day in November, but is likely a realistic estimate of the variation that could be observed in more extreme conditions, such as during heavy spring runoff, or with a persistent internal tide. To investigate the effectiveness of inverting for a path correction factor when lateral SSP variation is smaller, a simulation was carried out, using 50 source transmissions, but with

random time correction factors of standard deviation 0.6 ms, for test case 1. The results of this simulation are presented in Fig 5.23 and summarized in Table 5.9.

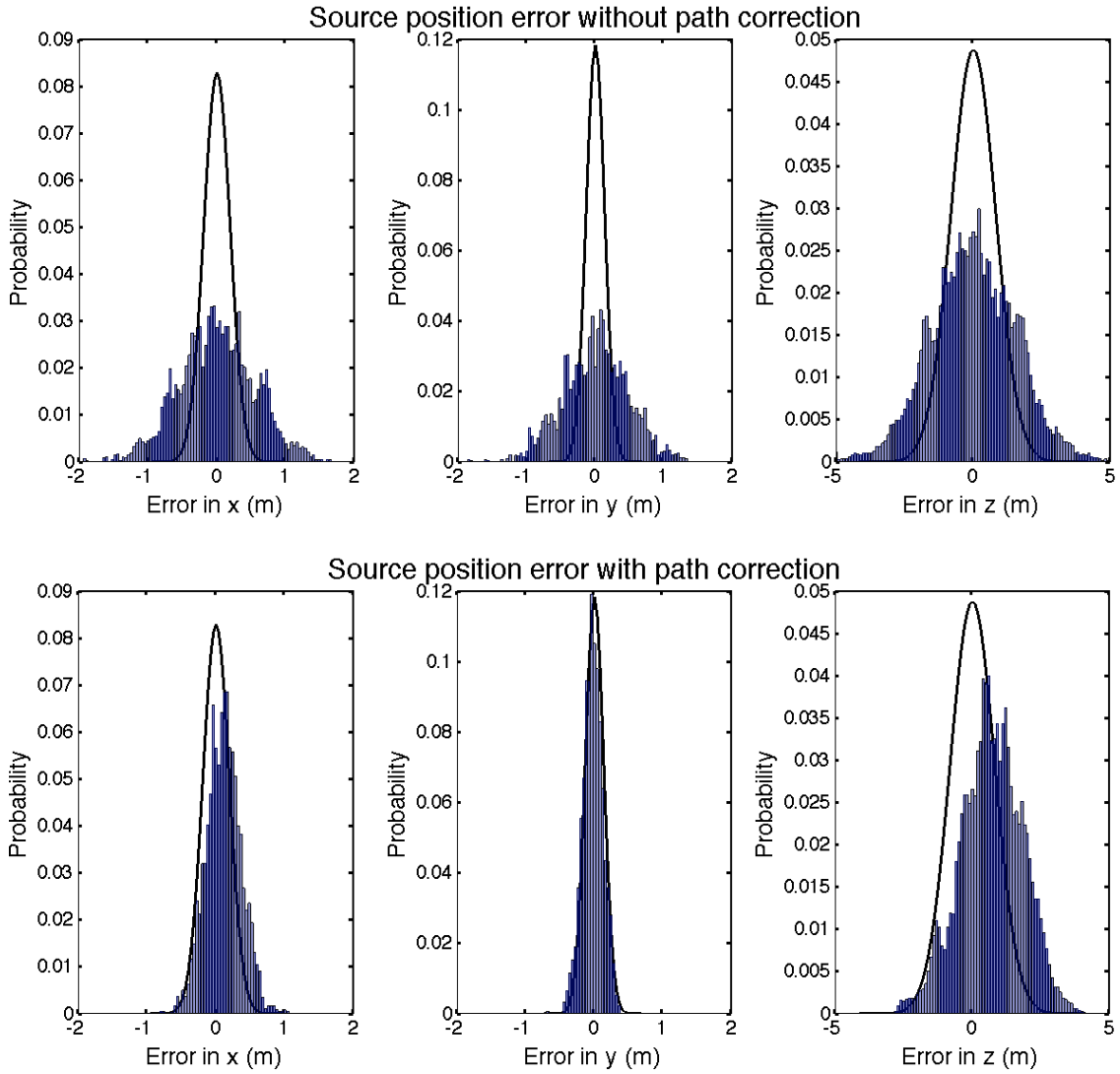

Figure 5.23: Histogram of errors for *x, y*, and *z* source position obtained when the path correction factor of standard deviation 0.6 ms is included (bottom) and not included (top) in the inversion for test case 1 based on inversion of 1000 noisy data sets with 50 source transmissions.

Test case		No path correction			Path correction		
		x	y	z	x	y	z
1	Bias (m)	-0.0018	0.0018	0.026	0.11	-0.027	0.69
	σ (m)	0.55	0.48	1.6	0.26	0.15	1.2
	RMS (m)	0.55	0.48	1.6	0.28	0.15	1.3

Table 5.9: Bias, standard deviation (σ), and RMS error for *x, y*, and *z* source position for test case 1 for inversions with and without path correction, for the case of a zero-mean, Gaussian distributed random error with standard deviation 0.6 ms added to the arrival time difference data to simulate a laterally-varying SSP.

When standard deviations of path corrections added to the data are reduced to 0.6 ms, errors for the uncorrected inversion decrease as compared to the case where 1 ms standard deviations are used (Fig. 5.19 and Table 5.7), however, results for the corrected inversion are essentially the same for either standard deviation, indicating that the algorithm is effective at predicting path corrections even for smaller levels of lateral SSP variation.

Since estimation of the path correction parameter requires data from several source transmissions, this factor can be built up in real-time as transmissions are received, becoming more accurate as the target emits more pings from the same general area. However, it may be most effective when used to improve source location estimates *a posteriori*. Referring back to Chapter 1, the goal of the IAS range is to provide highly-accurate AUV localization against which to compare stand-alone AUV navigation systems. To this end, targets can be equipped with depth-sensors to provide more accurate prior information in *z*. To simulate the use of this depth-sensor information,

simulations are carried out in which the prior uncertainty in z is reduced to 14 cm (a typical uncertainty for an inexpensive pressure sensing device), instead of 10 m, and results of the corrected and uncorrected inversions are compared to see if the addition of depth sensor information, in conjunction with the path correction, improve the localization accuracy in x and y for 50 source transmissions. Only test case 1 is considered, and results are shown in Figure 5.24 and summarized in Table 5.10.

Comparing the results of the depth sensor simulation for test case 1, shown in Fig. 5.24 and Table 5.10, to those without depth sensor information, shown in Fig. 5.19 and Table 5.7, it is apparent that the addition of depth sensor information improves corrected inversion source position accuracy not only in z, from 140 to 3.7 cm, but also in x, 30 to 17 cm, while y remains unimproved, at 16 cm as compared to 14 cm when depth sensor information is not included. This result implies that when a laterally-varying SSP exists in the IAS range, maximum localization accuracy can be achieved by incorporating the depth sensor information along with arrival time difference data to produce a complete positioning solution. That the y component of localization accuracy is unimproved may indicate that there is a limit to localization accuracy that is dependent on source-hydrophone geometry. The error in z for uncorrected inversion, 2.3 m, is much higher than the prior uncertainty in z, 0.14 m, as the inversion algorithm trades off fitting prior information with fitting data that include an unaccounted for source of error (lateral SSP variability).

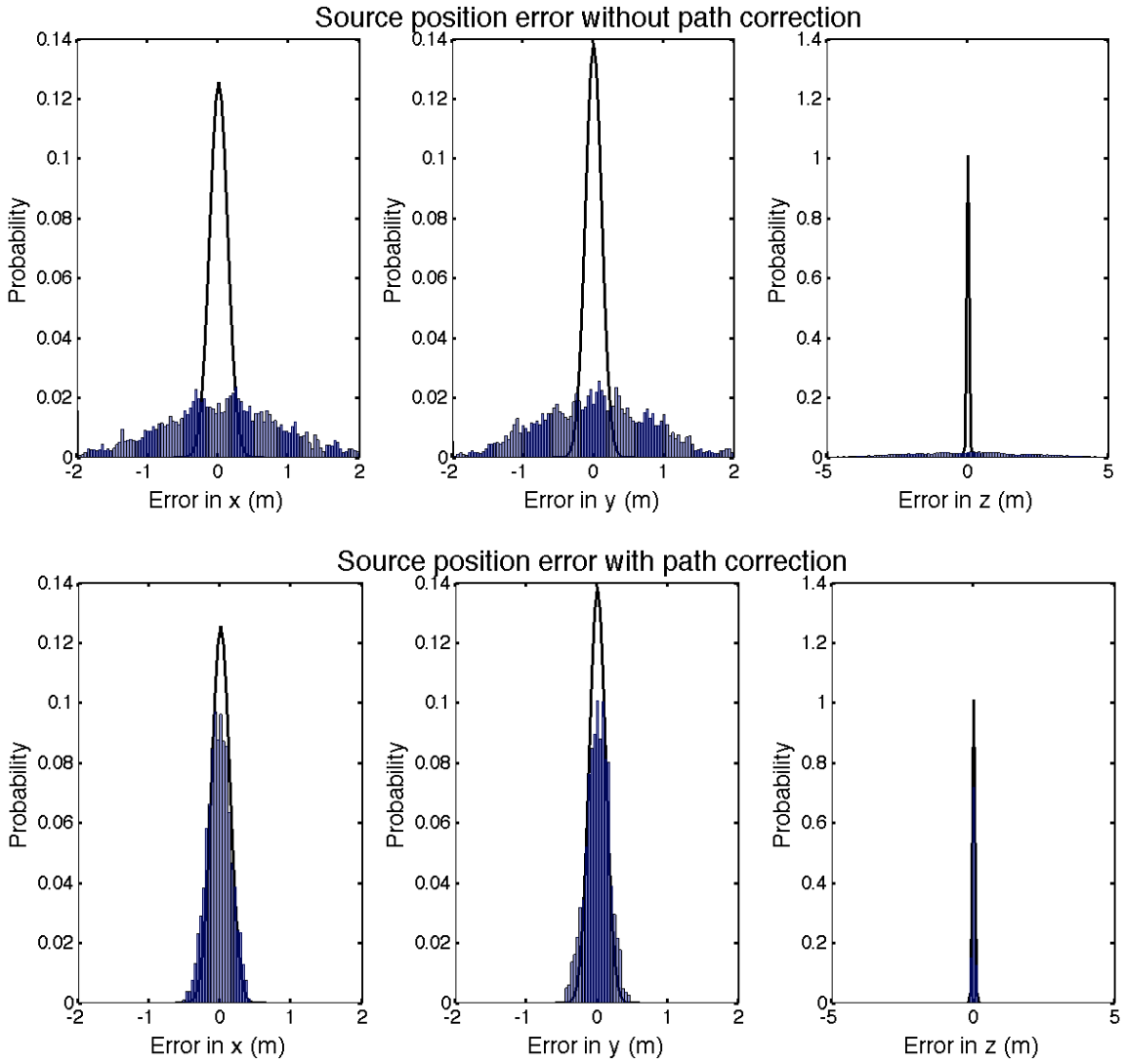

Figure 5.24: Histogram of errors for *x, y*, and *z* source position obtained when path correction is included (bottom) and is not included (top) as an inversion parameter when considering depth sensor information for test case 1 based on inversion of 1000 noisy data sets with random path corrections and *z*. Continuous distribution represents linearized uncertainty distribution.

Test case		No path correction			Path correction		
		x	y	z	x	y	z
2	Bias (m)	0.038	0.013	-0.054	-0.027	0.0020	-0.0025
	σ (m)	0.91	0.81	2.3	0.16	0.16	0.037
	RMS (m)	0.91	0.81	2.3	0.17	0.16	0.037

Table 5.10: Bias, standard deviation (σ), and RMS error for *x, y*, and *z* source position for test case 1 for inversions with and without path correction, for the case of a zero-mean, Gaussian distributed random error with standard deviation 1 ms added to arrival time difference data, and prior uncertainties in *z* are 14 cm to simulate depth sensor information.

5.6 Summary

This chapter investigated the impact of a number of factors in source localization accuracy through four general scenarios, carried out with simulations for sources at three test case positions, using a Monte Carlo method to quantify results. Scenarios investigated the effect of: (1) modelling transmission paths accounting for refraction due to a depth-varying SSP instead of using straight rays through a constant sound-speed approximation, (2) inverting for a potential sound-speed bias in the measured profile, (3) accounting for errors in hydrophone position by including these positions as unknowns in the inversion, and (4) applying path correction factors to account for lateral variability in the sound-speed profile.

For each factor, results were compared when addressing the factor in the inversion, and when the factor was neglected. In this summary section, a complete inversion is presented that integrates all four improvements into a single algorithm that addresses ray

tracing, SSP bias, uncertain hydrophone positions, and lateral sound speed variation in a localisation solution. Errors are applied as described in the general cases of preceding sections, with 1000 noisy data sets created by applying randomly chosen sound-speed biases from a zero-mean Gaussian distribution of standard deviation 1 m/s; uncertain hydrophone locations represented by a Gaussian-distributed zero-mean error of standard deviation 0.5 m added to the true position of each hydrophone in *x, y* and *z*; and zero-mean Gaussian-distributed random variables of standard deviation 1 ms representing a path-dependent time correction for each hydrophone added to each arrival time difference. Inversions were carried out for 50 source transmissions using the November SSP (Fig. 5.2), and results are presented in Fig. 5.25 and Table 5.11 for all three test cases.

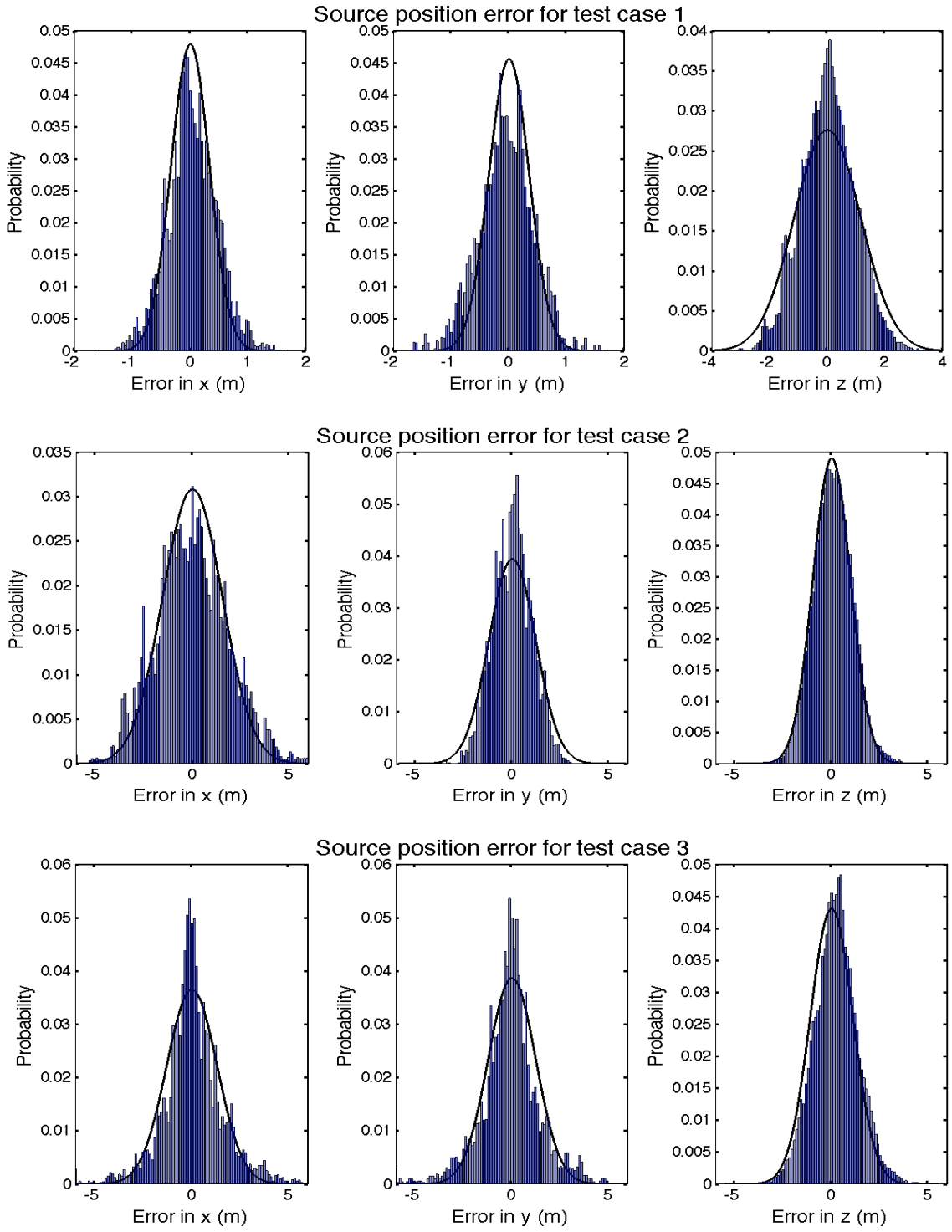

Figure 5.25: Histogram of errors for *x, y*, and *z* source position for the complete inversion for test cases 1, 2 and 3 based on inversion of 1000 noisy data sets with 50 source transmissions.

Test case		x	y	z
1	Bias (m)	0.0035	-0.054	0.020
	σ (m)	0.41	0.47	0.93
	RMS (m)	0.41	0.47	0.93
2	Bias (m)	0.0028	0.0094	0.076
	σ (m)	1.8	0.98	0.91
	RMS (m)	1.8	0.98	0.91
3	Bias (m)	0.067	-0.067	0.22
	σ (m)	1.6	1.6	1.1
	RMS (m)	1.6	1.6	1.2

Table 5.11: Bias, standard deviation (σ), and RMS error for *x, y*, and *z* source position for each of the three test cases when inverting for SSP bias, hydrophone position, and path correction.

The complete ray-based inversion produces errors of 0.41 m, 0.47 m and 0.93 m in *x*, *y*, and *z*, respectively, for test case 1; 1.8, 0.98, and 0.91 m in *x*, *y*, and *z* for test case 2; and 1.6, 1.6, and 1.2 m in *x*, *y*, and *z* for test case 3. These errors represent an estimate of the accuracy that the IAS would be able to achieve using the algorithm described in this thesis, when sources of error are as described above. Referring to Figures 5.6–5.8 and Table 5.2, results from this section can be compared to the 'best case' scenario where timing error is the lone source of error. There, errors in *x*, *y*, and *z*, were shown to be 1.3, 1.2, and 6.6 cm for test case 1; 3.0, 2.5 and 47 cm for test case 2; and 4.6, 3.1 and 69 cm for test case 3. Clearly, the addition of errors reduces the system accuracy. However, it is notable that while errors in *x* and *y* are worse for the complete inversion, increasing by an order of magnitude over the 'best case', the errors in *z* increased by a much smaller

proportion. Linearization errors are unsubstantial, with good agreement between the linear uncertainties predicted in the model covariance matrix and the nonlinear Monte Carlo results.

The simulations carried out in this chapter have shown that the ray-based, linearized inversion algorithm developed in this thesis is capable of effectively accounting for each of the factors investigated. In each case, the inversion developed to address the factor performed better than the inversion that did not. Statistical measures for each inversion method were compared, and the complete inversion was tested when noise was added from all error sources considered. Results from test cases 1 and 2 showed that the algorithm generally performs better when source-hydrophone geometry is good, and results from test case 3 show that the algorithm is robust enough to provide a localisation solution for any source location in the range.

6 Summary

Autonomous underwater vehicles (AUVs) are used in a wide range of underwater applications, from scientific data gathering to offshore construction; however, accurate localization and navigation of these vehicles remains a challenge. The Integrated Acoustic System (IAS) under development by the University of Victoria Ocean Technology Test Bed team aims to provide a highly-accurate acoustic test range for ground-truth AUV localizations against which standalone navigation systems can be tested. As part of the VENUS cabled underwater network, the IAS is based on five hydrophones mounted on seabed towers which measure the arrival times of impulsive acoustic signals which are periodically emitted by an AUV operating within the range. The IAS will employ a high-precision network timing protocol, known as PTP, which reduces system-timing errors to a level that allows high-precision acoustic positioning of an underwater target. By working with the difference of arrival times between receivers, the need to determine the transmission instant from the (asynchronous) source is eliminated, in a technique known as multilateration (IMCA, 2009).

This thesis developed a Bayesian inversion algorithm for AUV localization, and carried out a study of several factors contributing to localization accuracy in an underwater acoustic positioning system. Specifically, a ray-based algorithm has been developed that estimates target position through the linearized inversion of transmission arrival time differences, and provides linearized uncertainty estimates for model parameters. Factors contributing to source localization uncertainty considered here included: (1) modelling transmission paths accounting for refraction due to a depth-

varying SSP instead of using a constant sound-speed approximation and straight-line propagation, (2) inverting for a potential bias in the measured sound-speed profile, (3) accounting for errors in hydrophone position by including these positions as unknown parameters in the inversion, and (4) applying path-dependent timing correction factors to account for lateral variability in the sound-speed profile. In each case, nonlinear Monte Carlo analysis was applied in which a large number of noisy data sets were considered to obtain statistical measures of the localization improvement that resulted by addressing these factors. These simulations also compared linearized uncertainty estimates to non-linear (numerical) uncertainties, and show that for the cases investigated, linearization errors are generally small.

Additionally, localization uncertainties were considered as a function of source location over the entire range, since the acoustic positioning system accuracy was shown to be strongly dependent on source-hydrophone geometry. For this investigation, source position uncertainty due to hydrophone position and sound-speed profile uncertainties are considered, in addition to the effect of changes to timing error, range hydrophone geometry, and source depth.

The work described in this thesis builds upon previous efforts in underwater acoustic localization as described in Dosso and Ebbeson (2006). A new technique, not believed to have been applied previously to underwater acoustic localization but borrowed from earthquake seismology, accounts for lateral dependence in sound speed over the range by inverting for a specific path-dependent time correction factor applied to each hydrophone, assuming multiple source transmissions from a relatively small region. This method was

shown to improve localization accuracy when lateral variation in sound speed is present in the range.

This thesis applied simulated data to the investigations described above. Future work would see these inversion techniques applied to IAS range data, both in real-time and in post-processing where maximum localization accuracy might be achieved. Analysis of *in situ* data would likely bring rise to new factors affecting localization accuracy, such as ambient noise interference and multipath effects, and these will need to be addressed as IAS operations are brought online.

Bibliography

Akyildiz, I., Pompili, D., & Melodia, T. (2005). Underwater acoustic sensor networks: research challenges. *Ad Hoc Networks*, *3*(3), 257–279.

Ameer, P., & Jacob, L. (2010). Localization using ray tracing for underwater acoustic sensor networks. *IEEE Communications Letters*, *14*(10), 930–932.

AML Oceanographic, *SV Plus Sound Velocimeter* (2012). Retrieved from: http://www.amloceanographic.com/Products-Services/Sound-Velocity.

Aster, R., B. Borchers and C. Thurber, *Parameter Estimation and Inverse Problems* (Academic Press, Orlando, 2004).

Bingham, B., & Seering, W. (2006). Hypothesis grids: Improving long baseline navigation for autonomous underwater vehicles. *IEEE Journal of Oceanic Engineering*, *31*(1), 209–218.

Chandrasekhar, V., Seah, W., Choo, Y., & Ee, H. (2006). Localization in underwater sensor networks: survey and challenges. *Proceedings of the 1st ACM international workshop on Underwater networks*, 33–40.

Dosso, S. E., & Ebbeson, G. R. (2006). Array element localization accuracy and survey design. *Canadian Acoustics*, *34*(4), 1–11.

Dosso, S., Brooke, G., Kilistoff, S., Sotirin, B., McDonald, V., Fallat, M., & Collison, N. (1998a). High-precision array element localization for vertical line arrays in the Arctic Ocean. *IEEE Journal of Oceanic Engineering*, *23*(4), 365–379.

Dosso, S., Fallat, M., Sotirin, B., & Newton, J. (1998b). Array element localization for horizontal arrays via Occam's inversion. *The Journal of the Acoustical Society of America*, *104*, 846–859.

Eustice, R. M., Singh, H., & Whitcomb, L. L. (2010). Synchronous-clock, one-way-travel-time acoustic navigation for underwater vehicles. *Journal of Field Robotics*, *28*(1), 121–136. doi:10.1002/rob.20365

Gamroth, E., Kennedy, J., & Bradley, C. (2011). Design and testing of an acoustic ranging technique applicable for an underwater positioning system. *Underwater Technology: The International Journal of the Society for Underwater Technology*, *29*(4), 183–193. doi:10.3723/ut.29.183

Garcia, J. (2005). Positioning of sensors in underwater acoustic networks. *Proceedings of MTS/IEEE OCEANS 2005*, 2088–2092 Vol. 3.

Hahn, M. (2005). Undersea navigation via a distributed acoustic communications network, *Proceedings of the Turkish International Conference on Acoustics*, July 4-8, 2005, Istanbul, Turkey.

International Marine Contractors Association (2009). *Deep Water Acoustic Positioning.* Retrieved from: www.imca-int.com

Isik, M., & Akan, O. (2009). A three dimensional localization algorithm for underwater acoustic sensor networks. *Wireless Communications, IEEE Transactions on*, *8*(9), 4457–4463.

Jensen, F., Kuperman, W., Porter, M., & Schmidt, H., *Computational Ocean Acoustics* (Springer, New York, 2nd Ed., 2011).

Kussat, N., Chadwell, C., & Zimmerman, R. (2005). Absolute positioning of an autonomous underwater vehicle using GPS and acoustic measurements. *IEEE Journal of Oceanic Engineering*, *30*(1), 153–164.

Lee, P., Jun, B., Kim, K., & Lee, J. (2007). Simulation of an inertial acoustic navigation system with range aiding for an autonomous underwater vehicle. *IEEE Journal of Oceanic Engineering*, *32*(2), 327–345.

Lentz, S., & Lecroart, A. (2009). Precision timing in the NEPTUNE Canada network. *OCEANS 2009-EUROPE*, 1-5.

Menke, W., *Geophysical Data Analysis: Discrete Inverse Theory* (Academic Press, Orlando, 1984).

Monteiro, L. S., Moore, T., & Hill, C. (2005). What is the accuracy of DGPS? *Journal of Navigation*, *58*(2), 207–225.

Ocean Technology Lab. *Integrated Acoustic System* (2005). Retrieved from: http://web.uvic.ca/~lacir/ocean/acoustics.php

Porter, M., *Bellhop Manual* (2011), Retrieved from: http://oalib.hlsresearch.com/Rays/HLS-2010-1.pdf.

Sambridge, M. and K. Mosengaard, 2002. Monte Carlo methods in geophysical inverse problems, *Reviews of Geophysics*, 40(3), 3-29.

Sonardyne, *LBL Acoustic Positioning Systems* (2012). Retrieved from: http://www.sonardyne.com

Sen, M. K. and P. L. Stoffa, *Global Optimization Methods in Geophysical Inversion* (Elsevier, Amsterdam, 1995).

Siderius, M., Nielsen, P., Sellschopp, J., Snellen, M., & Simons, D. (2001). Experimental study of geo-acoustic inversion uncertainty due to ocean sound-speed fluctuations. *The Journal of the Acoustical Society of America*, *110*, 769.

Stutters, L., Liu, H., Tiltman, C., & Brown, D. (2008). Navigation technologies for autonomous underwater vehicles. *IEEE Transactions on Systems, Man, and Cybernetics, Part C: Applications and Reviews, 38*(4), 581–589.

Tarantola, A., *Inverse Problem Theory: Methods for Data Fitting and Model Parameter Estimation* (Elsevier, Amsterdam, 1987).

Thomson, D., Dosso, S. E., Gamroth, E., & Bradley, C. (2012). Modelling Uncertainty in an Underwater Acoustic Positioning System. *Canadian Acoustics*, *40*(1), 30–37.

Wang, D., Kannan, R., & Wei, L. (2010). Time of flight based two way ranging for real time locating systems. *Proceedings of the 2010 IEEE Conference on Robotics Automation,* 199–205

Whitcomb, L., Yoerger, D., Singh, H., & Howland, J. (1999). Combined Doppler/LBL based navigation of underwater vehicles. *Proceedings of the International Symposium on Unmanned Untethered Submersible Technology*, 1–7.

Zhou, L. (2010). A Precise Underwater Acoustic Positioning Method Based on Phase Measurement, MASc Thesis, University of Victoria.